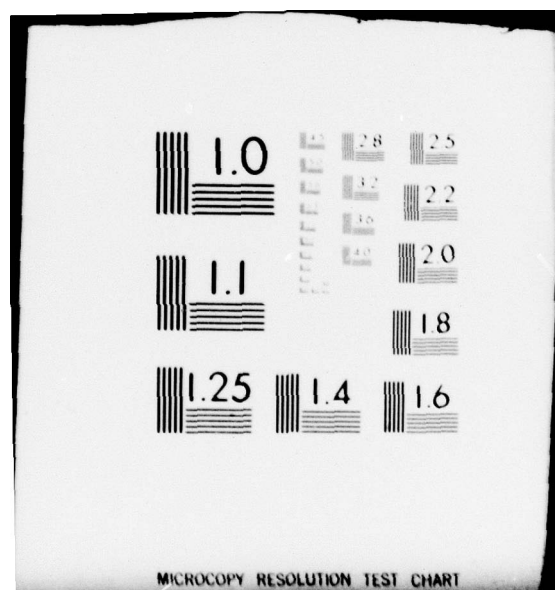


AD-A075 373 SYRACUSE UNIV NY DEPT OF ELECTRICAL AND COMPUTER EN--ETC F/G 17/8
DEFT: ADVANCED STRUCTURES AND APPLICATIONS.(U)
JUN 79 S T KOWEL, P G KORNREICH, A MAHAPATRA DAA653-76-C-0162
UNCLASSIFIED TR-79-12 NL

1 OF 2

AD
A075373





ADAU75373

Unclassified

SECURITY CLASSIFICATION OF THIS PAGE (When Data Entered)

REPORT DOCUMENTATION PAGE		READ INSTRUCTIONS BEFORE COMPLETING FORM
1. REPORT NUMBER DAAG53-76-C-0162 #2	2. GOVT ACCESSION NO.	3. RECIPIENT'S CATALOG NUMBER 14 TR-79-12
4. TITLE (and Subtitle) 6 DEFT: Advanced Structures and Applications	5. TYPE OF REPORT & PERIOD COVERED 9 Final Report 10 Jun 77 - Mar 79	
7. AUTHOR(s) 10 Stephen T. Kowel, Philipp G. Kornreich, Amaresh Mahapatra, Dennis Cleverly, Thomas Szebenyi, and Akbar Nouhi	8. CONTRACT OR GRANT NUMBER(s) 15 DAAG53-76-C-0162	
9. PERFORMING ORGANIZATION NAME AND ADDRESS Syracuse University 406 737 Electrical and Computer Engineering, 111 Link Hall Syracuse, NY 13210	10. PROGRAM ELEMENT, PROJECT, TASK AREA & WORK UNIT NUMBERS 16 15762709DH95 DA OD 3426	
11. CONTROLLING OFFICE NAME AND ADDRESS US Army Night Vision and Electrooptics Laboratory DRSEL-NV-SD Ft. Belvoir, VA 22060	12. REPORT DATE 11 30 June 79	
14. MONITORING AGENCY NAME & ADDRESS (if different from Controlling Office) 12 102 L	13. NUMBER OF PAGES 97	
15. SECURITY CLASS. (of this report) unclassified		15a. DECLASSIFICATION/DOWNGRADING SCHEDULE
16. DISTRIBUTION STATEMENT (of this Report) Approved for public release; distribution unlimited.		
17. DISTRIBUTION STATEMENT (of the abstract entered in Block 20, if different from Report) DDC RECEIVED OCT 23 1979 RECEIVED A		
18. SUPPLEMENTARY NOTES Principal Investigators: Stephen T. Kowel, Philipp G. Kornreich		
19. KEY WORDS (Continue on reverse side if necessary and identify by block number) optics spectral analysis acoustooptics image transducers surface acoustic waves image convolvers Fourier theory image analysis		
20. ABSTRACT (Continue on reverse side if necessary and identify by block number) During the period covered by this report, major progress was achieved in several areas, including the CdS sensor, light valve, and applications. The major impetus to this work is the desirability of a real-time, programmable sensor for use in image and signal processing. The basic result from any of these devices is a detected electronic signal current. of the form		

DD FORM 1 JAN 73 1473

EDITION OF 1 NOV 65 IS OBSOLETE

Unclassified

SECURITY CLASSIFICATION OF THIS PAGE (When Data Entered)

406 737

xlh

Unclassified

SECURITY CLASSIFICATION OF THIS PAGE(When Data Entered)

20.

$$I(t) = \iint E_{1z}(x \pm vt) I(x,y) E_{2z}(y \pm vt) dx dy$$

where E_{1z} and E_{2z} represent travelling disturbances, I is an image intensity at the sensor plane (x,y) .

The 30 MHz CdS/LiNbO₃ sensor can now be routinely fabricated as a monolithic structure, using a metallized polymer pedestal for sampling. This permits the device to be incorporated in a camera-like box with a highly convergent commercial lens for use under typical incoherent illumination conditions. Such sensors have been incorporated into delivered hardware by DEFT Laboratories, Inc., East Syracuse.

Extensive effort has led to the successful operation of both 35 MHz and 100 MHz devices based on our experience with the 30 MHz structure. Beyond the extra care required during the photolithography in order to obtain the three-fold increase in resolution, we had to overcome an excessively large acoustic loss encountered at the higher frequencies. While our results are encouraging, we have in mind several important refinements.

We have also succeeded in fabricating a two-dimensional light valve, capable of performance comparable to the 30 MHz sensor. This is the first analog light valve structure capable of two-dimensional processing in incoherent light.

Current efforts are aimed at significant reductions in the acoustic standing wave ratio associated with the bulk longitudinal waves used in this valve.

The third major area of effort has been in further developing our ideas on "signal design." In this report, we discuss both continuous decomposition (Fourier transforms, spatial raster scanning, signal and image convolution) and discrete decomposition (generalized matrix inner products, Hadamard transforms). Thus, the DEFT sensors emerge as unusually flexible analog devices. They are capable of programmed operation, obtaining image and signal parameters in a real-time, random-access mode.

Accession For	
NTIS G-XXI	<input checked="checked" type="checkbox"/>
DDC TAB	<input type="checkbox"/>
Unannounced	<input type="checkbox"/>
Justification	
By	
Distribution/	
Availability Codes	
Dist.	Avail and/or special
A	

Unclassified

SECURITY CLASSIFICATION OF THIS PAGE(When Data Entered)

TABLE OF CONTENTS

I. Introduction.....	1
II. Monolithic Sensors.....	3
II.1 Monolithic Device--Fabrication.....	3
II.2 Experimental Results/30 MHz Sensor.....	10
II.3 Acoustics--Study of Spurious Modes.....	11
II.4 Cadmium Sulphide: Its Properties and Preparation.....	12
II.5 Design and Fabrication of a 100-MHz Device.....	13
II.6 Experimental Results Using the 100 MHz Sensor.....	15
III. Implementation of the Light Valve Concept.....	17
IV. Applications: The Programmable Processor.....	18
V. Publications and Patents.....	20
VI. Conclusions.....	21
Appendix I. The Vector Imaging Convolver.....	22
Appendix II. Double-Layered Polycrystalline Cadmium Sulfide on Lithium Niobate.....	29
Appendix III. Modulation of Current in a Thin Film of Lead Tin Selenide by Bulk Acoustic Waves.....	36
Appendix IV. Strain-Induced Modulation of Photoconductivity in Thin Polycrystalline Films of Cadmium Sulfide.....	39
Appendix V. Spurious Acoustic Modes in Two-Dimensional Fourier Transform Devices.....	54
Appendix VI. Monolithic Two-Dimensional Fourier Transformer.....	60
Appendix VII. A Two-Dimensional Acoustic Processor.....	67
Appendix VIII. Two-Dimensional Photoacoustic Image Processing with Longitudinal Waves.....	73

TABLE OF CONTENTS (Continued)

Appendix IX.	
Image Feature Analysis Using DEFT Sensors.....	79
Appendix X.	
A Programmable, Multi-Function Processor.....	86
Appendix XI.	
Patent Rights.....	95

I. Introduction

During the period covered by this report, major progress was achieved in several areas, including the CdS sensor, light valve, and applications.

The major impetus to this work is the desirability of a real-time, programmable sensor for use in image and signal processing. The basic result from any of these devices is a detected electronic signal current of the form

$$I(t) = \iint E_{1z}(x \pm vt) I(x,y) E_{2z}(y \pm vt) dx dy \quad (1.1)$$

where E_{1z} and E_{2z} represent travelling disturbances, I is an image intensity at the sensor plane (x,y) .

The 30 MHz CdS/LiNbO₃ sensor can now be routinely fabricated as a monolithic structure, using a metallized polymer pedestal for sampling. This permits the device to be incorporated in a camera-like box with a highly convergent commercial lens for use under typical incoherent illumination conditions. Such sensors have been incorporated into delivered hardware by DEFT Laboratories, Inc., East Syracuse.

Extensive effort has led to the successful operation of both 35 MHz and 100 MHz devices based on our experience with the 30 MHz structure. Beyond the extra care required during the photolithography in order to obtain the three-fold increase in resolution, we had to overcome an excessively large acoustic loss encountered at the higher frequencies. While our results are encouraging, we have in mind several important refinements.

We have also succeeded in fabricating a two-dimensional light valve, capable of performance comparable to the 30 MHz sensor. This is the first analog light valve structure capable of two-dimensional processing in incoherent light. Current efforts are aimed at significant reductions in the acoustic standing

wave ratio associated with the bulk longitudinal waves used in this light valve.

The third major area of effort has been in further developing our ideas on "signal design." In this report, we discuss both continuous decomposition (Fourier transforms, spatial raster scanning, signal and image convolution) and discrete decomposition (generalized matrix inner products, Hadamard transforms). Thus, the DEFT sensors emerge as unusually flexible analog devices. They are capable of programmed operation, obtaining image and signal parameters in a real-time, random-access mode.

This report is based on a number of papers published and read during the past eighteen months. The remaining sections of this report rely heavily on these papers, furnished as appendices.

The authors wish to thank Mr. David Helm of the Night Vision and Electro-optics Laboratory for his encouragement during this contract. We also acknowledge the interest of Mr. Joseph Hannigan of the U.S. Army Engineer Topographic Laboratory. His successful application of DEFT sensors to camouflage measurement should encourage others to experiment with DEFT technology for other applications.

We also wish to thank Mr. William Penn, of the Electronics Laboratory, General Electric Company, and Dr. Samuel Craig of DEFT Laboratories, Inc., for many technical contributions.

II. Monolithic Sensors

II.1. Monolithic Device--Fabrication

As discussed in our report of June 1977, a major problem encountered in the fabrication of the two-dimensional DEFT device is the incorporation of a sampling grid. We mentioned that one way to do this is to etch the CdS into strips of appropriate width perpendicular to the metal sensor lines. However, this results in discontinuities in the sensor lines at the edges of the CdS strips. In fact, at that stage of the project, we were unable to fabricate a monolithic device and were forced to use a suspended sampling grid. This had the disadvantage that the sampling grid was at a finite distance from the CdS film. A highly convergent focussing lens would cause "undercutting." That is, the image would be obliterated by the poorly defined shadow of the grid. Thus, the device would work only with a well collimated light beam such as that from a laser.

Since that time, we have developed a new technique for fabricating a monolithic sampling grid. This technique necessitates only three additional steps in the photolithography process. It has worked remarkably well for 30 MHz devices. At higher frequencies it may not be appropriate since it does entail additional mass loading of the surface.

It was clear at the outset that one method of sampling the image would be to lay down a thin layer of a transparent insulator on top of the sensor area and fabricate opaque metal strips perpendicular to the sensor lines on top of the insulator. However, the sampling lines would capacitively couple the sensor lines and short out much of the a.c. signal current. In order to prevent this, it would be necessary to further etch the sampling lines into squares located exactly between the sensor contact lines as shown in Fig. (II.1). The problem, therefore, was the fabrication of such precisely aligned squares with the use of simple photolithographic processes.

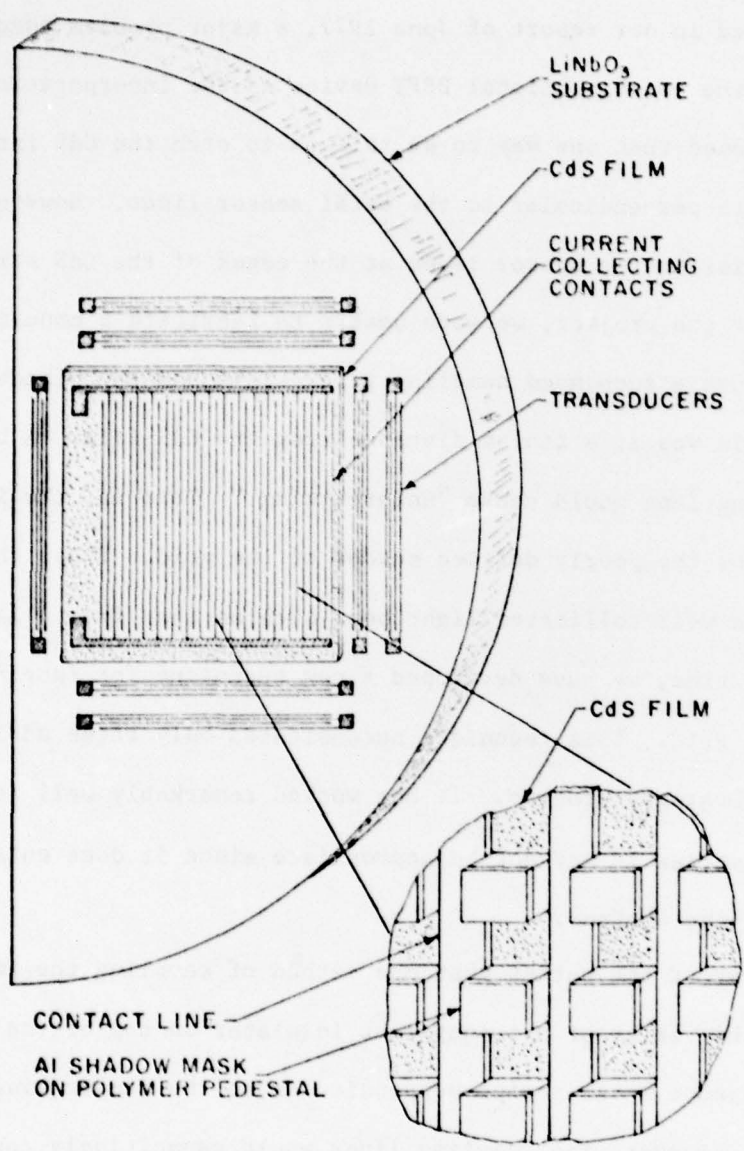


Fig. (II.1) DEFT Sensor showing sampling grid on polymer pedestals. The substrate is one half of a two-inch LiNbO_3 wafer.

This was accomplished as follows. After the sensor pattern and transducers had been fabricated on the LiNbO_3 substrate, a film of positive photoresist (Shipley 1350J) was spun on top of the substrate. This film was used as the insulating layer. Next a thin film of Al was evaporated on top of the sensor area so that only the transducers were visible through the photoresist. A second layer of photoresist was spun on to the substrate. Now, the thick master mask consisting of the sensor pattern and transducers was positioned over the substrate and aligned to coincide exactly with the pattern on the substrate. It was possible to do this since the transducers on the substrate were still visible. After alignment the transducers in the master mask were covered and the substrate was suitably exposed to UV light. Next the master mask was rotated by 90° and aligned so that the sensor lines in the master mask were perpendicular to the sensor lines on the substrate. The transducers were again covered and the substrate exposed a second time.

As a result of these steps, the transducers on the substrate were protected by unexposed photoresist. The Al on the sensor area, however, was covered only with squares of unexposed photoresist. Moreover, the squares were located precisely between the sensor lines because of the exact alignment of the master mask. Now, we developed the photoresist and etched the Al in dilute NaOH solution to generate the desired pattern of squares. As a last step, the sensor pattern was suitably covered and the rest of the area exposed to UV light and developed so that the transducers no longer had photoresist on them.

Clearly, the reason this technique works is that while the main sensor pattern is produced by "lift-off" the sampling pattern is produced by etching. Therefore, though the mask used in both cases is the same and is aligned to the same position, the squares of the sampling grid are located precisely between the lines of sensor pattern. Clearly, precise alignment of the master mask in the last few steps is crucial.

The devices with center frequencies of 100 MHz were not fabricated by this procedure, although it should be possible to do so. Instead of the polymer pedestal, the CdS film was etched to provide sampling. This was accomplished by etching away a periodic array of squares of CdS so that the "holes" are always between the contact lines.

This technique is somewhat simpler than that involved with building the polymer pedestals and produced very fine 100 MHz devices.

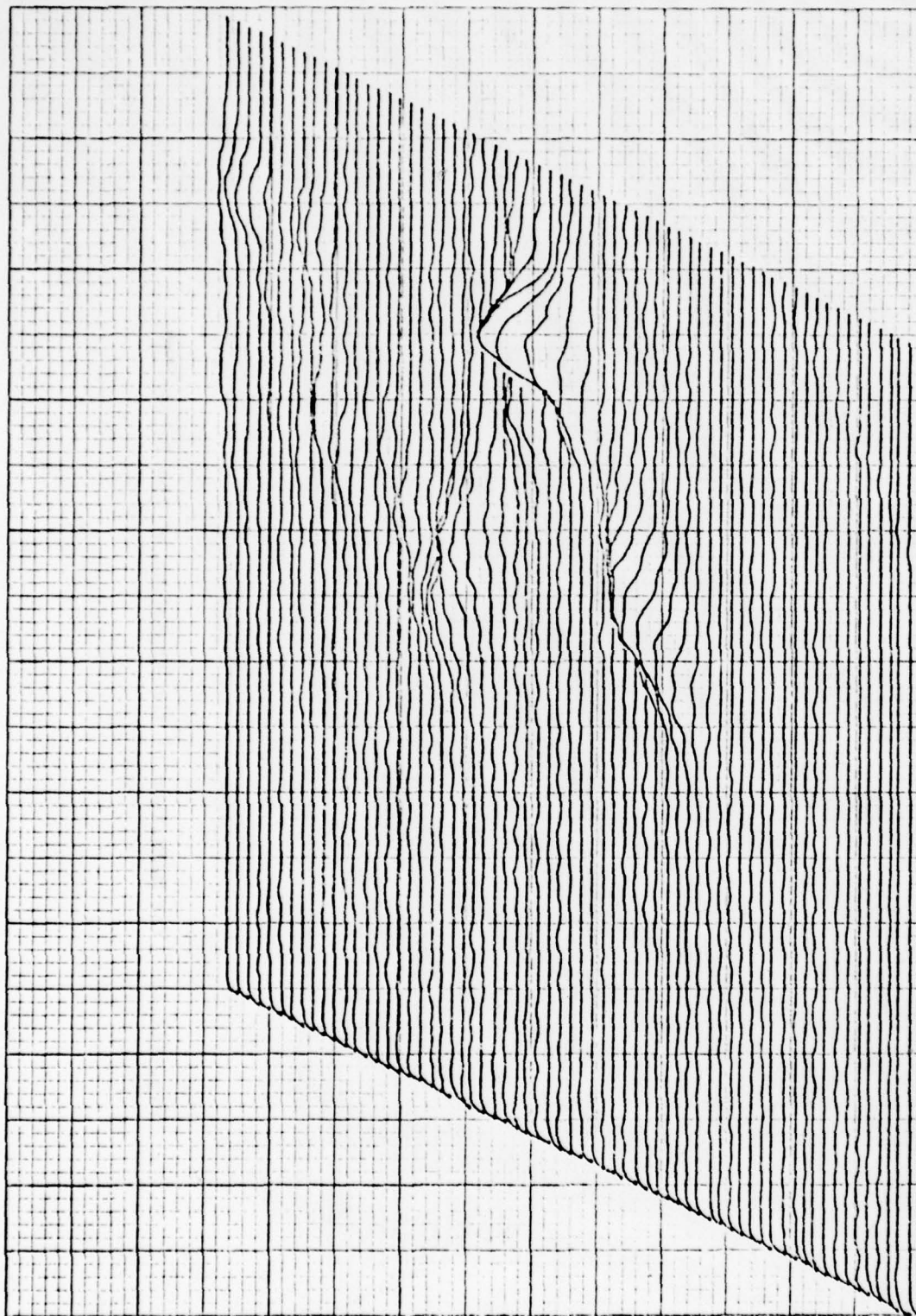


Fig. (II.2) Results obtained using a "35 MHz" DEFT sensor operated by microcomputer.
The horizontal axis spans frequencies between 33.46 MHz and 41.10 MHz,
while the vertical axis spans between 29.06 MHz and 36.70 MHz.

(a) Magnitude of the transform of a chevron pattern.

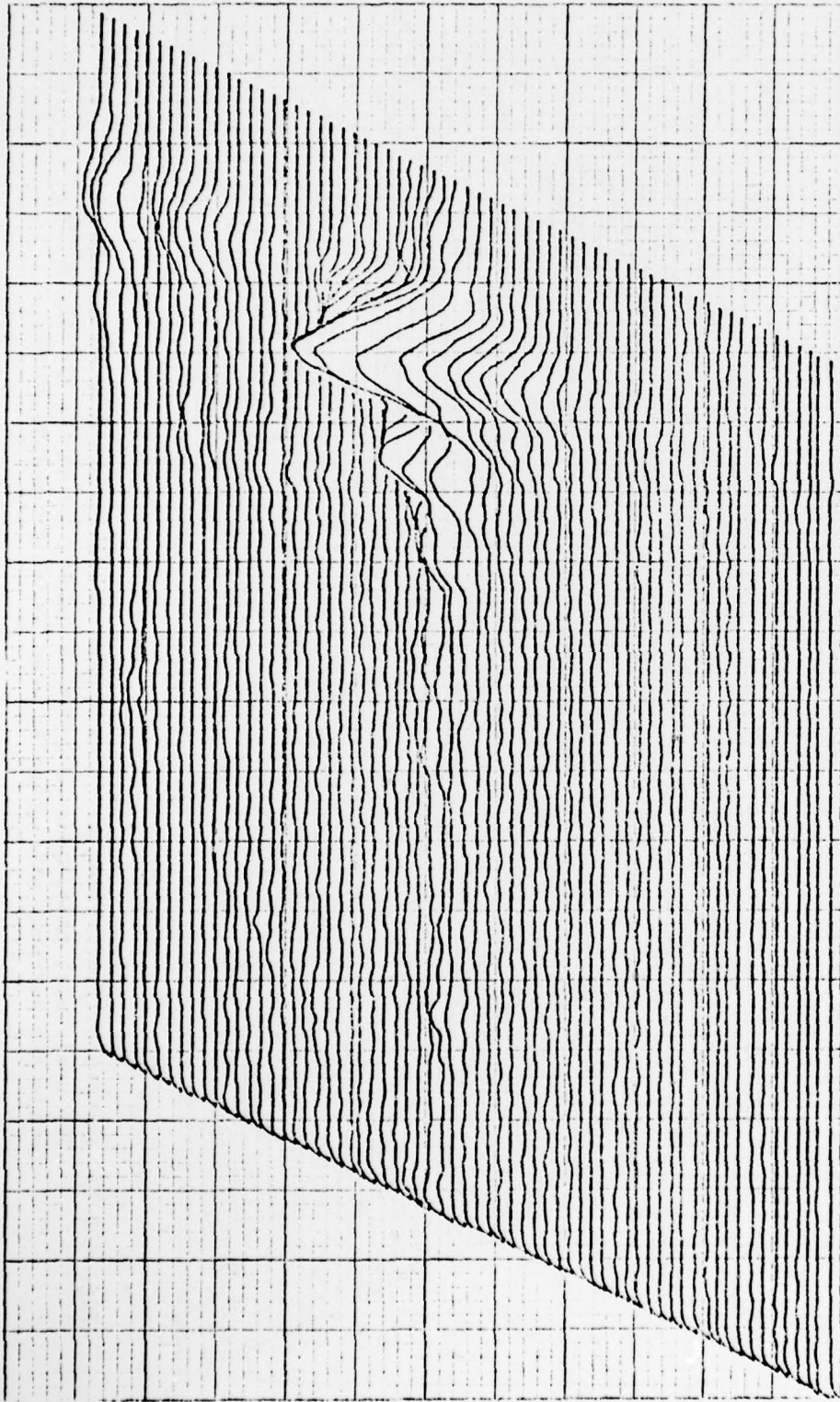


Fig. (II.2b) The magnitude of the transform of the letter "T".

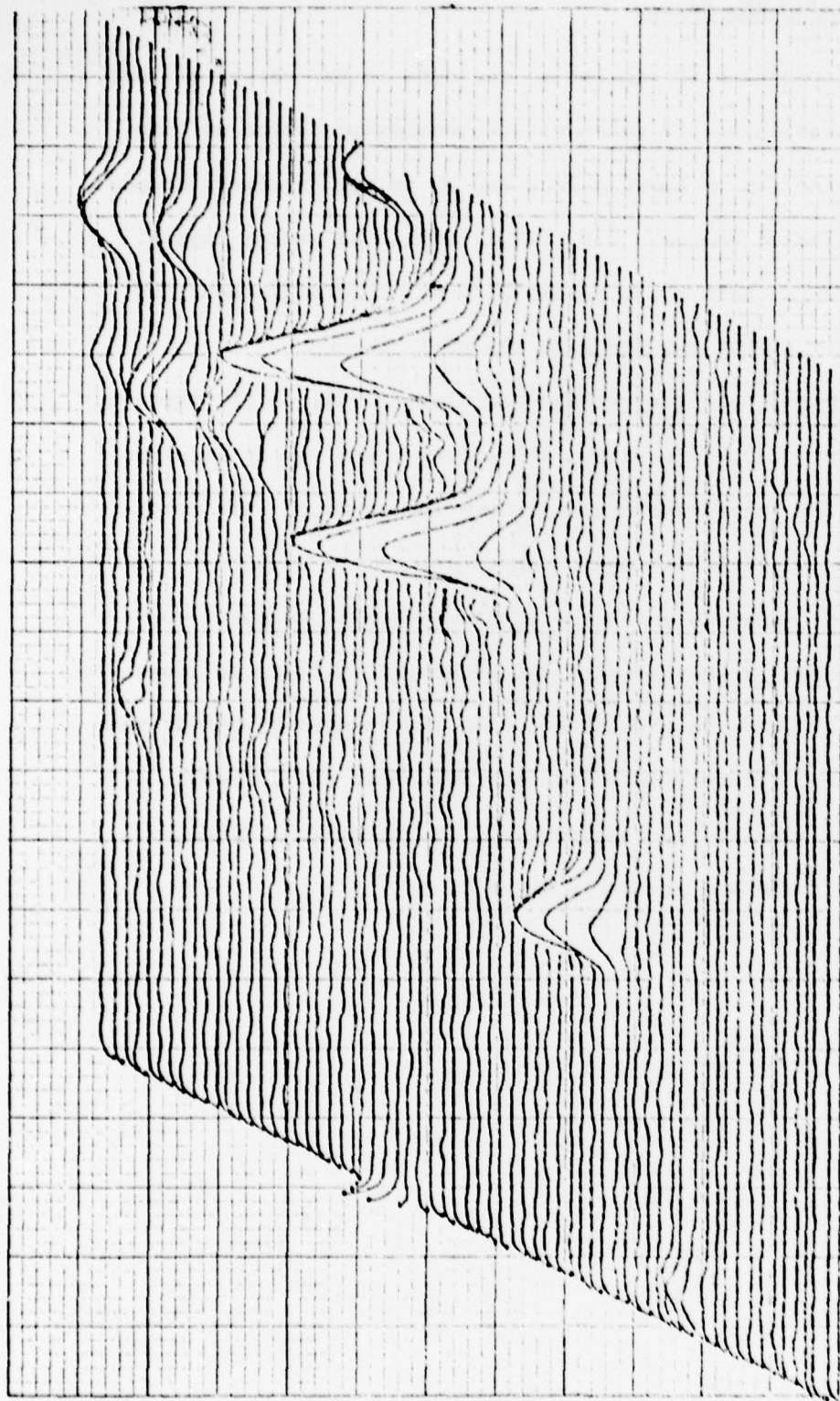


Fig. (II.2c) The magnitude of the transform of a bar-pattern image. The largest peak represents the "d.c.", or average value component. The large peak next to it represents the fundamental frequency of the pattern. Two other peaks in the lower left quadrant can be discerned on a line joining the d.c. and fundamental. The larger is the third harmonic; the smaller the fifth harmonic of the fundamental frequency.

The small cluttered peaks in the upper right quadrant are caused by spurious acoustic modes in the substrate.

II.2. Experimental Results/30 MHz Sensor

Much of the data reported here is similar to the data in our report of June, 1977. The difference is that these are taken with a monolithic device so that the image was focussed on the sensor using a lens and it is not necessary to use a laser beam or other collimated source. Fig. (II.1) shows the sensor layout.

All the experimental data confirm the possibility of performing focus and motion detection, and contrast measurements with the DEFT sensors.

In Appendix IX, Sections 3, 4, 5, 6, we show results on various bar pattern images, including focus and motion detection. The linear phase versus displacement curve shown in Fig. 5 of Appendix IX demonstrates the acoustic uniformity and precision available for position and motion detection.

Appendix X describes a system in which the sensors are microcomputer controlled and the image spectrum is then sampled and displayed yielding an isometric representation. Fig. (II.2) shows results obtained on this microcomputer-driven system developed at Deft Laboratories, Inc. Appendix VI shows similar data obtained by manually controlling the sensor drivers. In Appendix I, results for manual rotation of the image are presented as well.

II.3. Acoustics--Study of Spurious Modes

Recent work done with the DEFT sensor revealed evidence for the existence of more than one acoustic mode in our monolithic layered structures. It was found that there was at least one additional acoustic mode along each axis having a velocity larger than that of the fundamental Rayleigh mode by about 7%. The presence of these additional modes results in a repetition of the Fourier transform information in the frequency space scanned by the transducers.

While the effect of the additional acoustic modes can be minimized by suitable treatment of the back surface of the substrate, it cannot be eliminated. However, we have developed an advanced device design which entirely eliminates the detrimental effects of these spurious modes. It consists essentially of sampling the image such that the Fourier transform, instead of being shifted to the center of the scanned frequency space, is moved to its upper edge. This results in most spurious d.c. peaks being located outside the scanned frequency space.

This design feature is incorporated in our 100 MHz devices which are described in Section II.5. A detailed study of the spurious acoustic modes is given in Appendix V.

II.4. Cadmium Sulphide: Its Properties and Preparation

During this effort, considerable improvements were made in both film fabrication and in understanding the mechanisms involved in DEFT applications.

In Appendix II, we describe the double-layered technique for producing CdS films developed under this contract. We now routinely produce films with high light-to-dark conductivity ratios (500:1) and good coupling to surface waves. The films have proven physically and electrically stable over periods of several years.

In Appendix IV we describe the results of a major study of the mechanism of elastophotoconductivity, used in previous glass-substrate devices. Based on this successful study, we are presently at work on a companion theory of the electrophotoconductivity.

The theory developed is original and quite distinct from previous work. Most studies to date relied on constant, uniaxial strain measurements. In the theory often quoted on thin film devices using strain, interaction depends primarily on "barrier" effects between adjacent crystallites. The theory developed under the contract utilizes a quasicontinuous distribution of impurity levels in the forbidden gap, which is shifted due to strain.

Appendix III briefly relates experiments done which demonstrated the elastophotoconductivity effect in a thin film of lead tin selenide. It is hoped that future activity with infrared sensitive materials will be performed in order to evaluate the potential for DEFT sensors in the infrared.

II.5. Design and Fabrication of a 100-MHz Device

As a result of our work with the 30 MHz DEFT sensor, the following drawbacks were evident:

(a) Since the center frequencies of the x and y transducers were equal, the $\omega_1 = \omega_2$ line passed diagonally through the frequency space scanned by the transducers. Signals on this line could not be detected since they corresponded to a difference frequency of zero. Thus, this section of the Fourier spectrum could not be explored.

(b) As a result of the spurious acoustic modes mentioned earlier, the d.c. peak appeared at several locations within the scanned frequency space instead of appearing just at the center. As a result, the Fourier spectrum of any optical image also appeared centered around all these locations. This resulted in considerable overlapping of signals and difficulty in their analysis.

(c) The bandwidth was limited to about 8 MHz x 8 MHz at best.

Thus, we designed a 100 MHz device with an offset frequency space. This device would have different center frequencies in the two directions and different sampling frequencies so that the entire scanned space would consist of unique spatial frequencies (rather than having one-half redundant) while moving $\omega_1 = \omega_2$ outside of the scanned space. After a number of unsuccessful experiments, we were able to identify several problems:

- 1) Random scratches on the LiNbO_3 severely scattered the surface waves.
- 2) The CdS film excessively attenuated the surface waves. All signals observed were due to a complex pattern of bulk waves. When the bulk waves were absorbed by tape on the back of the substrate, no signals were observed.
- 3) The transducers had high insertion loss due to their increased aperture/wavelength ratio.

We have now produced working 100 MHz devices by overcoming these difficulties. Greater care in processing produced substrates without blemishes.

Acceptable SAW throughput (26 db, including insertion losses and propagation losses) was obtained by fabricating thicker transducers to decrease their electrical loss, and by fabricating a thinner CdS film ($\sim 0.5 \mu\text{m}$). These two improvements resulted in an improvement of about 27 db.

Further improvement was obtained by using the etching technique to remove a periodic array of squares of CdS, since this is simpler than the polymer pedestal image sampling technique.

II.6. Experimental Results Using the 100 MHz Sensor

Our first successful experiments using the 100 MHz sensors involved using the two adjacent transducers, resulting in unidirectional Fourier transform data. The device produced excellent spectral linearity over the bandwidth. The results are recounted in Appendix X, Section V. Fig. 5 of Appendix X shows the linear variation of measured temporal difference frequency as a function of spatial frequency in the image.

Our last experiments involved full two-dimensional operation. These were highly encouraging. Bar patterns were rotated and the spectral peaks tracked by varying the two drive frequencies.

Fig. II.3 shows the results obtained for three different bar patterns. The outermost arc corresponds to a magnitude of approximately 40 lines/cm at the sensor. The arcs were all drawn with a compass centered at (114.8 MHz, 88.6 MHz). The data points all fall extremely close to the ideal arcs.

We believe that these results can be improved considerably by judicious choice of electronics, including drivers and detectors. Of particular concern in obtaining the design bandwidth of (15 MHz x 15 MHz), is the introduction of a sweeping synchronous detector to avoid the tedious acquisition of data using the spectrum analyzer.

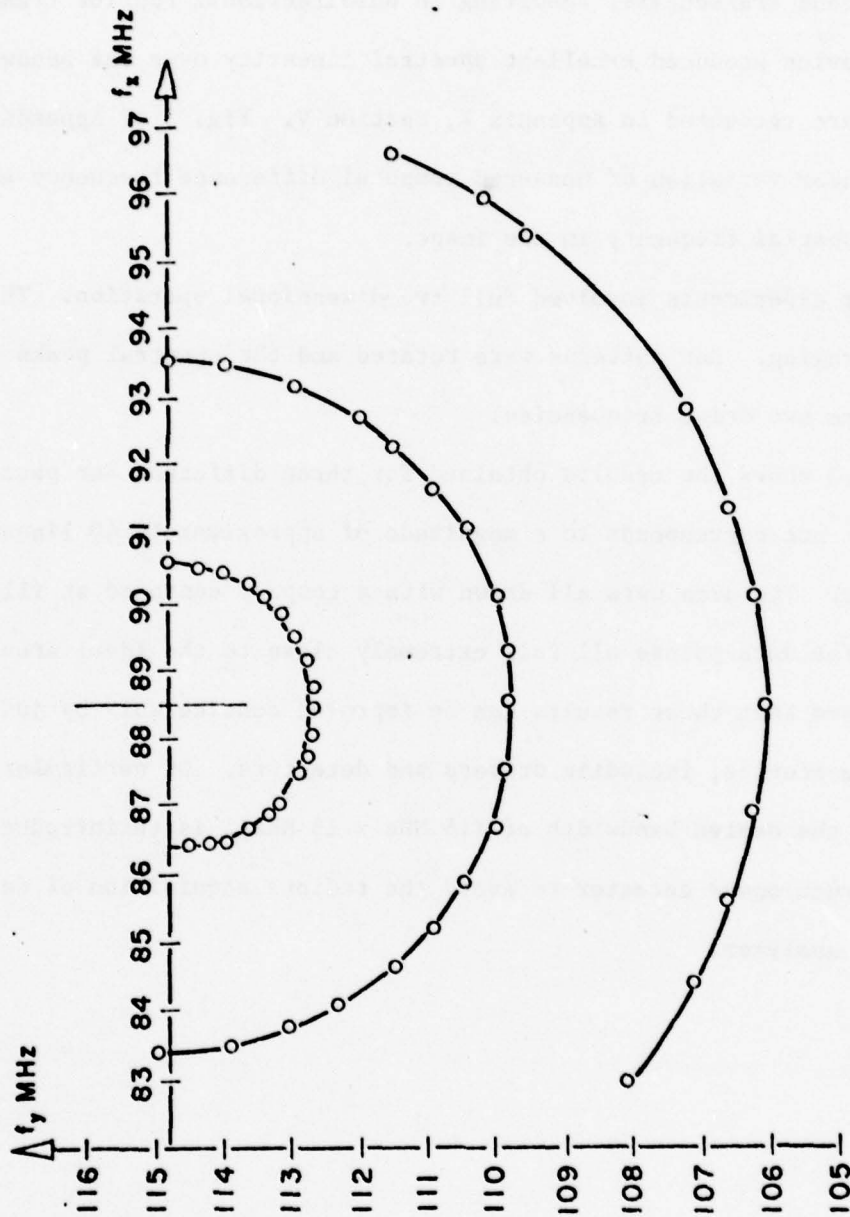


Fig. (II.3) Rotation of three bar patterns tracked electronically.

III. Implementation of the Light Valve Concept

During this last year, we fabricated a two-dimensional fused quartz light valve capable of measuring the Fourier transform components of an image. Appendices VII and VIII describe the theory, construction, and experimental results obtained. The system demonstrated pseudo-beam steering, had slightly greater resolution than the 30 MHz CdS sensor, and had the expected fast response to light, limited only by the commercial photodetector.

We are currently working to reduce the high standing-wave-ratio by further sandblasting of reflecting edges and by adding epoxy for damping.

IV. Applications: The Programmable Processor

We have continued to study a wide range of applications for DEFT systems. In particular, we have investigated the possibility of flexible, programmed operation of a DEFT sensor utilizing different orthogonal, but separable, decompositions. These include Fourier transforms, video raster scanning, Hadamard transforms, etc. DEFT Laboratories, Inc., now has a working microcomputer system for synthesizing driven signals and storing and displaying the resulting decomposition.

As we recognized earlier, there is considerable flexibility in operating the devices. By choosing the class of functions used to excite the transducers, other decompositions of the imaged light intensity may be obtained. If E_{1z} , E_{2z} , in (1.1) are not constant, but slow modulation signals, we can obtain the " E_{1z} , E_{2z} " decomposition. For example, suppose that $E_{1z}(x) \propto \delta(x)$, $E_{2z}(y) \propto \delta(y - a)$, two short pulses. Then the resulting current would be

$$i(t) \propto I(vt, vt - a) \quad (4.1)$$

where v is the speed of sound. Thus, a diagonal line of the image is raster scanned. By varying the delay, a , any line can be scanned. Here the signal is proportional to the light intensity at each point, rather than proportional to a Fourier component of the light intensity.

In fact, it is illustrative to look at the response signal in the form

$$i(t) \propto \iint f_1(x \pm vt) I(x, y) f_2(y \pm vt) dx dy \quad (4.2)$$

as a convolution/correlation of $f_1(t)$ with $f_2(t)$ weighted by $I(x, y)$.

This shows that the device has three programmable input ports (two electronic, one optical) and one output port (electronic) and can produce a variety of output information as a function of these three input ports.

The general result can also be put in discrete form

$$i_{lk} \propto \sum_{n,m} f_{1,lm} I_{mn} f_{2,nk} \quad (4.3)$$

where $f_{1,lm}$ is the phasor value of the x-directed wave envelope associated with the l th kernel function of the decomposition, and measured at the m th image position in the x-direction, etc. I_{mn} is the image intensity at the (m,n) position.

Thus, by appropriate encoding, we should be able to measure this generalized inner product in which the functions f_1 and f_2 are multiplied by a weighting function I_{mn} . In fact, if I_{mn} is a diagonal line, we are performing matrix multiplication.

The impact of this flexibility is that a number of recognition algorithms could be implemented using the same DEFT device. The device views the image and quickly decomposes it into any of a number of test functions for comparison with stored results, etc.

Theory and experimental results are included in Appendix X, Sections 3, 4, and 5.

It should be noted that the kernel functions f_1 and f_2 need not be chosen exclusively from a known orthogonal, complete set. One could start by evaluating isolated topographic features, such as roads, lakes, etc., by video scanning. Once this information has been stored, it can be used to modulate the transducers, permitting a "window scan correlation" mode of operation. That is, the acoustooptic system would report the result of successive correlations of the new picture with the different reference items. The result would indicate which feature had been recognized, and where it was found.

V. Publications and Patents

In addition to the papers included in the appendices, this contract period saw many patents issued on this technology. A list is included as Appendix XI.

Also, during this period, Mr. Joseph Hannigan, U.S. Army Engineer Topographic Laboratories (USAETL-RI), presented a paper entitled, "Direct Electronic Fourier Transforms (DEFT) for Camouflage Signature Measurement (CSM)" at the Army Science Conference, West Point, New York, in June 1978. He received an Outstanding Achievement Medallion for the paper and the work was described subsequently in TECH TRAN, Fall 1978, Vol. 3, #4, published by U.S. Army Corps of Engineers.

VI. Conclusions

The work performed during this contract has clearly indicated that DEFT technology has promise for a wide variety of image and signal processing functions.

A two-dimensional DEFT sensor, operating around 100 MHz, should be a versatile information-processor capable of resolving about 5000 image or transform points. Synchronous detection should permit a dynamic range greater than 60 db, and allow phase as well as amplitude measurements.

In the future, devices with still higher center frequencies should be attempted. Improvements to the thin film and acoustic aspects of the technology need more study. A two-dimensional processor needs an enormous acoustic aperture-to-wavelength ratio, resulting in poor transducer radiation efficiency. The CdS films need to be thinner, more uniform, and smoother to avoid attenuation.

The light valve technology is also promising. Higher frequencies need to be achieved, probably by fabricating thin-film piezoelectric transducers.

By fabricating infrared sensitive films or diode arrays, the technology could be extended beyond the visible regime as well.

APPENDIX I.

THE VECTOR IMAGING CONVOLVER

1977 Ultrasonics Symposium Proceedings,
IEEE Cat. #77CH1264-1SU

THE VECTOR IMAGING CONVOLVER

S.T. Kowel, P.G. Kornreich, A. Mahapatra, B. Emmer, M. Mehter, and P. Reck
Dept. of Electrical and Computer Engineering
Syracuse University, Syracuse, New York 13210

ABSTRACT. We have fabricated an acoustooptical sensor capable of two-dimensional image or signal processing. It is a monolithic, optically addressed convolver, except that the two transducers propagate orthogonal, rather than colinear, surface waves. The interaction between image, acoustics, and electrons is obtained in a thin, polycrystalline film of CdS deposited on z-cut LiNbO₃. A double-layer technique produces reproducible, stable films with a 20% modulation of the photoconductivity proportional to the square of the SAW electric field. The signal current is detected by an interdigital contact pattern, made from an In/Al film sandwich deposited on the CdS.

With sinusoidal inputs, we obtain a difference frequency signal proportional to the spatial Fourier transform of the optical pattern focussed on the film. By varying the driving frequencies, we perform a vector scanning in Fourier space. Image rotation can be tracked electronically over a full 360°. The sensor can detect the spatial frequency, orientation, and amplitude of variations in the optical intensity. Phase measurements of the Fourier components, made by comparing the signal with an electronically synthesized difference frequency, show the expected linear variation with frequency, and the linear variation with displacement.

Introduction

The electronic transduction of image information has necessarily relied on raster scanning of the optical intensity. Vidicons use electron beams; CCD's use moving charge packets; raster scanners move a light beam from point to point. Of course, coherent processors can take the Fourier transform of the image, but as yet no one has succeeded in encoding this information electronically, including magnitude and phase data, in real time.

Moreover, the amount of data in a high contrast, high resolution, picture is so large that even a powerful computer cannot compute full two-dimensional transforms of the raster lines. A series of one-dimensional transforms does not possess many of the properties of the transform of the picture.

Thus it is necessary to use very sophisticated electronic systems to perform information processing functions such as Fourier transformation, correlation, motion detection, noise reduction, and pattern recognition. We have studied several of these areas of image processing and reported a variety of results [1-9] using DEFT (Direct Electronic Fourier Transform) sensors.

We have succeeded in fabricating a sensor whose successors have the potential of providing many image processing functions in real-time without spatial raster scanning. The sensor makes use of a photoconducting film deposited on a piezoelectric substrate. Two orthogonally directed surface acoustic waves, launched by deposited interdigital transducers, create a significant modulation of the image-induced charges, creating an electronic signal of the general form

$$i(t) = \iint I(x, y) f_1(x \pm v_1 t) f_2(y \pm v_2 t) dx dy \quad (1.1)$$

where $i(t)$ is a current detected by interdigital contacts laid over the film, $I(x, y)$ is the image intensity, and $f_1(t)$ and $f_2(t)$ are electronic signals used to generate the acoustic waves.

The most natural application of (1.1) occurs when $f_1(t)$ and $f_2(t)$ are sinusoids. In this case, $i(t)$ corresponds to an arbitrary component of the two-dimensional Fourier transform of the image intensity. By varying the transducer driving frequencies, the entire transform can be obtained including magnitude and phase. Thus the sensors are called Direct Electronic Fourier Transform devices (DEFT).

If the transducer driving voltages are chopped into short pulses, varying the pulse timing between transducers will have the effect of raster scanning of the image. By appropriate signal design, still other imaging modes can be obtained.

"1977 Ultrasonics Symposium Proceedings, IEEE Cat. #77CH1264-1SU"

Furthermore, in uniform light, the devices can perform correlation and convolution of input electronic signals as implied by (1.1).

In order to take full advantage of SAW Fourier imaging, it is essential to be able to electronically select arbitrary, two-dimensional, Fourier components of arbitrary, two-dimensional images. Previous work has been largely confined to obtaining one-dimensional transforms of one-dimensional [10,11] or two-dimensional images [1,6,7]. Various techniques have been proposed [1,12] for achieving full two-dimensional capability, culminating in the development of the pseudo beam steering technique discussed here [4,8,9].

Two surface acoustic waves, travelling perpendicularly, cross the image, focussed on a thin photoconductive film of CdS. The modulation of the photoconductivity is strongly dependent on applied electric field, with the generated photocurrent having a component proportional to the square of the electric field. We provide the electric fields by propagating the two crossed surface acoustic waves on a piezo-electric substrate (LiNbO₃) on which the CdS has been deposited. A full tensor treatment of the interaction [13] reveals that the deposited contacts detect a current proportional to

$$i(t) = \iint dx dy E_z^2(x, y, t) I(x, y) \quad (1.2)$$

where $I(x, y)$ is the image intensity, x and y are the coordinates on the film, and E_z is the electric field perpendicular to the plane.

Since

$$E_z = E_{1z} \cos(\omega_1 t - k_1 x) + E_{2z} \cos(\omega_2 t + k_2 y) \quad (1.3)$$

where E_{1z} , ω_1 , k_1 , refer to the x-directed acoustic wave and E_{2z} , ω_2 , k_2 , refer to the y-directed acoustic wave, E_z^2 contains a term of the form

$$E_{zd}^2 = E_{1z} E_{2z} \cos[(\omega_1 - \omega_2)t - (k_1 x + k_2 y)] \\ = E_{1z} E_{2z} \cos[\omega_1 - \omega_2)t - \vec{k} \cdot \vec{r}]. \quad (1.4)$$

By varying the driving frequencies, we can vary \vec{k} , yielding a signal term proportional to the two-dimensional Fourier transform,

$$i_s(t) = \exp[j(\omega_1 - \omega_2)t] \int d^2 \vec{r} I(\vec{r}) \exp(-j \vec{k} \cdot \vec{r}) \quad (1.5)$$

while the other terms from (1.2) can be ignored because they are at different frequencies. That is, the signal behaves as if a new acoustic wave has been created with wavevector equal to the sum of the excited wavevectors. Thus we call this effect "pseudo beam steering."

From theoretical considerations alone, pseudo beam steering by conductivity modulation is likely to be far superior to other proposed techniques for accomplishing two-dimensional imaging. For example, the actual creation of a third surface wave from nonlinear mixing appears to be a much smaller and less controllable effect.[12]

The use of high frequency surface wave transducers requires that the image be placed on a high spatial frequency carrier. This is accomplished in one direction by the interdigital contact pattern used to detect the signal, and in the perpendicular direction by either etching the CdS into strips, or by projecting the image through a grid.

Quantitative measurements of spatial frequencies, amplitude and phase behavior are described. Convincing evidence of the pseudo-beam steering behavior is found in the data on image rotation. In these experiments, the physical rotation of an object, focused on the sensor, results in the expected disappearance of the Fourier component signal. The requisition of the signal by appropriate change of the transducer frequencies permitted the component to be tracked during a full 360° rotation.

II.1 Principles of Operation

The image sensor consists of a CdS film deposited on a z-cut LiNbO₃ substrate, as shown in Fig. 2.1. Thin film metal contacts, in the form of an interdigital pattern, are deposited onto the CdS film. This pattern permits the collection of the total photocurrent over the area of the CdS film.

Besides providing electrical contact, the contacts also form a coarse grating across the image. This, in effect, shifts the Fourier transform of the image along the k_y direction to higher spatial frequencies. It allows us to generate the Fourier transform of the image with SAW's having a limited bandwidth. A similar effect is obtained by etching the CdS film into strips along the x direction. We here use, for simplicity, gratings with equal dark and light spacings. Unfortunately, this type of grating only exposes 1/4 of the CdS film to the image. Larger film exposures are possible by making the dark areas of the masks narrower.

The effect of the contact pattern and the etching of the CdS (or the projection of the image through a grid perpendicular to the contact lines) is to multiply the image intensity by a sampling grid function, and by an aperture function, to form the sensed image. The principal effect of this two-dimensional sampling is to put the original image on a spatial carrier whose period is in both the x and y directions respectively. It is reasonable to assume that the image only varies appreciably over several squares. The effect of the finite device size is to smooth the "reduced" Fourier space with a sinc function which is reduced to 1% of its center value at the edge of the "reduced" spatial frequency space centered at $1/a, 1/a$. The main lobe has a bandwidth of 1% of the center frequency which implies that data will be smoothed out over one percent of the center frequency. Indeed, this is observed in the devices.

Finally, we give the signal current phasor at the difference temporal frequency ($\omega_1 - \omega_2$) to be[13,14]

$$i = i_{d.c.} \frac{(\sigma_{13}^{LE} + \sigma_{66}^{LE})}{\sigma_d} E_{1z} E_{2z} < \bar{T}_1(g_x, g_y) > \cdot \frac{\sin \pi f_x/2}{\pi f_x/2} \frac{\sin \pi f_y/2}{\pi f_y/2} \quad (2.1)$$

where we introduce standard elasticity notation,[16] and \bar{T}_1 is the smoothed version of the transform of the

image intensity, g_x, g_y are the reduced spatial frequencies, f_x, f_y are the total spatial frequencies, and

$$< \bar{T}_1 > \equiv \bar{T}_1 / \int_{-\infty}^{\infty} dx \int_{-\infty}^{\infty} dy I(x, y). \quad (2.2)$$

Thus we have completed our model showing how the geometry of the sensor when properly coupled to the acoustics yields a two-dimensional Fourier transform of the image. It is interesting to note that the use of the same sampling rate in both directions results in the situation that, for $\omega_1 = \omega_2$, no output is obtained unless very special circuits are employed to measure this d.c. signal. Thus the transform components along the line $g_x = g_y$ will not be obtained. This problem can be avoided by using a/b equal to an irrational number sufficiently large to make this line pass outside of the reduced space. Fig. (2.2) shows the f_x, f_y and g_x, g_y spaces schematically. Next we discuss the experimental confirmation of this theory.

II.2. Two-Dimensional Layered Film Devices

The most difficult task encountered was the production of good photoconductive thin films of CdS on LiNbO₃. Since we had been making such films on glass for several years, we had hoped that the technique for making the films could be used relatively intact.[1,14] However, this is not possible due to the degrading effects of material diffusing out of the LiNbO₃ during curing.

We now insulate the photoconducting CdS film from the LiNbO₃ by a second CdS film. If this film is thick enough it does not permit out-diffused elements from LiNbO₃ to reach the second film of CdS. Moreover, there is no sticking problem at either surface. Our very first experiment with this technique yielded very good L/D ratios. It soon became clear that one could easily adjust the doping levels of HCl, O₂ and Cu for the second CdS film to have L/D ratios of 10⁴ at 200 m.cd.[15]

Since then we have made a number of CdS films on LiNbO₃ by this "double-deposition", or layered, technique.

The "recipe" for evaporating and curing the films has been published elsewhere.[13,14]

Luukkala[11] has made CdSe films on y-cut LiNbO₃ but has reported difficulty in reproducing these films because of cracking and peeling[17]. Solie has made CdS/CdSe films on LiNbO₃ using a somewhat more complicated technique[18,19].

The next step is metallization. Indium makes good ohmic contact to CdS while aluminum, the material normally used in SAW technology, does not. Also, we cannot use the "etching" technique to fashion the metal fingers from the vacuum-deposited metal film. Any etchant that will remove metal will remove CdS. Thus we had to learn a more sophisticated technique known as the "lift-off" method.[20]

Unfortunately, indium films thin enough for lift-off turned out to have a very poor conductivity. This is a serious problem because of the length of our finger patterns (1.2 cm). We solved this problem by a thin film of aluminum on top of the indium film. Such sandwich films permit the indium to make ohmic contact to the CdS, while the aluminum films permit the long surface conduction route.

The z-cut LiNbO₃ crystal was subject to x-ray analysis. We were able to identify the x and y axes of the wafer by comparing our pictures to published data [21]. The wafer was cut in half along a line 13.5° from the true x-axis. This cut became the "x-axis" referred to as our "y-axis."

A very selective low-pass filter had to be inserted directly at the contact terminal port, rather than at the detector output. Such a filter, with 60 dB

S. T. Kowel

separation between 30 MHz and the desired signals (between zero and 4 MHz), was required to eliminate feed-through.

With these improvements, we were able to detect the long hoped-for difference frequency signal which was image dependent, and disappeared in the dark. The device was operated with the bias current electronically maintained at a constant level of 0.25 mA. The sensor, with a resistance of 1K Ω , acted like a current source since it was terminated in 15 Ω .

The experiments performed were meant to give convincing proof that the strong acoustically induced modulation of the photoconductivity (up to 20%) did produce the pseudo beam steering effect required for two-dimensional transform imaging. This required us to show that as the image is physically rotated, the device can electronically track the image spatial frequency components angle for angle.

We also were able to make phase measurements verifying that the sensor satisfies the Fourier translation theorem along any arbitrary axis.

The evaluation of a device with apodized transducers revealed numerous anomalies related to non-uniform acoustic fields. These non-uniformities are caused by the large variation in acoustic aperture size and position due to the "sinc x" form of the finger overlap. This apodization creates a non-uniform wavefront and also produces highly diffracting waves from the smaller overlaps.

Thus we abandoned this form of transducer. For simplicity, we went to a simple six finger pair, uniformly spaced, unapodized design. This yields approximately equal bandwidth but with more roundoff at the band edges.

With this sensor, we were able to track a spacial frequency in an image when the object was rotated a full 360°. The signals were clean and smooth. These experiments were performed by raster scanning in frequency space. While one oscillator scanned, the other was kept fixed. An oscilloscope picture was taken, the object rotated; the fixed frequency readjusted. Fig. 2.3 shows the g_x , g_y plane labelled by the temporal frequencies. The marked points correspond to signals obtained by 10° rotations for two objects, one with a spatial frequency magnitude of 3 cm⁻¹ and one with 4 cm⁻¹. Note the 45° diagonal line along which no data is obtained, due, as predicted, to the zero difference frequency cutoff of the detector. Each bar pattern object had a zero frequency plus two fundamental frequency peaks within the transducer bandwidth.

Fig. 2.4 reveals the geometry of the rotation experiments. Fig. 2.5 shows the oscilloscope traces for each rotation. Each trace is obtained by adjustment of the fixed frequency to recapture one of the two non-zero spatial frequencies after each 10° rotation. Rotation through 180° revealed all of the points in Fig. 2.5, since there are two non-zero peaks, and therefore two non-zero spacial frequencies, for each new orientation. An additional 180° was plotted to confirm the reproducibility of the data.

Starting along the g_x axis ($g_y = 0$), we first see all three peaks in Fig. 2.5. As the rotation begins, we follow one non-zero frequency peak around the g_x , g_y space by varying the generator controlling g_y . At $\theta = 90^\circ$, this peak has moved into the center of the trace. But it is not the zero-frequency peak as we additionally confirmed by removing the object and noting the disappearance of the peak.

These experiments would be much easier if we could make circular scans in g_x , g_y space, but our present electronic equipment only permitted raster scanning and so the three peaks were always on three separate scans at three separate values of g_y , except when $g_y = 0$. Here the three image frequencies are along the scanned direction. Future experiments will include circular scanning electronics.

It was also quite satisfying to continuously vary the image spatial frequency magnitude. With $g_y = 0$, the two non-zero frequency peaks move smoothly in toward the zero frequency peak as the image frequency is decreased.

These results are strong evidence for the pseudo beam steering effect. Indeed, the very fact of obtaining these signals at all is strong evidence since the existence of signals depends on the vector addition of the wavevectors in order for the image transform space and the acoustic space to be superimposed.

To perform phase measurements, the configuration used needs to be modified.[13,14] Since the difference frequency is generated in the CdS film, there is no reference against which the signal phase can be measured. Therefore, a reference must be created electronically by mixing signals from the same generators that drive the transducers. Specifically, we want to determine if the device operates consistently with the Fourier translation theorem. We want to measure the change of phase of a given spatial frequency component as a function of image displacement. These measurements were made successfully for the glass substrate sensors using the linear change of photoconductivity with strain and formed the basis for the motion-detection application. [6].

Quantitative measurements resulting from our set-up revealed the linear variation of phase with frequency for a stationary bar pattern. The phase was linear in the region of the peak, and deteriorated off the peak since there is really no signal being detected. As the image was displaced in any direction, the straight line sweeps across the peak region, while the amplitude peak remained stationary, save for some minor changes in detail.

We expect a linear change in phase,

$$\phi = -2\pi \vec{g} \cdot \vec{r}_0 \quad (2.3)$$

for a displacement of the image \vec{r}_0 . This implies that in order to tell the direction and distance involved in the displacement, two measurements of ϕ must be made, although only one spatial frequency is needed.

After adjusting the image so that its fundamental spatial frequency vector \vec{g}_1 is along a particular direction, measured by protractor from the object itself, we translated the image, using precision micrometer translation stages, in the x-direction and the y-direction until we had measured some specific phase change. From (2.3)

$$\phi_x = 2\pi |\vec{g}_1| \Delta x \cos \theta \quad (2.4)$$

for motion along the x-axis, Δx , where θ is the smallest angle between \vec{g}_1 and the x-axis.

Similarly for translation along the y-axis,

$$\phi_y = -2\pi |\vec{g}_1| \Delta y \sin \theta \quad (2.5)$$

As one additional check, suppose that we choose $\phi_x = \phi_y$, then

$$\frac{\Delta y}{\Delta x} = \cotan \theta, \quad (2.6)$$

Table 1 shows data for this case, $\phi_x = \phi_y = 2\pi$. The results from (2.4), (2.5), and (2.6) yield the correct orientation for the pattern to within 10%. This is a very strong quantitative test of pseudo beam steering, and therefore, of Fourier imaging.

Δy	Δx	θ	θ	θ	θ
measured	measured	(2.4.)	(2.5.)	(2.6.)	measured
.0659"	.0751"	45.8°	51.6°	49°	47°

TABLE 1. Quantitative measurement of angle from phase.

S. T. Kowel

Here

$$|g_1| = 833.3 \text{ m}^{-1}, \text{ a period of } 1.2 \text{ mm}.$$

III. Conclusions

We have successfully fabricated a monolithic, two-dimensional acoustooptical processor, yielding real-time Fourier transform frequency, magnitude, and phase data. The magnitude of the acoustically-induced modulation is so large that convolvers and correlators may be fashioned using CdS on LiNbO₃, using either a one- or two-dimensional geometry. Without the use of pseudo-beam steering it would be necessary to provide many transducers in order to produce two-dimensional acoustic coverage on a line-by-line basis. Such an approach is likely to be complicated by diffraction problems if a large number of small aperture transducers are employed.

The fact that the effect is so profound (20% modulation of the photoconductivity), coupled with our success in making stable, highly photoconductive films of CdS on z-cut LiNbO₃, implies that we can concentrate our efforts on improvements. Improvement in transducer design is a high priority aimed at developing a still more uniform, collimated wavefront, and a larger bandwidth.

By introducing further spacings between transducers and the CdS film contact region, we hope to operate devices in the gated mode, making possible spatial raster scanning sensors in addition to Fourier imaging sensors.

Acknowledgements

The authors wish to thank Mr. David Helm of the U.S. Army Night Vision Laboratory and Mr. Joseph Hannigan of the U.S. Army Engineer Topographic Laboratory for their interest in this work. The work report here was supported by the U.S. Army Night Vision Laboratory, Fort Belvoir, VA.

Bibliography

1. P. G. Kornreich, S. T. Kowel, D. J. Fleming, N. T. Yang, A. Gupta, and O. Lewis, "DEFT: Direct Electronic Fourier Transforms of Optical Images," IEEE Proceedings, Vol. 62, pp. 1072-1087, August, 1974.
2. P. G. Kornreich, S. T. Kowel, "Direct Electronics Fourier Transforms of Images," U.S. Patent #3,836,712 (9/17/74).
3. S. T. Kowel, P. G. Kornreich, O. Lewis, A. Gupta, N. T. Yang, and R. Zawada, "DEFT: Progress on Direct Electronic Fourier Transform of Two-Dimensional Images," RADC-TR-244, September 1974.
4. S. T. Kowel, P. G. Kornreich, O. Lewis, A. Gupta, and R. Zawada, "Progress on Two-Dimensional Direct Electronic Fourier Transform (DEFT) Devices," 1974 Ultrasonics Symposium Proceedings, pp. 763-767.
5. P. Kornreich, N. T. Yang, and S. T. Kowel, "A Direct Electronic Fourier Transform Device for Imaging," IEEE Proc. Letters, Vol. 61, August 1973.
6. S. T. Kowel, P. G. Kornreich, O. Lewis, and F. D. Kirschner, "Passive Detection of Motion Transverse to the Optical Viewing Axis," IEEE Trans. on Instrumentation and Measurement, Vol. IM-24, pp. 248-255, Sept. 1975.
7. S. T. Kowel, P. G. Kornreich, and O. Lewis, "Focus Detection Using Direct Electronic Fourier Transform Sensors," J. of Appl. Photographic Engineering, Vol. 2, #3, pp. 113-118, Summer 1976.
8. S. T. Kowel, P. G. Kornreich, A. Mahapatra, D. Cleverly, B. Emmer, and R. Zawada, "Two-Dimensional Fourier Imaging of Light Using Acoustic Pseudo-Beam Steering," 1975 Ultrasonics Symposium Proceedings, pp. 136-140.
9. S. T. Kowel, P. G. Kornreich, A. Mahapatra, and B. Emmer, "Experimental Confirmation of Two-Dimensional Acoustic Processing of Images," 1976 Ultrasonics Symposium Proceedings, pp. 668-672, Oct. 1976.
10. H. Gautier, G. S. Kino, and H. J. Shaw, "Acoustic Transform Techniques Applied to Optical Imaging," 1974 Ultrasonics Symposium Proceedings, pp. 99-103.
11. M. Luukkala, P. Merilainen, and K. Saarinen, "Acousto-Resistive Effects in Thin Film CdSe/LiNbO₃ Delay Line System," 1974 Ultrasonics Symposium Proceedings, pp. 345-348.
12. V. L. Newhouse, C. L. Chen, and K. L. Davis, "Possibility of Switching and Steering Surface Waves by Nonlinear Mixing in Anisotropic Media," J. Appl. Phys., Vol. 43, pp. 2603-2608, June 1972.
13. S. T. Kowel, P. G. Kornreich, K. W. Loh, A. Mahapatra, M. Mehter, P. Reck, and B. Emmer, "Imaging without Raster Scanning," to be published in IEEE Trans. on Electron Devices.
14. S. T. Kowel, P. G. Kornreich, K. W. Loh, A. Mahapatra, M. Mehter, B. Emmer, P. Reck, and W. A. Penn, "Two-Dimensional Direct Electronic Fourier Transform Devices (DEFT): Analysis, Fabrication, and Evaluation," TR-77-5, Department of Electrical Engineering, Syracuse University, Syracuse, NY 13210.
15. P. G. Kornreich, A. Mahapatra, S. T. Kowel, K. W. Loh, and Bruce Emmer, "Double-Layered Polycrystalline Cadmium Sulphide on Lithium Niobate," to be published in the J. of Applied Physics.
16. J. F. Nye, Physical Properties of Crystals, Oxford, 1969.
17. M. Luukkala, private communication.
18. L. P. Solie, "A New Mode of Operation for the Surface-Wave Convolver," Proc. IEEE, Vol. 64, May 1976, pp. 760-763.
19. L. P. Solie, "Integrated Surface Acoustic Wave Convolver/Amplifier," RADC-TR-75-191, 11/75.
20. H. I. Smith, F. J. Bachmer, and N. Efremow, "A High Yield Photolithographic Technique for Surface Wave Devices," J. of the Electrochemical Society, Vol. 118, pp. 821-825, May 1971.
21. A. J. Slobodnik, Jr., E. D. Conway, and R. T. Delmonico, Microwave Acoustics Handbook, Air Force Cambridge Research Laboratories, 1973.

S. T. Kovel

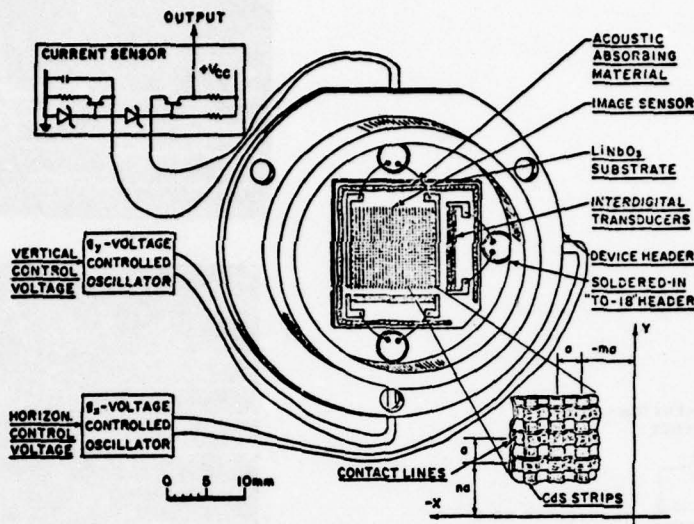


Fig. 2.1 Electrophotoconductive Sensor.

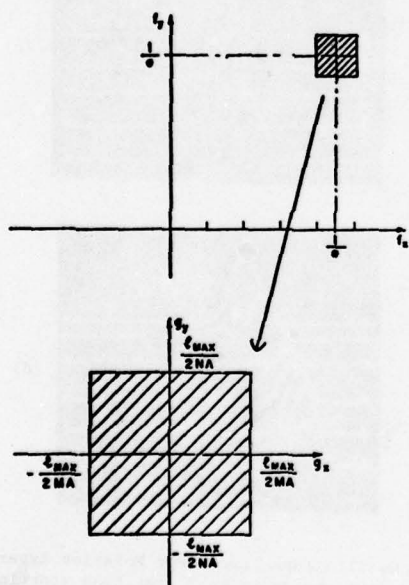


Fig. 2.2 Schematic representation of the original Fourier space (g_x, g_y). The value of g_{\max}^2 is the number of Fourier components available in the reduced space.

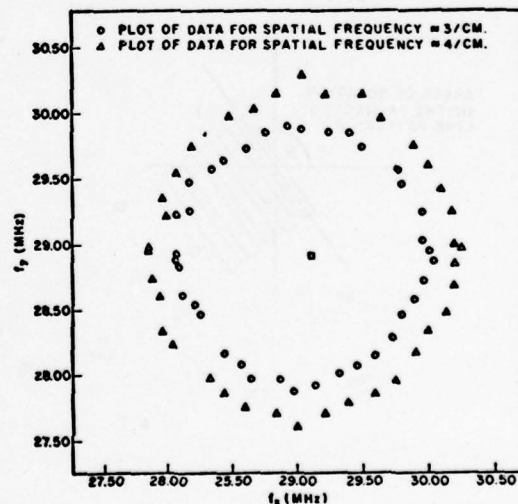


Fig. 2.3 Time Frequency Coordinates of the Vector Spatial Frequencies. As the object was rotated (Fig. 2.4), the frequencies were mapped through 180° of rotation. Note the "dead space" along the 45° diagonal caused by the inability of the detector circuitry to pass a zero difference frequency. The square point in the center represents the zero spatial frequency peak which moved very little during the rotation experiments.

S. T. Kowel

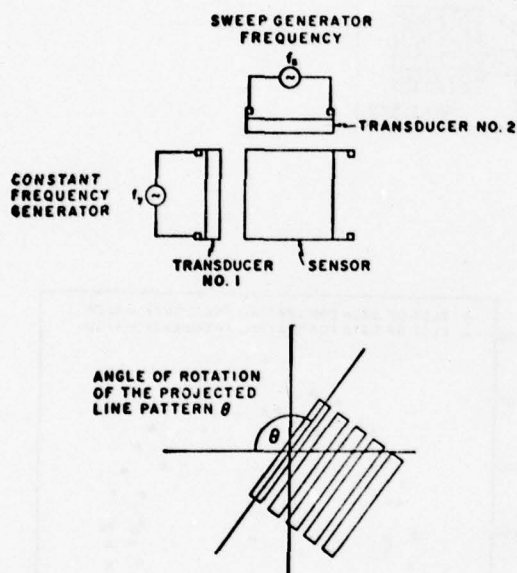


Fig. 2.4 Geometry of Pseudo Beam Steering Experiments. A bar pattern was projected on the sensor and rotated manually. The zero spatial frequency and the two fundamental spatial frequencies were found by changing the generator frequency f_y for each 10° rotation of the object.

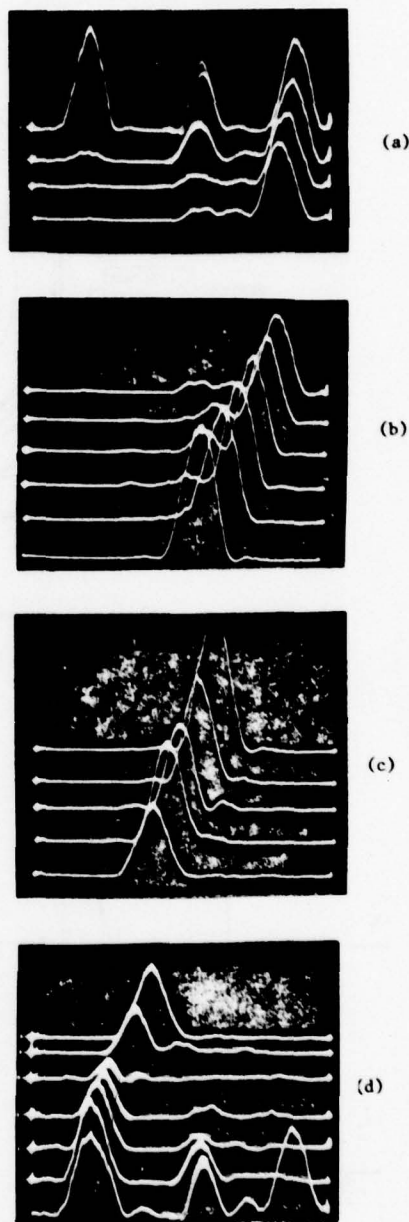


Fig. 2.5 Oscilloscope Traces For Rotation Experiments. Each trace corresponds to a 10° rotation starting with $g_y = 0$. The bottom trace in each picture is repeated as the top trace in the succeeding picture. Thus 90° corresponds to the second trace from the top in (c), 180° to the bottom trace in (d). At 90° , the right hand peak has moved to the center of the trace, just where the zero frequency peak would appear for $g_y = 0$. Note the slight difference between 0° and 180° , presumably caused by translations which change the picture slightly.

APPENDIX II.

DOUBLE-LAYERED POLYCRYSTALLINE CADMIUM SULFIDE
ON LITHIUM NIOBATE

J. Appl. Phys. 49(4), April 1978

Double-layered polycrystalline cadmium sulfide on lithium niobate^{a)}

Philipp G. Kornreich, Amaresh Mahapatra, Stephen T. Kowel, K. W. Loh, and Bruce Emmer

Department of Electrical and Computer Engineering, 111 Link Hall, Syracuse University, Syracuse, New York 13210

(Received 16 September 1977; accepted for publication 29 November 1977)

We have developed a technique for fabricating polycrystalline thin films of CdS on z-cut LiNbO₃. A single film will show a light-to-dark-conductivity ratio of approximately unity with very high sheet resistance after curing. To make a good photoconductor, a second film is then deposited. This film is protected during the subsequent curing from out-diffusion from the LiNbO₃ by the first film and develops a light-to-dark-conductivity ratio of 10000 in room light with a sheet conductivity of 10^{-10} s/□mcd. Films produced by this layered process also possess a remarkably large conductivity-modulation dependence (20%) on the square of an impressed electric field provided by a traveling surface acoustic wave in the LiNbO₃ substrate.

PACS numbers: 73.60.Fw, 81.15.Ef, 72.50.+b, 43.35.Qv

I. INTRODUCTION

A major area of research in the field of surface acoustic waves (SAW) involves the interaction of ultrasonic Rayleigh waves with conduction electrons. Such interactions provide the physical basis of image scanners, Fourier-transform imagers, convolvers, and microwave traveling-wave amplifiers.¹⁻¹⁰ CdS is a good candidate for such applications since it is inexpensive and can be fabricated with a wide range of both optically induced and dark conductivities.

We have been interested in both the effects of strain and electric fields on the photoconductivity. We first made direct electronic Fourier-transform (DEFT) devices by vacuum depositing CdS films on glass.^{11,1} The films were cured by using a variation of the method developed by Boer.¹² This was done in a diffusion furnace in an atmosphere of CdS, O₂, HCl, and Cu.

A piezoelectric transducer was subsequently bonded to the substrate. The transducer excited traveling surface acoustic waves in the glass which modulated the carriers generated in the film by an image. These charges are detected as a current by indium contacts. Such devices depend on the linear strain-induced modulation of the photoconductivity, which we observed to be approximately 0.1% of the photoconductivity in room light.

More recently, we have been fabricating films on z-cut LiNbO₃. This structure makes use of metal interdigital contacts deposited on the piezoelectric substrate for the generation of the Rayleigh waves. By using two orthogonally directed transducers, we are able to produce signals in the CdS proportional to the two-dimensional Fourier transform of an image intensity.^{13,14} These effects depend on a modulation of photoconductivity proportional to the square of the electric field accompanying the SAW's in the LiNbO₃. This effect is remarkably large, 20% in typical bright-room illumination.

The purpose of this paper is to describe a novel layered technique for fabricating thin films which was developed for deposition on LiNbO₃ and to describe the film properties. We note the variance of our results with the usual boundary theory¹⁵ of photoconductivity.

We expect that the fabrication techniques and modulation effects may be of interest to researchers working with similar films and substrates both for SAW applications, as well as for more fundamental material studies.

II. LAYERED CdS FILM DEPOSITION AND CURING

On the glass substrates, CdS was evaporated from a fused-quartz bottle onto suitably positioned substrates in a vacuum of 10^{-6} Torr. These evaporated films had very high conductivity but a poor light-to-dark-conductivity ratio. To increase their sensitivity they were cured in the vicinity of CdS and Cu powder at 650°C under a N₂ flow, which had traces of O₂ and HCl to optimize the photoconducting properties of the films. The exact ratio of the constituent gases is given in the Appendix. This technique is a variation on the work of Boer.¹² We finally succeeded in obtaining light-to-dark-conductivity ratios of about 5×10^3 at an illumination of 250 mcd of white light. At the same time, the conductivity of the films was quite high, about 0.1 ns/□mcd.

We hoped that by suitably adjusting the doping levels of O₂, HCl, and Cu, one could get good photoconducting films of CdS on LiNbO₃. However, after numerous attempts, we came to the conclusion that this is not possible due to the degrading effects of material diffusing out of the LiNbO₃ during curing.

Next, we decided to overcome the problem of the substrate entirely by laying down a thin layer of SiO₂ between the substrate and the CdS film. This layer would insulate the CdS from the LiNbO₃. At the same time, SiO₂, being stable thermally, would not itself diffuse into the CdS. This idea proved successful in that we improved the L/D ratio by a factor of 100 in our first attempts.

^{a)} The work reported here was supported by the US Army Night Vision Laboratory, Ft. Belvoir, Va. 22060. It contains some of the results of the dissertation of A. Mahapatra.

Unfortunately, the SiO_2 layer had its own problems. It worked fairly well with yz -cut LiNbO_3 , which has a low coefficient of thermal expansion like the SiO_2 . But on z -cut LiNbO_3 , which has a coefficient of thermal expansion 10 times that of yz cut, the films peeled off during curing.

At this point, a number of attempts to prevent the CdS from peeling from the SiO_2 were made, such as graduating the SiO_2 -CdS boundary during evaporation and roughening the surface of the LiNbO_3 . All of these were unsuccessful. We also tried to out-diffuse the LiNbO_3 before evaporation. This would obviate the need for the SiO_2 film. This was also unsuccessful. The films were still degraded during curing.

We next tried Al_2O_3 as an intermediary diffusion barrier. Unfortunately, the CdS film peeled off the Al_2O_3 as it did from SiO_2 . Attempts to prevent peeling by making thicker films of SiO_2 to allow for different expansion rates on the opposite sides were also unsuccessful.

Eventually, we struck upon an ideal solution. We knew that CdS itself would stick to LiNbO_3 . Therefore, why not insulate the photoconducting CdS film from the LiNbO_3 by a second CdS film. If this film were thick enough it would not permit out-diffused elements from LiNbO_3 to reach the second film of CdS. Moreover, there would be no sticking problem at either surface. Our very first experiment with this technique yielded very good L/D ratios. It soon became clear that one could easily adjust the doping levels of HCl, O_2 , and Cu for the second CdS film to have L/D ratios of 10^4 at 500 mcd of white-light illumination. Since then, we have made a number of CdS films on LiNbO_3 by this "double-deposition" or layered technique.

The Appendix reveals an abbreviated "recipe" for evaporating and curing the films.¹³ The best films to date have been approximately 1 μm thick.

It should be noted that these films represent the first reliable photoconductive films on z -cut LiNbO_3 . Luukkala⁸ has made CdSe films on yz -cut LiNbO_3 , but has reported great difficulty in reproducing these films because of the cracking and peeling of the layer of SiO_2 used as a diffusion barrier. Solie has made photoconducting films on yz -cut LiNbO_3 , thus producing an excellent one-dimensional convolver.¹⁰ It is not clear, however, precisely what is the film composition. It is described as CdSe cured with a layer of CdS. The CdS may be a dopant or may indeed represent a "double-layered" film.¹⁶

III. PHENOMENOLOGICAL CALCULATION OF THE CONDUCTANCE OF CdS

Before describing our experimental results, it may be useful to give a brief discussion to reveal the phenomenological nature of the modulation effects. This exercise is useful because it shows the tensor nature of the higher-order interactions. This view has been neglected in the device-oriented papers.^{7,8,10}

Though we realize that various electric field and strain effects may vary through the thickness of the CdS film, we shall, for simplicity, assume all effects to be uniform over the thickness of the CdS film. Thus, the conductance per square can be expanded in a Taylor series to first order in the light intensity $I(x, y)$ and the strain tensor $\sum_{\mu\nu}$, and to second order in the electric field E_μ due to the SAW in the piezoelectric LiNbO_3 substrate.

$$\begin{aligned} \sigma_{\alpha\beta}(x, y) = & \sigma_{\alpha\beta}^D + \sigma_{\alpha\beta\mu\nu}^{DS} \sum_{\mu\nu} + \sigma_{\alpha\beta}^L I(x, y) + \sigma_{\alpha\beta\mu\nu}^{LS} I(x, y) \sum_{\mu\nu} \\ & + \sigma_{\alpha\beta\mu}^{DF} E_\mu + \sigma_{\alpha\beta\mu\nu}^{LF} I(x, y) E_\mu + \sigma_{\alpha\beta\mu\nu}^{DE} E_\mu E_\nu \\ & + \sigma_{\alpha\beta\mu\nu}^{LE} I(x, y) E_\mu E_\nu \dots, \end{aligned} \quad (1)$$

where summation over like Greek indices is implied. Here,

$\sigma_{\alpha\beta}^D$ is the dark conductance per square, $\sigma_{\alpha\beta\mu\nu}^{DS}$ is the change of the dark conductance per square with strain $\sum_{\mu\nu}$, $\sigma_{\alpha\beta}^L$ is the change of the conductance per square with light flux $I(x, y)$, the ordinary photoconductivity, $\sigma_{\alpha\beta\mu\nu}^{LS}$ is the change of the conductance per square with light and strain, $\sigma_{\alpha\beta\mu}^{DF}$ is the linear change of the conductance per square with electric field, $\sigma_{\alpha\beta\mu\nu}^{LF}$ is the linear change of the conductance per square with light and electric field, $\sigma_{\alpha\beta\mu\nu}^{DE}$ is the change of the conductance per square to second order with electric field, and $\sigma_{\alpha\beta\mu\nu}^{LE}$ is the change of the conductance per square to first order in the light intensity and second order in the electric field.

Our polycrystalline CdS films have essentially isotropic symmetry. Therefore all third rank tensors must be zero. This requires that $\sigma_{\alpha\beta\mu}^{DF}$ and $\sigma_{\alpha\beta\mu\nu}^{LF}$ be zero. This also requires that the ordinary photoconductivity be essentially a scalar, $\sigma_L \delta_{\alpha\beta}$. The dark conductance is small compared to the photoconductivity at reasonable light levels for good photoconductive CdS. This allows us to neglect the terms $\sigma_{\alpha\beta}^D$, $\sigma_{\alpha\beta\mu\nu}^{DS}$, and $\sigma_{\alpha\beta\mu\nu}^{DE}$. This reduces Eq. (1) to

$$\begin{aligned} \sigma_{\alpha\beta} = & \sigma_L \delta_{\alpha\beta} I(x, y) + \sigma_{\alpha\beta\mu\nu}^{LS} I(x, y) \sum_{\mu\nu} \\ & + \sigma_{\alpha\beta\mu\nu}^{LE} I(x, y) E_\mu E_\nu. \end{aligned} \quad (2)$$

The term $\sigma_{\alpha\beta\mu\nu}^{LS}$ is the one that has been used in all our previous DEFT devices. However, here we are interested in the change of the conductivity to first order with light intensity and to second order with electric field, the last term in Eq. (2).

A similar effect has previously been observed by Luukkala *et al.*⁸ Solie¹⁰ has fabricated a convolver using a CdS/CdSe film system, and has observed difference frequencies using 132- and 123-MHz carriers. They observed a substantial change of the photoconductivity of a CdSe film deposited on a LiNbO_3 substrate when a SAW was propagated on its surface. They observed the effect with 70-MHz SAW's. There is substantial evidence that the effect is to second order in the electric field. They observed a change in the dc photoconductivity, as well as observing an output at twice the SAW frequency; and the effect disappeared when the experiment was conducted on a nonpiezoelectric fused-quartz substrate.

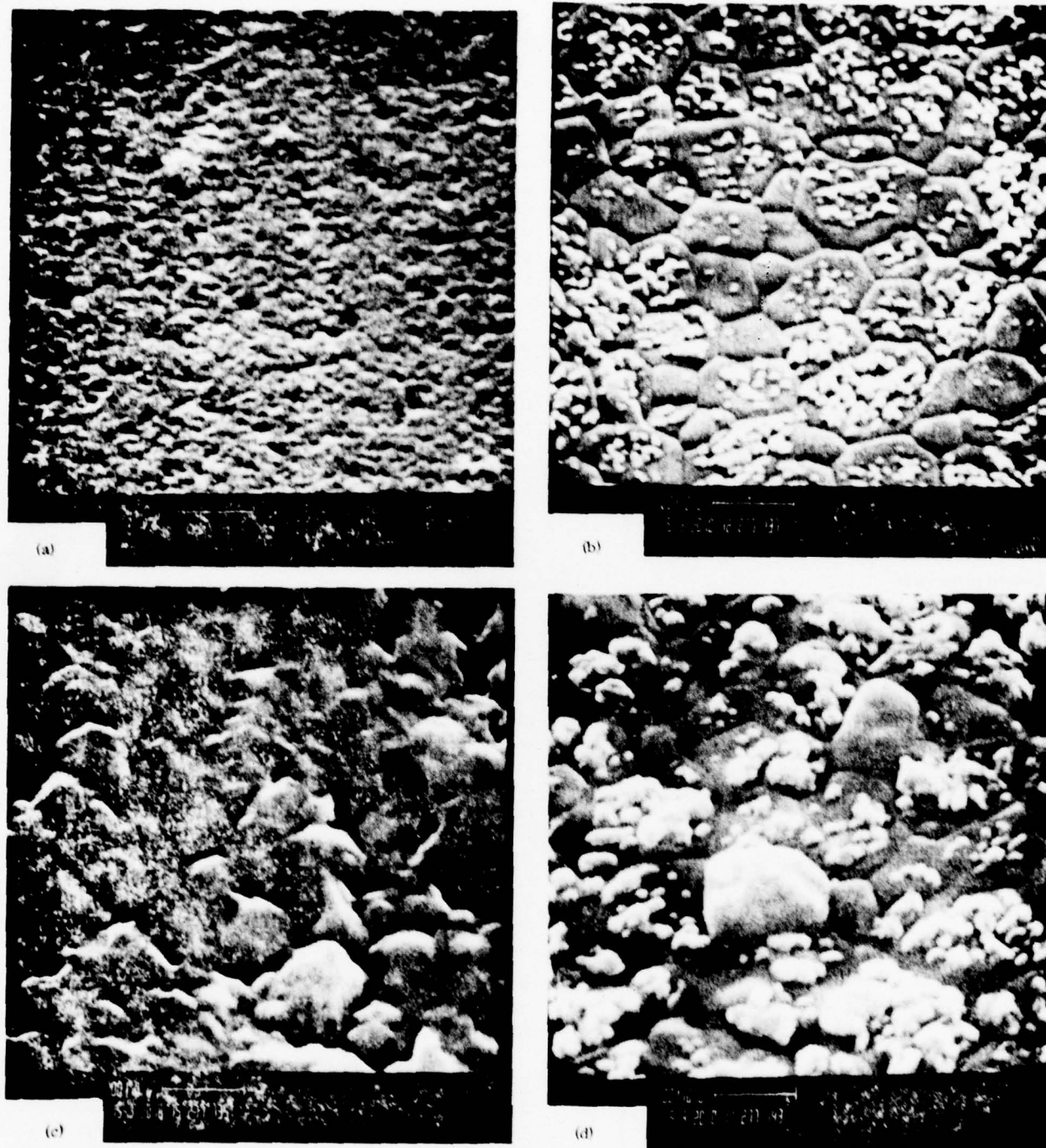


FIG. 1. Scanning-electron-microscope studies of the films at various steps. Note the 1- μ m scale indicated just under the figures. (a) First deposition; (b) first curing; (c) second deposition; (d) second curing.

The effect, also known as the Franz-Keldysh effect, has been observed in CdS by Franz¹⁷ and Keldysh,¹⁸ as well as by Kohn and Lampert.¹⁹ They also reported the effect to be quite large.

IV. MEASUREMENTS OF CdS FILM PROPERTIES

Once the CdS films have been laid down and cured,

it is of considerable interest to study a number of parameters that can be correlated with known and predicted properties. These include surface uniformity, absorption of light as a function of optical wavelength, conductivity change as a function of light level, change of conductivity with strain, and change of conductivity with temperature. In Sec. IV we describe a number of such measurements and correlate the results, whenever possible, with our expectations.

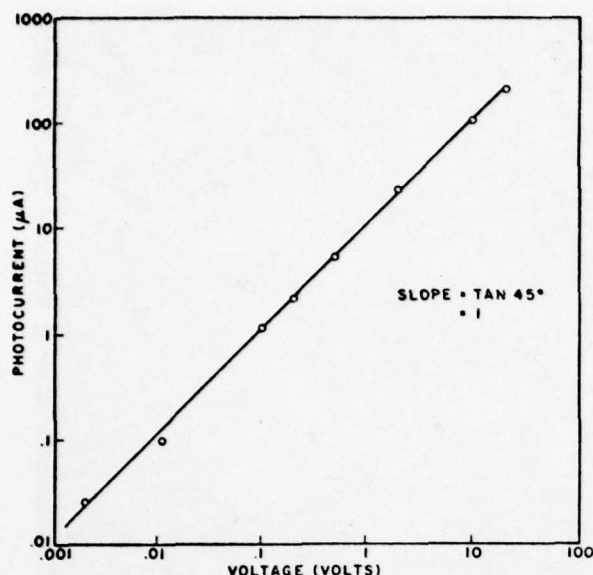


FIG. 2. Voltage versus current for uniform illumination.

A. Surface properties

The films were examined under an electron microscope at various stages of fabrication as shown in Fig. 1. The surface of the bottom film is smooth with no obvious structure. On a $1\text{-}\mu\text{m}$ scale it looks something like rough concrete. Once cured, a definite crystallization becomes evident. The film looks like a tile floor

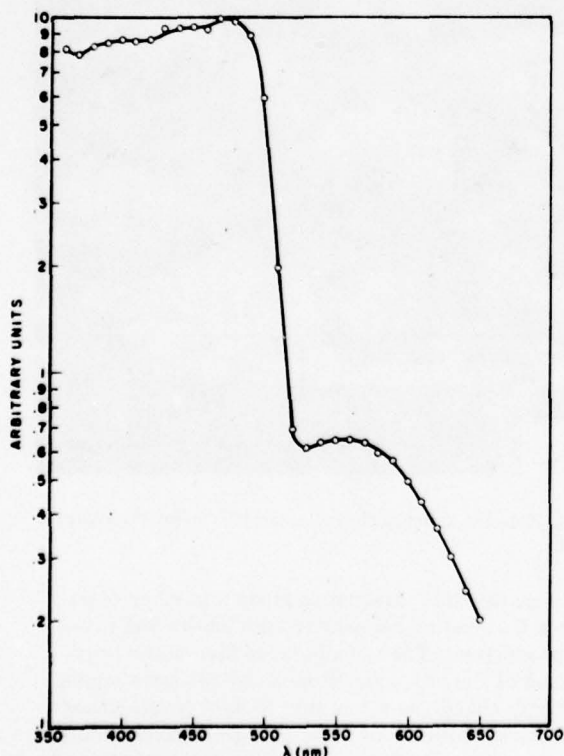


FIG. 3. Variation of photocurrent with light wavelength at room temperature.

with irregularly shaped but smoothly fitting tiles. On top of the film is what appears to be excess CdS dust. The crystallites have between four and six sides and are $\frac{1}{2}$ – $1\text{ }\mu$ in diameter.

With the second layer deposited, the surface looks very hilly and irregular. But after curing, we are again left with a smooth film with clear crystallite boundaries, although not as smooth as the bottom film. Figure 1(d) shows the surface of this final film. Note that again there is dust sprinkled on top of the film. We are giving some thought to see whether this curing artifact can be prevented or removed. It is quite significant that there are no holes or tears in the film.

B. Film conductivity

We have measured the i - V characteristics of CdS films on LiNbO_3 by depositing indium/aluminum contacts. The voltage was varied over 4 decades and the i - V curve was found to be strikingly linear, as shown in Fig. 2. The contact separation was about $75\text{ }\mu\text{m}$. Assuming the crystallites to be $1\text{ }\mu\text{m}$ wide, there were 75 crystallites between any pair of contacts. Let us assume that the barrier model of conductivity holds for our films, so that we can assume the current to be of the form

$$i = I_0 [\exp(-\phi/kT)] [\exp(qV_d/kT) - 1], \quad (3)$$

where ϕ is the barrier voltage between crystallites and V_d is the voltage across each barrier.¹⁵ Now if $qV_d \leq kT$, the above expression can be suitably expanded to give a linear i - V characteristic. However, at the highest applied voltage we used (20 V), V_d is about $20/75 \approx 0.267\text{ V}$. Thus, qV_d is about $10\text{ }kT$ and one would expect highly nonlinear i - V curves. Since this does not happen, we think that either the barrier model quoted in many papers does not apply to our films, or else Eq. (3) is an oversimplification. We obtained a linear curve for current versus voltage from $V = 0.002$ to 20 V , i.e., over 4 decades. The drift-electric field changes from $E = 0.2$ to $2 \times 10^3\text{ V/cm}$.

In order to make the electrical contacts on the CdS, we first deposit indium and then aluminum. The indium makes Ohmic contact to the CdS, and the aluminum provides high conductivity along the contacts.

We next measured the variation of photocurrent with light wavelength. The normalized curve given in Fig. 3 shows the band edge to be at 505 nm , which corresponds to a band gap of 2.46 eV . The photocurrent drops sharply at higher wavelengths. However, there is a secondary maximum at 560 nm , which corresponds to a level 0.25 eV from the valence band. A similar level was detected in our CdS films on glass. We believe this to be a sensitizing center with low-capture cross section for electrons. These measurements were made using a calibrated E.G. and G. high sensitivity spectroradiometer.

The next measurement was the variation of photocurrent with white-light intensity, showing clearly the power-law behavior of the conductivity. There is a supralinear variation with an exponent 1.4 as can be seen in Fig. 4. However, our films on glass had an

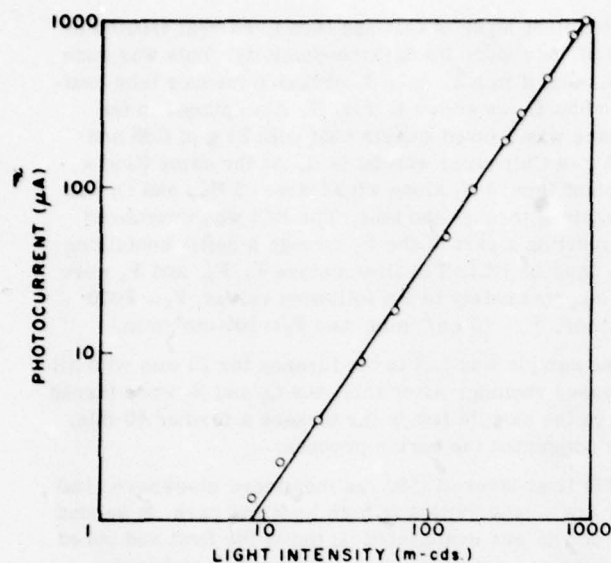


FIG. 4. Photocurrent versus light intensity. This particular sample gave $i \propto I^1 A$.

exponent lying between 0.8 and 1, probably due to the sensitizing center lying closer to the valence band (0.15 eV). We also measured the rise and decay times of the photocurrent for different white-light intensities from 4 to 1000 mcd. The rise, as expected, is an order of magnitude larger than the decay time. The decay time changes from 28 ms at low intensities to 3 ms at 1000 mcd.

Of particular significance to our goal of fabricating Fourier imaging sensors and signal convolvers, was the evaluation of the last term in Eq. (1). Figure 5 shows a schematic view of structure used to make conductivity-modulation experiments. For the purposes of this paper, two adjacent transducers propagated Rayleigh waves in the x direction across the CdS film region. The contact pattern detected the difference frequency current due to this term in the conductivity. It

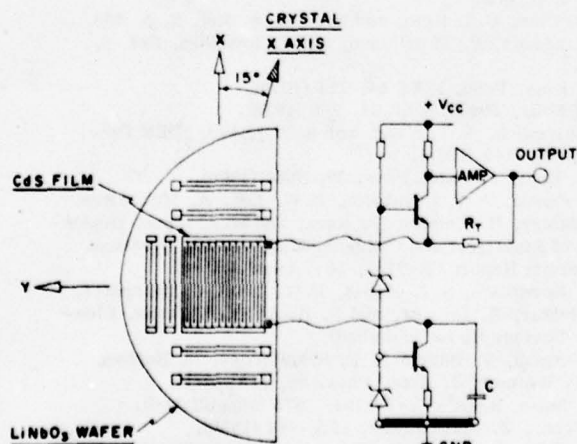


FIG. 5. Deft imaging sensor. The measurements in this paper were made using two contiguous transducers propagating in the x direction.

can be shown^{13,14} that this signal, $i(t)$, is proportional to the integral over x of the product of the square of the electric field associated with the surface acoustic wave with the optical intensity. With sinusoidal acoustic waves,

$$i(t) = (2i_{dc}/\sigma_d) \langle \bar{I}_i(f_s) \rangle [E_{1x}E_{2x}(\sigma_{13}^{LE} + \sigma_{66}^{LE}) + E_{1x}E_{2x}(\sigma_{12}^{LE} + \sigma_{44}^{LE})], \quad (4)$$

where $\langle \bar{I}_i(f_s) \rangle$ is the smoothed normalized Fourier transform of the image intensity, i_{dc} is the dc current, σ_d is the dark conductivity, and E_{1x} , E_{1y} , E_{2x} , and E_{2y} are the amplitudes of the SAW electric fields generated by transducers 1 and 2 respectively. The coefficients σ_{13}^{LE} , σ_{66}^{LE} , σ_{12}^{LE} , and σ_{44}^{LE} are defined in terms of the coefficients $\sigma_{\alpha\beta\gamma\delta}^{LE}$ by the usual elasticity notation.²⁰ Using a light pattern with a well-defined spatial frequency, we measured $i(t)/i_{dc}$ as a function of $(P_1P_2)^{1/2}$, where P_1 and P_2 are the acoustic powers generated by transducers 1 and 2, which is proportional to $E_{1x}E_{2x}$ and $E_{1y}E_{2y}$, to obtain the curve of Fig. 6. As can be readily seen, a modulation of more than 10% was obtained and a larger modulation is within reach. Saturation is seen to set in at these acoustic-power levels since the SAW fields begin to create appreciable modulation of the dc current. At lower levels, the curve is quite linear. Actually, σ_d is an increasing function of acoustic power also.^{13,14}

This SAW modulation of the photocurrent is an enormous second-order effect; especially so when considering that the linear effect in strain ($\sigma_{\alpha\beta\gamma\delta}^{LS} \sum_{\alpha\beta\gamma\delta}$) is approximately 200 times smaller.

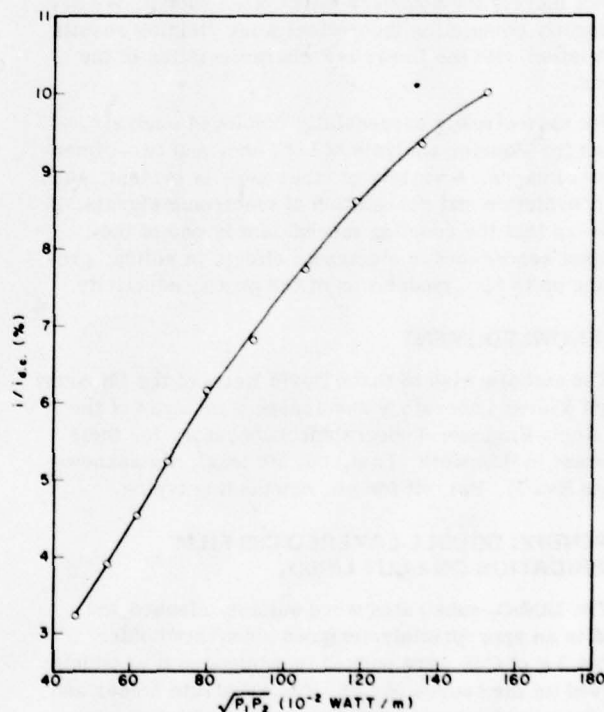


FIG. 6. Large modulation of the photoconductivity as a function of the acoustic power. Saturation due to modulation of the dark current is evident for acoustic signals $80 < (P_1P_2)^{1/2} < 250$ in units of 10^{-2} W/M of transducer aperture.

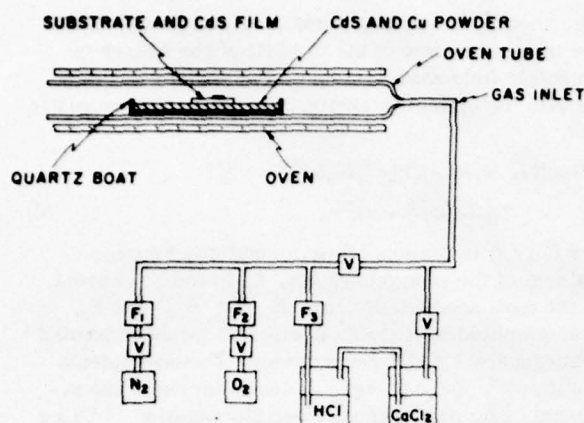


FIG. 7. Curing arrangement in the diffusion furnace. V represents valves and F represents flow meters.

V. CONCLUSIONS

We have described a method of fabricating a polycrystalline film of CdS on *z*-cut LiNbO₃, which results in high light-to-dark-conductivity ratios and large modulation proportional to the electric field squared. The fabrication technique employs a double-layered deposition and recrystallization procedure in order to obtain a film not destroyed by diffusion from the LiNbO₃ during heat treatment.

Evidence indicates that the conduction mechanism is not merely the boundary effect often quoted. We are presently completing theoretical work yielding results consistent with the linear *i*-*V* characteristics of the films.

We have already successfully employed such structures for Fourier analysis of both one- and two-dimensional images. A variety of other uses is evident, such as convolution and correlation of electronic signals. It appears that the coupling mechanism is one of the largest second-order electronic effects in solids, providing up to 20% modulation of the photoconductivity.

ACKNOWLEDGMENT

The authors wish to thank David Helm of the US Army Night Vision Laboratory and Joseph Hanningan of the US Army Engineer Topographic Laboratory for their interest in this work. Last, but not least, we acknowledge Eva M. Barrett for her outstanding typing.

APPENDIX: DOUBLE-LAYERED CdS FILM FABRICATION ON *z*-CUT LiNbO₃

The LiNbO₃ substrates were suitably cleaned and held in an appropriately designed substrate holder. About 3 g of CdS were packed in a tungsten boat which served as the source of CdS. The substrate holder and the tungsten boat were appropriately positioned in a vacuum chamber evacuated to 10⁻⁶ Torr. The substrate holder was heated to 210°C. The evaporation was continued until the films reached a thickness of approximately 1 μm.

This first layer of CdS had then to be heat treated or "cured" to reduce its dark conductivity. This was done by placing it in a 2½-in.-i.d. diffusion furnace tube heated to 650°C, as shown in Fig. 7. Also placed in the furnace was a fused-quartz boat with 25 g of CdS and 12.5 g of Cu powder spread in it. At the same time a constant flow of N₂ along with traces of HCl and O₂ was maintained through the tube. The HCl was introduced by diverting a part of the N₂ through a bottle containing 37% aqueous HCl. The flow meters F₁, F₂, and F₃ were set, approximately to the following values: F₁ = 2000 cm³/min, F₂ = 10 cm³/min, and F₃ = 100 cm³/min.

The sample was left in the furnace for 30 min with all the gases running. After this, the O₂ and N₂ were turned off and the sample left in the furnace a further 60 min. This completed the curing process.

This first layer of CdS, as mentioned elsewhere, had very low conductivities in both light and dark. A second film of CdS was evaporated on top of the first and cured using the same procedure for evaporation and curing. This resulted in films with light-to-dark-conductivity ratios as high as 10⁴. To obtain this value, one might have to readjust the HCl flow setting, since the amount of HCl picked up depends on the volume of HCl in the bottle, the bore of the inlet tube, etc. In our experience, it is not necessary to adjust the O₂ or the amount of Cu to get *L/D* ratios of 10³, which is good enough for most applications.

- ¹P. G. Kornreich, S. T. Kowel, D. J. Fleming, N. T. Yang, A. Gupta, and O. Lewis, *Proc. IEEE* **62**, 1072 (1974).
- ²S. T. Kowel, P. G. Kornreich, O. Lewis, A. Gupta, and R. Zawada, 1974 Ultrasonics Symposium Proceedings, 1974, p. 763 (unpublished).
- ³S. T. Kowel, P. G. Kornreich, O. Lewis, and F. D. Kirschner, *IEEE Trans. Instrum. Meas.* **IM-24**, 248 (1975).
- ⁴S. T. Kowel, P. G. Kornreich, and O. Lewis, *J. Appl. Photogr. Eng.* **2**, 113 (1976).
- ⁵S. T. Kowel, P. G. Kornreich, A. Mahapatra, D. Cleverly, B. Emmer, and R. Zawada, 1976 Ultrasonics Symposium Proceedings, 1976, p. 136 (unpublished).
- ⁶S. T. Kowel, P. G. Kornreich, A. Mahapatra, and B. Emmer, *Ref. 5*, p. 668.
- ⁷H. Gautier, G. S. Kino, and H. J. Shaw, *Ref. 2*, p. 668.
- ⁸M. Luukkala, P. Merilainen, and K. Saarinen, *Ref. 2*, p. 345.
- ⁹G. S. Kino, *Proc. IEEE* **64**, 724 (1976).
- ¹⁰L. P. Solie, *Proc. IEEE* **64**, 760 (1976).
- ¹¹P. Kornreich, N. T. Yang, and S. T. Kowel, *IEEE Proc. Lett.* **61**, 1149 (1973).
- ¹²K. W. Boer, *J. Appl. Phys.* **37**, 2664 (1966).
- ¹³S. T. Kowel, P. G. Kornreich, K. W. Loh, A. Mahapatra, M. Mehter, B. Emmer, P. Reck, and W. A. Penn, Department of Electrical and Computer Engineering, Syracuse University Report TR-77-5, 1977 (unpublished).
- ¹⁴P. G. Kornreich, S. T. Kowel, K. W. Loh, A. Mahapatra, M. Mehter, B. Emmer, and P. Reck, *IEEE Trans. Electron. Devices* (to be published).
- ¹⁵A. Waxman, V. Henreich, F. Schellcross, H. Borhan, and P. Weimer, *J. Appl. Phys.* **36**, 168 (1965).
- ¹⁶L. P. Solie, RADC-TR-75-191, 1975 (unpublished).
- ¹⁷W. Franz, *Z. Naturforsch.* **13A**, 484 (1958).
- ¹⁸L. V. Keldysh, *Zh. Eksp. Teor. Fiz.* **34**, 1138 (1958) [*Sov. Phys.-JETP* **4**, 788 (1958)].
- ¹⁹E. S. Kohn and M. Lampert, *Phys. Rev. B* **4**, 4479 (1971).
- ²⁰J. F. Ney, *Physical Properties of Crystals* (Clarendon, Oxford, 1969).

APPENDIX III.

MODULATION OF CURRENT IN A THIN FILM OF LEAD TIN SELENIDE
BY BULK ACOUSTIC WAVES

Appl. Phys. Lett 32(11), 1 June 1978

41

Modulation of current in a thin film of lead tin selenide by bulk acoustic waves

S. T. Kowel, P. G. Kornreich, and T. Szebenyi

Department of Electrical and Computer Engineering, Syracuse University, Syracuse, New York 13210

D. Kaplan

U.S. Army Night Vision and Electro-optics Laboratories, Fort Belvoir, Virginia 22060

(Received 11 January 1978; accepted for publication 28 March 1978)

We have measured a 0.1% modulation of electron current in a lead tin selenide film due to a bulk acoustic wave propagated in the barium fluoride substrate. This effect was observed as an ac component of the current at the acoustic frequency 0.6 MHz.

PACS numbers: 78.20.Hp, 73.60.Fw, 43.35.Ns, 72.50.+b

There has been significant progress in the area of optical imaging using acoustical modulation of photocurrent. Devices for image scanning¹⁻³ and Fourier imaging⁴⁻⁷ in the visible range have been reported. It is of considerable interest to determine whether the principles on which these devices depend can be applied at infrared wavelengths. Our previous work with cadmium sulphide deposited on glass⁴ indicated that a linear change of photocurrent with acoustic strain should be observed in many semiconductors.

Thus the first step in fabricating infrared imagers using acoustic waves is to show a significant modulation. For this purpose it is not necessary to cool the film since we assume that the modulation of room-temperature carriers relies on the same mechanism (energy band warping due to strain) as modulation of infrared image induced electrons.⁸

The test sample was prepared at the U.S. Army Night Vision and Electro-Optics Laboratories by dual-source molecular beam epitaxy of $\text{Pb}_{1-x}\text{Sn}_x\text{Se}$ and SnSe on (111) cleaved BaF_2 . The growth rate was $1.1 \mu\text{m/h}$ and the substrate temperature was 340°C , yielding a film $3 \mu\text{m}$ thick. X-ray diffractometry and spectral response measurements of sister samples indicate a film composition of $\text{Pb}_{0.975}\text{Sn}_{0.025}\text{Se}$, which corresponds to a 300°K band gap of 0.25 eV ($5 \mu\text{m}$ cutoff). Room-temperature Hall measurements, again on sister samples, using the van der Pauw method⁹ indicate a resistivity of $7.1 \times 10^{-2} \Omega\text{cm}$, a mobility of $5 \times 10^2 \text{ cm}^2/\text{V sec}$ and a carrier concentration (p type) of $1.9 \times 10^{17}/\text{cm}^3$.

Using standard microelectronic photolithographic techniques, the film was first etched to a convenient size, using a 5% solution of Br in HBr. Then gold was electroplated for electrical contacts, leaving exposed a current path through the PbSnSe about 10 mm wide by 1 mm long. The total resistance was 40Ω .

A piezoelectric transducer (PZT) was bonded to one end of the substrate; Figure 1 shows the arrangement.

In order that the modulation be monitored, the configuration shown in Fig. 1 was employed. The device was mounted in a shielded box in order to minimize interference effects, and the input and output chambers were separated by a metal bridge that acted as a cutoff waveguide.

Upon careful investigation the modulation at the output current was observable only at several discrete frequencies with the maximum output at 600 kHz due to the resonances of the transducer. This modulation is at the same frequency as the input to the transducer. The output current can be derived from the measurement of the amplifier output voltage by

$$i_0 = i_{ia} = V_{out}/R_T, \quad (1)$$

where i_0 is the device output current (mA), i_{ia} is the amplifier input current (mA), V_{out} is the amplifier output voltage (V), and R_T is amplifier transresistance (Ω). For the amplifier used, $R_T = 87.74 \text{ k}\Omega$. At 600 kHz , $V_{out} = 0.4 \text{ V}$ peak to peak, giving a device output current $i_0 = 4.56 \mu\text{A}$. The percent modulation of the bias current by the acoustic signal is

$$\text{percent modulation} = (i_0/i_{dc}) 100, \quad (2)$$

where i_{dc} is the dc bias. With $i_{dc} = 2.33 \text{ mA}$, the modulation is about 0.2% . In order to check that the observed output is not simply feedthrough, the signal to the transducer was pulse modulated. There was an observable propagation delay across the substrate before the active thin film was reached by the acoustic wave. This proved that the effect was due to the acoustic pulse. This delay is about $60 \mu\text{sec}$ over a distance of 1 cm , yielding an effective velocity of 166 m/sec . This conflicts with the longitudinal propagation in the

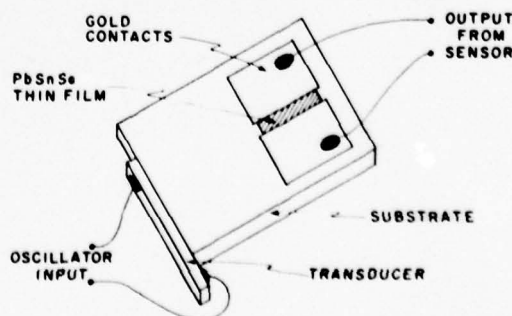


FIG. 1. The PbSnSe film deposited on BaF_2 . Note the PZT transducer bonded to the substrate. The transducer was shielded from the contact region. The substrate dimensions are $19.05 \text{ mm} \times 12.7 \text{ mm} \times 4.76 \text{ mm}$.

[100] direction given by¹⁰.

$$v_s = (C_{11}/\rho)^{1/2}, \quad (3)$$

where ρ is the density (g/cm³), and C_{11} is the longitudinal elastic constant [g/(cm/sec²)]. For BaF₂, $\rho = 4.886$ g/cm³ and $C_{11} = 0.891 \times 10^{12}$ g/(cm/sec²), giving a theoretical velocity of $v_s = 4.2791 \times 10^3$ m/sec.

Further investigation is required to resolve this discrepancy. We believe that cracks in the substrate may be responsible for introducing reflections between the upper and lower surfaces of the substrate, thus adding considerably to the path length. Alternatively, the small apparent velocity may be due to an unexpected acoustical mode.

Future experimentation should be directed toward obtaining a junction in the PbSnSe which should be more sensitive to ir. Also, the bias current will be changed in value and its effect on the frequency output will be studied. In conclusion, PbSnSe exhibits modulation by bulk acoustic waves of the same order of magnitude as that observed previously in CdS.⁸

The work reported here was performed under a contract with the U.S. Army Night Vision and Electro-optics Laboratories, Fort Belvoir, Va. The PbSnSe film on BaF₂ was fabricated by David Kaplan. The authors wish to acknowledge the assistance of David Helm of the Night Vision Laboratories.

¹M. Luukkala, P. Merilainen, and K. Saarinen, 1974 *Ultrasonics Symp. Proc.* (IEEE, New York, 1974), pp. 345-348.

²G.S. Kino, *Proc. IEEE* **62**, 724-748 (1976).

³L. P. Solie, *Proc. IEEE* **64**, 760-763 (1976).

⁴P.G. Kornreich, S.T. Kowel, D.J. Fleming, N.T. Yang, A. Gupta, and O. Lewis, *Proc. IEEE* **62**, 1072-1087 (1974).

⁵H. Gautier, G.S. Kino, and H.J. Shaw, *Ref. 1*, pp. 99-103.

⁶S.T. Kowel, P.G. Kornreich, K.W. Loh, A. Mahapatra, M. Mehter, P. Reck and B. Emmer, *IEEE Trans. Electron Devices* (to be published).

⁷S.T. Kowel, P.G. Kornreich, K.W. Loh, A. Mahapatra, and M. Mehter, 1977 *Ultrasonics Symp. Proc.* (IEEE, New York, 1977).

⁸A. Mahapatra, P.G. Kornreich, and S.T. Kowel, *Phys. Rev.* (to be published).

⁹L.J. van der Pauw, *Philips Res. Rep.* **13**, 1 (1958).

¹⁰A.J. Slobodnik, Jr., E.D. Conway, and R.T. Delmonico (unpublished).

APPENDIX IV.

STRAIN-INDUCED MODULATION OF PHOTOCONDUCTIVITY
IN THIN POLYCRYSTALLINE FILMS OF CADMIUM SULFIDE

Physical Review B, Volume 18, Number 6,
15 September, 1978

Strain-induced modulation of photoconductivity in thin polycrystalline films of cadmium sulfide

A. Mahapatra, P. G. Kornreich, and S. T. Kowel

Department of Electrical and Computer Engineering, Syracuse University, Syracuse, New York 13210

(Received 3 February 1978)

We have studied the modulation of the photoconductivity of polycrystalline films of CdS by elastic strain. The CdS films are vacuum deposited on soda-lime glass substrates. They are then suitably heat treated to yield films with light-to-dark conductivity ratios of 10^4 at 215 mcd. Elastic strains are generated in the film by propagating Rayleigh waves (surface acoustical waves) in the glass substrate. We have observed that the fractional change in conductivity due to strain shows prominent maxima and minima as a function of light intensity. The largest recorded fractional change in conductivity is about 10^{-3} at strains of the order of 10^{-7} . This is a much larger change than has been observed in single crystals of CdS. We have developed a new model to explain the strain-induced changes in the conductivity of our films. We assume the presence of a quasicontinuous distribution of impurity levels in the forbidden gap and assign deformation potentials to all these levels. Elastic strain shifts these levels and changes the number of electrons "trapped" in them significantly. This, in turn, changes the concentration of conduction electrons.

I. INTRODUCTION

Studies of strain-induced changes in the properties of single crystals are amply recorded in the literature. Langer¹ reported the shift in absorption edge of CdS crystals with pressure to have a slope of 4.9×10^{-6} eV/cm²/kg and also reported the fractional change in conductivity with pressure to be 1.1×10^{-4} cm²/kg for pure CdS and 10^{-6} cm²/kg for indium-doped CdS. Noting that a typical value for an elastic stiffness constant in CdS is 9.3×10^5 kg/cm², these values can be translated to yield the fractional change in conductivity per unit strain to be 102.3 for pure CdS crystals and 0.01 for indium-doped CdS. In a later paper, Boer *et al.*² reported results which, again, translated using the elastic stiffness constant quoted above, yield fractional changes in conductivity with unit strain of 111.6 for low-conductivity CdS and 2.79 for high-conductivity CdS. However, we have not found reports of the experimental study of the effect of strain on the photoconductivity of thin films of CdS in the literature. Such studies are difficult since it is not easy to apply static stresses to thin films.

In this paper, we study the modulation of electrical conductivity by strain in polycrystalline films of CdS. The CdS films are vacuum deposited on soda-lime glass substrates. The difficulty of applying static strains has been overcome by generating surface acoustical waves in the substrate using piezoelectric transducers. The strains thus generated are measured by a novel "tuned capacitor" method. An aluminum film is evaporated onto the glass substrate and a second aluminum film (evaporated on a glass plate) is positioned above it to form a capacitor. The strain wave in the

glass substrate flexes the lower metal film and changes the capacitance. These changes can be measured and used to calculate the strains associated with the acoustical wave. It is true that the strains generated by this technique are much smaller than those generated by static methods. However, since the signal is sinusoidal, measurement techniques can be made much more sensitive by use of phase synchronous detection.

We will show that in our films the fractional change in photoconductance demonstrates prominent peaks and dips when plotted as a function of light intensity. The largest recorded fractional changes in photoconductance are of the order of 10^{-3} at strains of 10^{-7} . This corresponds to a fractional change in conductivity of 10^4 per unit strain. This is a much larger change than has been observed in single crystals, as is evident from the references quoted earlier, and we are unable to reconcile our measurements with existing models.

We have developed a model based on the existence of impurity levels in the forbidden gap to explain the magnitude and characteristics of the observed strain-induced modulation of conductivity. We show that the strain shifts not only the extrema of the valence and conduction band, but also the energy of impurity levels. This results in a significant change in the number of electrons "trapped" in impurity levels and therefore in the concentration of conduction electrons.

We further show the possibility of utilizing measurements of strain-induced modulation of conductivity in semiconductors to investigate the deformation potentials of deep impurities and also the distribution of impurity states in the forbidden gap.

II. THEORY

A. Elastophotoconductance

We assume that the conductivity σ of a polycrystalline film depends on light intensity I and strain Σ , i.e.,

$$\sigma = \sigma(I, \Sigma). \quad (2.1)$$

If we now expand σ in a Taylor series in Σ about $\Sigma = 0$, we obtain,

$$\sigma = P(I) + M(I)\Sigma + (\dots), \quad (2.2)$$

where the dots represent higher-order terms, $P(I) = [\sigma(I, \Sigma)]_{\Sigma=0}$ is the usual photoconductivity of the film, and $M(I) = [\partial\sigma(I, \Sigma)/\partial\Sigma]_{\Sigma=0}$ is the change in photoconductivity with strain.

Here we have only retained terms to first order in the strain. The usual photoconductivity term $P(I)$ reduces to the dark conductivity σ_D at zero light intensity.

We know that the electrical conductivity is a symmetric second-rank tensor. Therefore, $P(I)$ must also be a symmetric second-rank tensor. $M(I)$, on the other hand, is a fourth-rank tensor, since the strain Σ is itself a second-rank tensor.

We will define the fourth-rank tensor $M(I)$ to be the elastophotoconductivity tensor. Since the strain is a symmetric tensor, M can, at the most, have 36 independent components. Further, since elastophotoconductivity is a material property, it must exhibit all the symmetry properties of the material. Now, CdS exhibits hexagonal symmetry and belongs to the symmetry class C_{6v} . This symmetry requirement further reduces the number of independent components in M to only six.³ It is tempting to think that a polycrystalline film would be essentially isotropic because of the random orientation of crystallites. However, this is often not the case. The fabrication technique we use usually results in the crystallites being oriented with the z axes perpendicular to the plane of the film, although the x and y axes are randomly oriented in the plane of the film.⁴ It can be shown, however, that such a random orientation does not reduce the number of independent constants in M to less than six.⁵

The technique employed to generate the strain resulted only in the strain components Σ_{xx} and Σ_{yy} . Therefore, our measurements yield only the change in the conductivity component σ_{yy} by the strains Σ_{xx} and Σ_{yy} . This change averaged over all orientations of the x and y axes of the crystallite in the plane of the film can be shown to be

$$\Delta\sigma_{yy} = (M\Sigma)_{yy} = (\frac{1}{2}M_{11} + \frac{1}{2}M_{12})\Sigma_{xx} + M_{13}\Sigma_{yy}, \quad (2.3)$$

where M_{11} , M_{12} , and M_{13} are components of the elastophotoconductance tensor for a single crystal.⁶

Further, we show in Appendix A that in our films the strains Σ_{xx} and Σ_{yy} are related through the equation, $\Sigma_{yy} = C\Sigma_{xx}$, where C is a constant depending only on the frequency of the strain wave. Therefore, Eq. (2.3) becomes,

$$\Delta\sigma_{yy} = (M\Sigma)_{yy} = (\frac{1}{2}M_{11} + \frac{1}{2}M_{12} + CM_{13})\Sigma_{xx} = M_0\Sigma_{xx}, \quad (2.4)$$

where

$$M_0 = \frac{1}{2}M_{11} + \frac{1}{2}M_{12} + CM_{13}. \quad (2.5)$$

We will show in Sec. V that M_0 is the only linear combination of elastophotoconductance components that we can measure.

For our purpose, it will be helpful to note that the fractional change in the P_{yy} component of the photoconductivity is, from Eq. (2.4),

$$(\Delta\sigma_{yy}/P_{yy}) = (M_0\Sigma_{xx}/P_{yy}). \quad (2.6)$$

In fact, we will measure only this fractional change. Now, if we assume that the strain does not change the mobility of the electrons, the change in conductivity must result from a change in concentration of free electrons, n . Therefore, Eq. (2.6) can be written

$$\Delta\sigma_{yy}/P_{yy} = \Delta n/n = M_0\Sigma_{xx}/P_{yy}. \quad (2.7)$$

In Sec. II B we will consider different physical models in an attempt to correlate M_0 with the physical properties of our films. The purpose of all calculations will be to calculate the fractional change in concentration of free electrons, $\Delta n/n$.

B. Theoretical model for elastophotoconductance

It became evident from our preliminary measurements that the modulation of the photoconductivity by elastic strain possesses many interesting properties. For instance, the fractional change in photoconductivity due to strain changes from 10^{-5} at 0.065 mcd to 10^{-3} at 4300 mcd. However, the variation, far from being monotonic, exhibits prominent dips and peaks. Measurements made at different wavelengths of light yield similar results although the positions of the extrema change. In an attempt to explain these diverse characteristics we look at three different mechanisms: 1. barrier model, 2. deformation potential model, and 3. change in trap density as a result of deformation.

1. Barrier model

This model exploits the fact that most vapor-deposited films are polycrystalline. The crystallites have properties different from those possessed by the intercrystallite region. One assumes the exis-

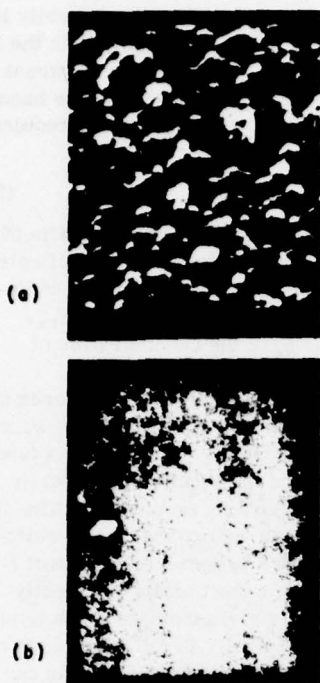


FIG. 1. Scanning-electron-microscope studies of CdS films. (a) Uncured films. (b) Cured films.

tence of a potential barrier ϕ between crystallites and, in analogy with semiconductor p - n junctions, writes down the current voltage (I - V) characteristics as,

$$I = I_0 e^{-\phi/kT} (e^{eV_d/kT} - 1). \quad (2.8)$$

Here e is the electronic charge, k is the Boltzmann constant, I_0 is a constant, and V_d is the drift voltage across each barrier. Equation (2.8), used by many authors, predicts highly nonlinear I - V characteristics if $eV_d > kT$.

From scanning-electron-microscope pictures (Fig. 1), we know that the crystallites are about $1\mu\text{m}$ wide. The electrode spacing is 100 microns. Therefore, if 20 V are applied to the electrodes, the voltage across each barrier is about 0.2 V. At room temperature (24°C), this gives $eV_d \gg kT$, and one would expect highly nonlinear I - V characteristics. However, the observed I - V curves are linear to applied voltages as high as 30 V. Furthermore, we have not been successful in finding experimental confirmation of the I - V characteristics predicted by Eq. (2.8) in the literature. This leads us to conclude that either the barrier model is not applicable to our films or that Eq. (2.8), quoted in many papers,⁶ is an oversimplification.

It is interesting that strain-induced changes in the conductivity of single crystals of CdS, which

were briefly mentioned in Sec. I, seem to support the view that potential "barriers" are probably not responsible for the phenomenon we have observed. For instance, Langer¹ has reported the fractional changes in conductivity for unit strain to be 102.3 for pure CdS crystals and 0.01 for indium-doped CdS crystals. Clearly, the effect depends markedly on the presence of dopants and, therefore, on the presence of impurity levels. Boer et al.² have reported fractional changes in conductivity with unit strain of 111.6 for low-conductivity CdS crystals and 2.79 for high-conductivity CdS crystals. Thus, the effect seems to decrease markedly as the conductivity of the crystals increases. We will show in subsequent sections that in our polycrystalline CdS films, the fractional change in conductivity due to strain shows qualitative features similar to the ones reported for single crystals of CdS and quoted above. Therefore, the origin of the effect is very likely the same in single crystals of CdS and polycrystalline films of CdS; since single crystals cannot have potential "barriers," we are inclined to believe that such "barriers" may exist but cannot be responsible for the effect we have studied.

2. Deformation potential model

It has been shown by Pikus and Bir⁷ that for the CdS structure the only first-order change in band structure due to strain is a change in the band gap. In fact, the change in band gap ΔE_g can be written

$$\Delta E_g = D_1(\Sigma_{xx} + \Sigma_{yy}) + D_2 \Sigma_{zz} \quad (2.9)$$

where the Σ_{ij} 's are components of the strain tensor. The constants D_1 and D_2 are called deformation potentials. They have been experimentally measured in CdS by Langer⁸ et al. who report the following values for D_1 and D_2 :

$$D_1 = -2.8 \text{ eV}, \quad D_2 = -4.5 \text{ eV}. \quad (2.10)$$

Now, the concentration n of free electrons is

$$n = N_c \exp(E_{Fn} - E_c)/kT, \quad (2.11)$$

where N_c is the effective density of states in the conduction band, E_{Fn} is the quasielectron Fermi level, and E_c is the bottom of the conduction band. A small change ΔE in E_c as a result of strain would produce a fractional change in conductivity of the order of $\Delta E/kT$. For strains of the order of 10^{-7} which are the strains generated in our experiments, this implies a fractional change in conductivity of the order of 10^{-5} . However, the highest values of the fractional changes in conductivity measured by us are of the order of 10^{-3} . Hence, it appears difficult to explain the signals we ob-

served as due to strain induced change in band gap.

3. Change in trap densities as a result of deformation

In our consideration of the deformation potential model, we saw that the conduction- and valence-band extrema shifted in energy as a result of elastic strain. However, we did not take into account the presence of defect energy levels in the forbidden gap. It is well known that these defect states play an important role in the photoconduction mechanism.

We assume that the strain not only shifts the extrema of the valence and conduction bands but also the position of energy levels within the forbidden gap. Moreover, the shift in energy of any level depends on its position within the gap. In fact, one can now define two energy-dependent deformation potentials, $D_1(E)$ and $D_2(E)$, such that an impurity level at energy E , would shift to an energy E' given by

$$E' = E + \Delta E = E + D_1(E)\Sigma_{xx} + D_2(E)\Sigma_{zz} \quad (2.12)$$

In the most general case, when all six components of strain exist, one must define six deformation potentials. However, for our purpose, only two of the deformation potentials need be considered, since only two components of strain are non-zero. It is true that even if the number of nonzero strain components in the laboratory coordinate system is two, the number of such components in the crystallite coordinate system would generally be more. However, it is easy to show that if the strains in the crystallite coordinate system are averaged over all possible orientations of the x and y axes of the crystallite, one can still write an equation similar to Eq. (2.12) without loss of generality.⁸

The change in the position of impurity levels is interesting because it implies a significant change in the distribution of impurity levels. Clearly, all the levels that were originally at energy $E - \Delta E$ will now appear at energy E . If the original impurity distribution was characterized by the function $g_0(E)$ the distribution function with strain, $g(E, \Sigma)$ would be given by

$$g(E, \Sigma) = g_0(E - \Delta E). \quad (2.13)$$

Assuming ΔE to be much smaller than E , we can expand the right-hand side to first order in ΔE to obtain

$$g(E, \Sigma) = g_0(E) - \frac{dg_0}{dE} \Delta E. \quad (2.14)$$

Let us assume that the electron Fermi level in the dark is located at E_F . When the CdS film is illuminated by light, the electron Fermi level

moves up to E_{Fn} . If we assume the Fermi function to be a step function, all of the impurity levels between E_F and E_{Fn} which were empty, in the dark, will now be filled. Of course, these electrons must have been excited out of the valence band and out of hole traps. Electrical neutrality requires that

$$n + n_t = p + p_t, \quad (2.15)$$

where n is the concentration of electrons in the conduction band, p is the concentration of holes in the valence band, n_t is the total number of impurity levels contained between E_F and E_{Fn} , $\int_{E_F}^{E_{Fn}} g_0(E) dE$, and p_t is the concentration of trapped holes.

Equation (2.15), of course, must hold even under the application of strain, although p , p_t , n , and n_t could change individually. Now, n_t is a function of $g_0(E)$ and since the distribution of impurity states changes with strain, so must n_t . The change in n_t will reflect itself in a change in n , which through recombination processes will affect p and p_t . The change in n_t cannot affect p_t directly since impurity levels are associated with impurity atoms which are physically in different parts of the crystal. The only way impurity levels can "communicate" is through the conduction or valence band. Now, in our experiments we use sinusoidal strains at a frequency of 2 MHz which corresponds to a time period of 0.5×10^{-6} secs. The lifetime of electrons, which is a gauge of the speed of recombination processes, is about 10^{-3} sec.⁹ This means that the strains vary much too fast for the resulting changes in n_t and n to affect the values of p and p_t . Therefore, we can assume that the right-hand side of Eq. (2.15) is unchanged on application of strain, i.e., for fixed light intensity,

$$(n + n_t)_{\text{without strain}} = (n + n_t)_{\text{with strain}}. \quad (2.16)$$

In all that follows the subscripts 1 and 2 will refer to quantities before and after the film is strained, respectively. Thus,

$$n_1 = N_c \exp(E_{Fn} - E_c)/kT, \quad (2.17)$$

$$n_{t1} = \int_{E_F}^{E_{Fn}} g_0(E) dE. \quad (2.18)$$

On the application of strain the concentration of conduction electrons changes. It is clear from Eq. (2.17) that this will change the electron Fermi level. Therefore, the number of conduction electrons in the presence of strain is,

$$n_2 = N_c \exp[(E_{Fn} - E_c + \Delta E_{Fn} - \Delta E_c)/kT].$$

For $(\Delta E_{Fn} - \Delta E_c)/kT \ll 1$, we obtain,

$$n_2 = n_1 [1 + (\Delta E_{Fn} - \Delta E_c)/kT]. \quad (2.19)$$

Therefore, the fractional change in the number of conduction electrons is

$$\Delta n/n = (n_2 - n_1)/n_1 = (\Delta E_{Fn} - \Delta E_c)/kT. \quad (2.20)$$

We note from Eq. (2.14) that the strain changes the density of impurity states. The Fermi level is also changed by an amount ΔE_{Fn} . Therefore, in analogy with Eq. (2.18) we can write

$$n_2 = \int_{E_F}^{E_{Fn} + \Delta E_{Fn}} g(E, \Sigma) dE.$$

Using Eq. (2.15), and retaining terms to first order in ΔE and ΔE_{Fn} yields

$$n_2 = \int_{E_F}^{E_{Fn}} g_0(E) dE + g_0(E_{Fn}) \Delta E_{Fn} - \int_{E_F}^{E_{Fn}} \frac{dg_0}{dE} \Delta E dE. \quad (2.21)$$

Now, from Eq. (2.16) we must have

$$n_1 + n_{II} = n_2 + n_3.$$

By substituting for these quantities from the above equations, it is easy to show that

$$\frac{\Delta E_{Fn}}{kT} = \frac{1}{n_1 + g_0(E_{Fn})kT} \left(n_1 \frac{\Delta E_c}{kT} + \int_{E_F}^{E_{Fn}} \frac{dg_0}{dE} \Delta E dE \right). \quad (2.22)$$

Now we are in a position to calculate the fractional change in the concentration of free electrons. Using Eq. (2.22) in Eq. (2.20) gives

$$\frac{\Delta n}{n} = \frac{1}{n_1 + g_0(E_{Fn})kT} \times \left(-g_0(E_{Fn}) \Delta E_c + \int_{E_F}^{E_{Fn}} \frac{dg_0}{dE} \Delta E dE \right). \quad (2.23)$$

Now, $g_0(E_{Fn})kT$ is the number of impurity levels in a region kT near the Fermi level. In our films it is always larger than 10^{15} cm^{-3} . On the other hand n_1 is of the order of 10^{12} cm^{-3} . Therefore, we can drop n_1 in comparison to $g_0(E_{Fn})kT$ in Eq. (2.23). This gives

$$\frac{\Delta n}{n} = -\frac{\Delta E_c}{kT} + \frac{1}{g_0(E_{Fn})kT} \int_{E_F}^{E_{Fn}} \frac{dg_0}{dE} \Delta E dE. \quad (2.24)$$

Note that the first term in $\Delta n/n$, i.e., $\Delta E_c/kT$, is exactly the one obtained by using the deformation potential model. We believe that the second term, which contains the deformation potentials through ΔE , is largely responsible for the change in conductivity with strain. We also note from Eq. (2.24) that the fractional change in concentration of conduction electrons should decrease inversely as

$g_0(E_{Fn})$. In fact, we can quantitatively show that $\Delta n/n$ should have its extrema at the same values of E_{Fn} as $g_0(E_{Fn})$. To see this we multiply Eq. (2.24) by $g_0(E_{Fn})$ and then differentiate with respect to E_{Fn} . This gives, after simplification,

$$\frac{d}{dE_{Fn}} \left(\frac{\Delta n}{n} \right) = \frac{1}{g_0(E_{Fn})} \frac{dg_0}{dE_{Fn}} \left(\frac{\Delta E}{kT} (E_{Fn}) - \frac{\Delta E_c}{kT} - \frac{\Delta n}{n} \right). \quad (2.25)$$

Therefore, if dg_0/dE_{Fn} is zero, so is $(d/dE_{Fn})(\Delta n/n)$. This means that the extrema of g_0 and $\Delta n/n$ coincide.

III. FABRICATION AND CHARACTERIZATION OF CdS FILMS

A. Film fabrication

We followed the technique developed by Boer *et al.*¹⁰ with slight modifications. Our CdS films were fabricated on substrates of soda-lime glass. The substrates were suitably cleaned and held in a substrate holder, which was then placed in a vacuum system. The CdS powder was packed in a small, fused-quartz bottle which had a molybdenum filament wound around it so that it could be heated to the temperature necessary for evaporation of the CdS. The substrate holder, along with the glass pieces, was held about 20 cm above the CdS source. It had suitable heating elements running through it so that it could be heated to about 210°C. The vacuum chamber was evacuated to about 10^{-5} Torr and the CdS was evaporated at 800°C.

It was found that these evaporated films had a poor photocurrent-to-dark-current ratio, hereafter referred to as light-to-dark (LD) ratio. The well-known reason for this is that the evaporated films have a poor stoichiometry. The CdS dissociates on evaporation due to the high evaporation temperature (800°C). The Cd and S deposit separately on the substrate and then recombine to form CdS. However, since the vapor pressure of S is higher than that of Cd at 210°C, the substrate temperature, much of the S re-evaporates from the substrate leaving the film Cd rich. This increase, the dark conductivity of the film and reduces the LD ratio. If the substrates were at room temperature, the difference in the vapor pressures of Cd and S would be larger, thus making the stoichiometry even poorer. It has been found by many researchers¹¹ that a substrate temperature somewhat above 200°C results in the best stoichiometry.

To improve the photosensitivity of the films they have to be heat treated or "cured" after evaporation. This is done by suitably placing the substrate in a furnace heated to 650°C. Also placed in the furnace is a fused-quartz boat with suitable

amounts of CdS and copper powder. At the same time, a constant flow of N_2 along with traces of HCl and O_2 is maintained through the furnace tube. The high temperature serves two functions. It helps to re-evaporate much of the free cadmium in the film.¹² Notice that the vapor pressure of Cd at 650°C is about 100 Torr so that it will undergo some evaporation. However, CdS has a boiling point of 980°C, so the film itself will not evaporate. The high temperature also gives the CdS molecules enough kinetic energy to regroup and form crystallites. Thus "curing" facilitates recrystallization.¹¹

The individual roles of the different doping elements in the curing process is not well understood. The copper presumably helps in recrystallization.¹¹ The HCl acts as a carrier for the CdS and Cu and also dopes the film with Cl. The role of minute traces of O_2 is understood least of all, although its presence is absolutely essential. Films cured without O_2 have very poor LD ratios.

After suitable curing we obtain films with LD ratios of the order of 10^4 at 200 mcd and with response times of the order of 10 msec. In comparison, uncured films typically have a LD ratio of 5 and response times as large as a few seconds.

B. Film characterization

To study the surface properties of the films, they were examined under a scanning electron microscope (SEM) at various stages of fabrication. The results are shown in Fig. 1. It is clear that the surface of the uncured film is almost completely lacking in structure. The cured film, on the other hand, does show considerable crystallization. The crystallites are irregularly shaped, but seem to fit smoothly into each other. The crystallites range in size from 0.5 to 1 μ m. On top of the film is what appears to be a white deposit. We are unable to explain the presence of this deposit, but it probably results from the "curing" technique we have employed.

We measured the optical transmittance of a cured and an uncured film. The results are shown in Fig. 2. The curve for the uncured film does show an absorption edge at around 520 nm. However, the cured film shows a much sharper absorption edge, which indicates considerable recrystallization due to curing.

Next we measured the spectral distribution of the photocurrent. Since the light source used did not have a flat intensity output over the range of wavelengths explored, the measured currents had to be suitably normalized. Figure 3 shows the photocurrent-versus-light spectral distribution normalized to equal incident photon densities. The

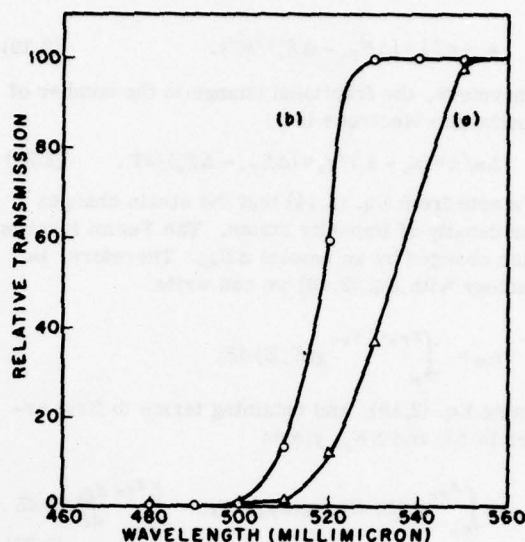


FIG. 2. Relative optical transmission of CdS films (normalized to 100% at 540 m μ): (a) "uncured" film; (b) "cured" film.

photocurrent maxima at 510 nm clearly corresponds to the band edge and yields a band gap of 2.43 eV. At wavelengths smaller than 510 nm, the photocurrent drops sharply. At wavelengths larger than 510 nm, there is a flat region extending from 525 to 555 nm. Clearly the current in this region arises from electrons excited to the conduction band from impurity levels lying close to the valence band. The end of the plateau at 555 nm indicates a hole trap 2.23 eV from the conduction band or 0.2 eV from the valence band.

We measured the dark current as a function of temperature in the range of 24°C to 90°C. The re-

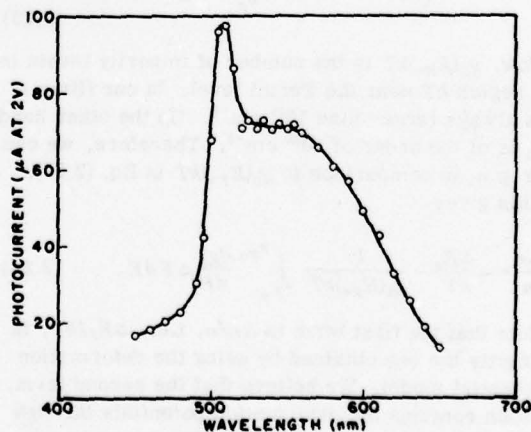


FIG. 3. Dependence of photocurrent on light wavelength at 24°C (normalized to equal incident photon density).

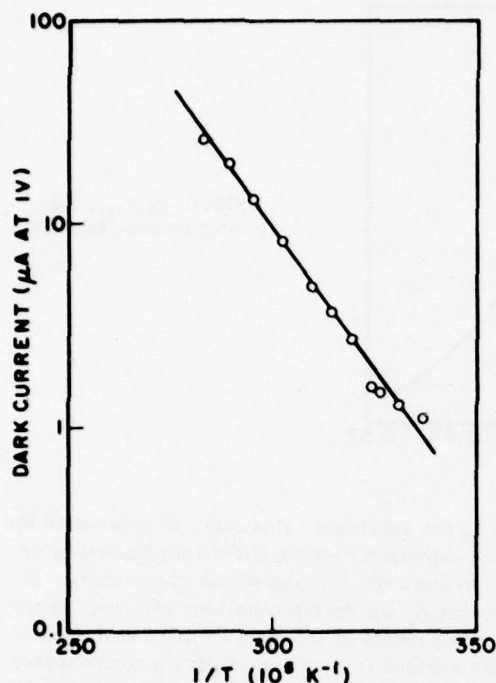


FIG. 4. Dark current as a function of temperature between 24 and 90°C.

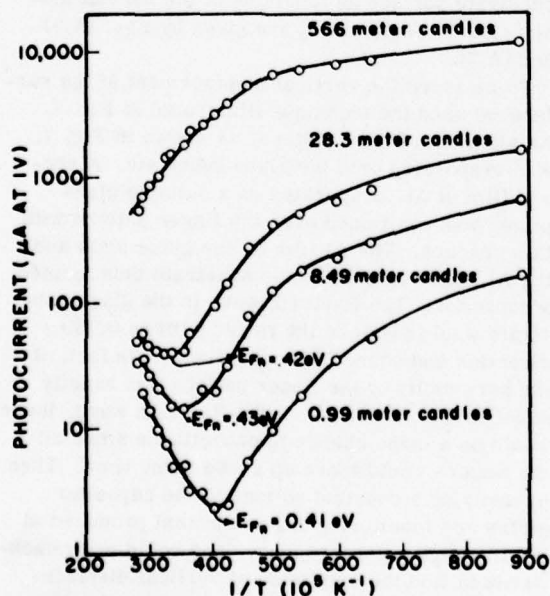


FIG. 5. Photocurrent as a function of reciprocal temperature at constant white-light intensity.

sults are shown in Fig. 4. The curve is fairly linear and the slope shows the Fermi level in the dark to be located 0.56 eV below the conduction band. From the position of the Fermi level one can calculate the electron density

$$n = N_c \exp(E_F - E_c)/kT.$$

Here N_c is the effective density of states in the conduction band and is given by $2(M_{eff}kT/2\pi k^2)^{3/2}$. M_{eff} is the effective electron mass in the conduction band and typically is 0.2 times the bare mass of an electron.¹³ Once n and the conductivity σ are known, the electron mobility μ can be calculated. Such a calculation yields an electron mobility of 228 cm²/V sec. Since the mobility is relatively insensitive to temperature, we will use this value of μ hereafter to obtain the value of n from the conductivity under all other circumstances.

The results of measuring the variation of photocurrent with temperature for different light intensities are shown in Fig. 5. All the curves up to 28 mcd show a minimum of the photocurrent which occurs when the electron Fermi level is located 0.42 eV from the conduction band. Clearly, this indicates a strong electron trap level located about 0.42 eV from the conduction band. As the electron Fermi level approaches these trap levels, more and more of them are converted to recombination centers. This decreases the electron lifetime and therefore, the photocurrent.

Once the electron Fermi level crosses the electron trap levels, all the curves show a constant slope for a wide range of temperatures. This is interpreted as follows. Let us assume there is a hole trap located at an energy E_s from the valence band, with the hole density in the valence band p and the hole density in the traps p_t in thermal equilibrium. Therefore,

$$p = p_t e^{-E_s/kT}. \quad (3.1)$$

Now, concentration of free electrons n in the conduction band is inversely proportional to the concentration of recombination centers occupied by holes, p_r . However p_r itself is proportional to the density of holes in the valence band. This implies that the concentration of free electrons is inversely proportional to the concentration of free holes, that is,

$$n \propto p^{-1} \propto p_t^{-1} e^{E_s/kT}. \quad (3.2)$$

Also, because of quasineutrality, the hole density in hole traps, p_t , is about equal to the hole density of trapped electrons. Therefore,

$$p_t \approx \int_{E_F}^{E_{Fn}} g_0(E) dE, \quad (3.3)$$

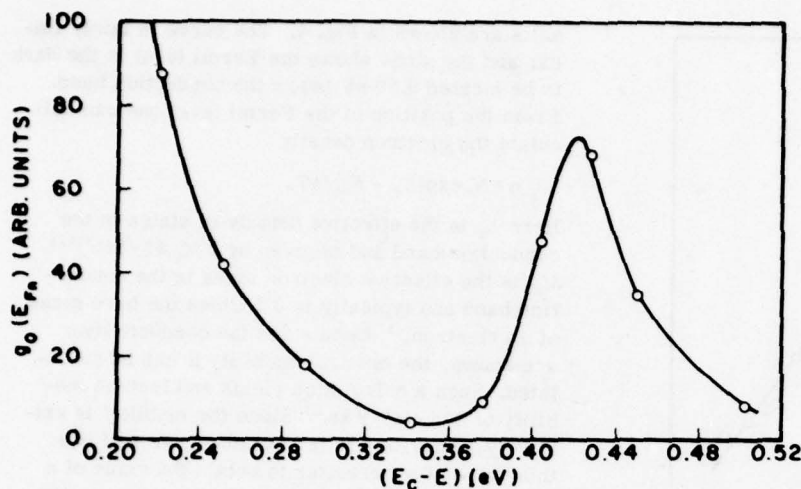


FIG. 6. $g_0(E_{Fn})$, calculated by using Eq. (3.4).

where $g_0(E)$ is the energy distribution of electron traps and E_F is the electron Fermi level in the dark. Substituting Eqs. (3.1) and (3.3) in Eq. (3.2) gives

$$n \propto \exp(E_a/kT) / \int_{E_F}^{E_{Fn}} g_0(E) dE. \quad (3.4)$$

This indicates that the slope of the natural log of n ($\ln n$) vs $1/T$ curve will be constant and determined by E_a only if the density of trapped electrons does not depend markedly on light intensity or temperature. This can be fulfilled only if the trap density in the corresponding range of the quasi-Fermi level is very small as compared to the density of the deeper traps near 0.42 eV. We can now use the slope of the curves to determine E_a . Such a calculation shows the electron trap to be located 0.15 eV above the valence band. Clearly these must be the same hole traps determined earlier from Fig. 3.

Now that we know E_a we can work backwards from Eq. (3.4) to get $g_0(E)$ keeping in mind that n is proportional to the photocurrent i . Such a calculation made from the curve at 0.99 mcd in Fig. 5 yields the $g_0(E)$ curve of Fig. 6. Although this curve does not give the absolute values of the density of impurity states, it shows the position of peaks and valleys in the density of states. The peak at 0.42 eV (which we had expected) and the minimum at 0.34 eV will figure prominently in the measurements of elastophotoconductance described later.

IV. STRAIN RELATED MEASUREMENTS

A. Measurement of strain

From our experiments we can only measure the component of the displacement normal to the sur-

face of the substrate. However, to determine the strain dependence of the CdS film properties we need to know the various strain components. In Appendix A, we derive equations relating the normal components of the displacement at the substrate surface to the various strain components. We assume that the Rayleigh wave propagates in the x direction with uniform wave fronts along the y axis. Such a wave has only three strain components, the longitudinal strain components Σ_{xx} and Σ_{zz} and the shear strain component Σ_{xz} . However, at the traction free surface of the substrate the shear strain component vanishes identically. The remaining longitudinal strain components at the substrate surface as functions of the normal displacement component u_0 are given by Eqs. (A.6) and (A.7).

To measure the vertical displacement at the surface we used the technique illustrated in Fig. 7. An aluminum finger pattern, as shown in Fig. 7, was evaporated onto the glass substrate. A second film of Al, evaporated on a suitable glass plate, was positioned over the finger pattern with thin spacers. The Al film on the glass plate and the Al finger pattern on the substrate thus formed a capacitor. The Rayleigh wave in the glass substrate would displace the finger pattern in the z direction and change the capacitance. In fact, if the periodicity of the finger pattern was exactly equal to the wavelength of the Rayleigh wave, there would be a large change in capacitance since all the fingers would move up at the same time. Then, by applying a constant voltage to the capacitor plates and monitoring the ac current produced at the Rayleigh wave frequency, one could work backwards to find the amplitude of vertical displacement. The necessary formula for doing this can be shown to be

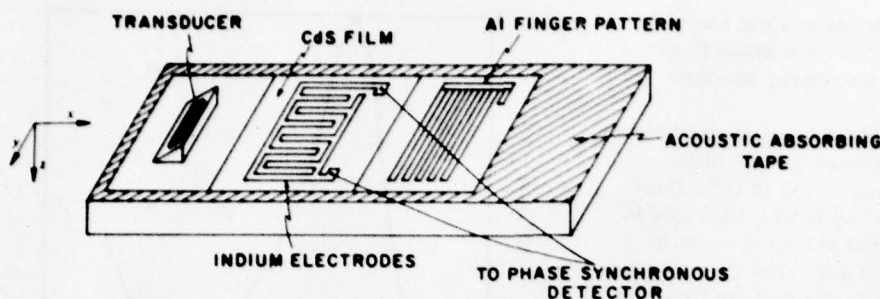


FIG. 7. Aluminum finger pattern used to measure magnitude of elastic strains.

$$i_t = (8V_c C^2 f^3 / E_0 b v_s N) u_0 \sin 2\pi f t, \quad (4.1)$$

where i_t is the ac current from the capacitor V_c is the voltage applied to the capacitor, C is the measured capacitance, f is the Rayleigh wave frequency, b is the length of the metal fingers, v_s is the surface wave velocity, N is the total number of metal fingers, and u_0 is the amplitude of vertical displacement at the surface. It is clear that if one could measure i_t , it would be possible to calculate u_0 since all the other quantities in Eq. (4.1) are known.

For a transducer frequency of 2.1 MHz, and a transducer driving voltage of 4 V (peak to peak), the measured strains were

$$\Sigma_{xx}^0 = 1.9 \times 10^{-7}, \quad \Sigma_{xx} = -0.408 \times 10^{-7}. \quad (4.2)$$

The negative sign of Σ_{xx}^0 indicates that it is out of phase with Σ_{xx}^0 .

B. Measurement of elastophotocurrent

A complete schematic diagram of the experimental arrangement used to measure elastophotocurrent signals is shown in Fig. 7. As the traveling acoustical wave passed through the CdS film, the resulting strains modulated the conductivity of the film. The modulation signals were detected and amplified by a current amplifier with input impedance of about 20 Ω . If the input current to a current amplifier is i_{ac} , and if the output voltage is V_{ac} , the transresistance R_T is defined as

$$R_T = V_{ac} / i_{ac}. \quad (4.3)$$

R_T can be determined by putting in a known ac current into the amplifier and measuring the output voltage. Once R_T is known, Eq. (4.3) can be used to calculate i_{ac} from the observed values of V_{ac} . The output of the current amplifier was fed to a network analyzer. This made possible the measurements of currents as small as 10^{-9} A. The substrate was mounted in an aluminum box designed to minimize electromagnetic feedthrough from the transducer driving circuit to the pickup amplifier. This was accomplished by separating the chambers containing the driving circuit and

the pickup amplifier by a metal tunnel 4 cm long.

In all our measurements, we used a "bar" light pattern of the kind shown in Fig. 13. The transducer had its strongest resonance frequency at about 2.1 MHz. Therefore, all measurements were made at this frequency. This, of course, meant projecting a "bar" pattern with the appropriate periodicity. The expression for the ac current, i_{ac} generated at the fundamental Fourier frequency of the "bar" pattern (the frequency at which the wavelength of the Rayleigh waves equals the repetition interval of the pattern) has been shown in Appendix B to be

$$i_{ac} = \frac{2}{\pi} i_{dc} \frac{M_0(I_0)}{P_{yy}(I_0)} \Sigma_{xx}^0. \quad (4.4)$$

In our model to explain elastophotocurrent we have assumed that the strain modulates the concentration of free electrons $\Delta n/n$ and not the mobility of electrons. Under this assumption, we can use Eq. (2.7) to rewrite Eq. (4.4)

$$i_{ac} = \frac{2}{\pi} i_{dc} \frac{\Delta n}{n}. \quad (4.5)$$

From our measurements, we can determine i_{ac} while i_{dc} is already known. Thus Eq. (4.5) can be used to calculate the fractional change in concentration of free electrons. Since we have also measured the strain components Σ_{xx}^0 , we can use Eq. (4.4) to calculate M_0/I_0 . The photoconductivity component P_{yy} can itself be measured independently. Thus, we are in a position to calculate M_0 , which then gives us an idea of the magnitude of the change in conductivity due to strain.

We have found experimentally that our CdS films are, unfortunately, not uniform. Their photoconducting properties do vary somewhat over the contact area. This probably results from the technique used for "curing" the films. In the case, when the projected image is a "bar" pattern, we work at the fundamental Fourier frequency of the picture. At this frequency it is clear that the contributions of all the lighted portions are in phase. Hence, although the individual contributions may be different due to nonuniformity, the total signal is obtained by adding all the contributions. Thus

film nonuniformity only serves to yield signals which have been averaged over the whole film. All calculated quantities, therefore, are also averaged parameters.

The "bar" pattern used had a fundamental Fourier spatial frequency corresponding to 2.21 MHz. Since the velocity of surface waves in soda-lime glass is 3128 m/sec, this implies $2L \approx 1.5$ μ m in Fig. 13. The transducer was driven by a signal with peak to peak voltage of 4 V. The current amplifier kept the dc current i_{dc} through the CdS film at 1.01 mA. At the lowest light intensities used it was difficult to maintain such a high current (since film resistance would go up as high as 100 k Ω). At these intensities a resistor (22 k Ω) was put in parallel with the sample in order to maintain the proper 1.01 mA amplifier bias current while decreasing the sample current. The voltage across the sample was measured so that one could calculate the part of the bias current which went through the sample.

The photocurrent of the sample as a function of white light was measured at room temperature (24°C) and a simple calculation yielded

$$P_{yy}(I_0) = 173 I_0^{0.84} \frac{S}{m} \quad (4.6)$$

with I_0 in mcd.

Next we measured the ac currents i_{ac} generated by the strain at different white-light intensities. For purposes of comparison with the model of elastophotoconductivity that we have proposed in Sec. I, it was necessary to plot $\Delta n/n$ as a function of the electron Fermi level E_{Fn} . At any light intensity, E_{Fn} can be calculated using the photoconductance of the film and electron mobility determined in Sec. IV (228 cm²/V sec). A plot of $\Delta n/n$ vs E_{Fn} for different white-light intensities is given in Fig. 8.

In order to determine if the elastophotoconductance signals had any dependence on the wavelength of light, measurements similar to those in Fig. 8 were made at three different wavelengths. For this purpose interference filters were used. The results are shown in Figs. 9-11. It was difficult to explore a wider range of wavelengths since we did not have a source which would generate enough intensity at these wavelengths.

V. CALCULATIONS AND DISCUSSION OF RESULTS

As a result of the measurements in Sec. IV, we are now in a position to calculate some of the constants associated with elastophotoconductance in our films. From Eq. (4.6) at 70 mcd we have

$$P_{yy} = 113.2 \text{ S/m.}$$

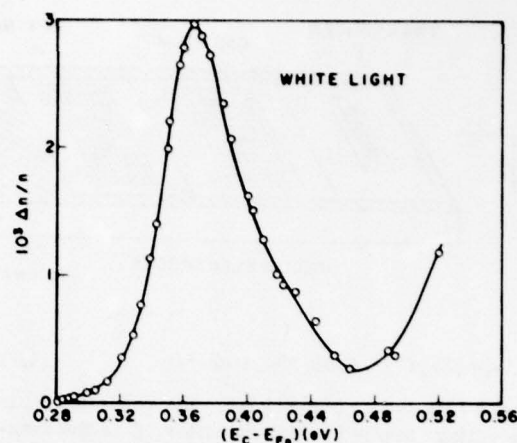


FIG. 8. Strain induced fractional change in concentration of conduction electrons $\Delta n/n$ as a function of $E_c - E_{Fn}$.

Using these values of $\Delta n/n$ and P_{yy} in Eq. (2.7) and the value of $\Sigma_{xx}^0 (= 1.9 \times 10^{-7})$ quoted in Eq. (4.2), we obtain

$$M_0 = 1.76 \times 10^6 \text{ S/m at 70 mcd.} \quad (5.1)$$

Again, from Fig. 8 we note that at 0.689 mcd $\Delta n/n$ is 2.65×10^{-4} , and from Eq. (4.5),

$$P_{yy} = 2.35 \text{ S/m.}$$

Again, using Eq. (2.7), we obtain

$$M_0 = 3.28 \times 10^3 \text{ S/m at 0.689 mcd.} \quad (5.2)$$

Equations (5.1) and (5.2) show that M_0 changes by more than two orders of magnitude between 0.689 and 70 mcd. Therefore, the change in conductivity due to strain, of which M_0 is a measure, has a

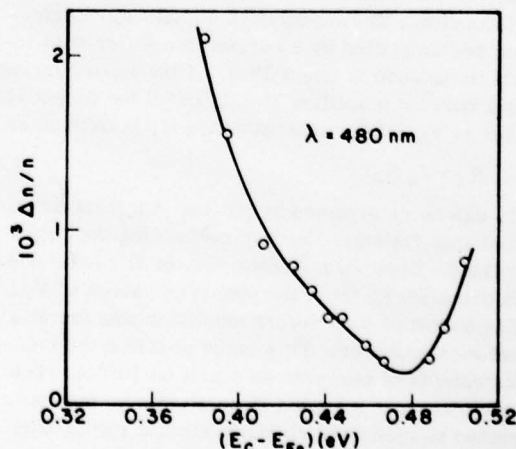


FIG. 9. $\Delta n/n$ as a function of $E_c - E_{Fn}$ for light of wavelength 480 nm.

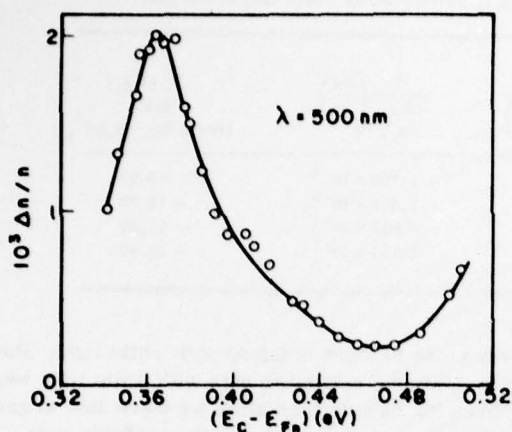


FIG. 10. $\Delta n/n$ as a function of $E_c - E_{Fn}$ for light of wavelength 500 nm.

marked dependence on light intensity.

Now let us look closely at the variation of the fractional change in concentration of free electrons $\Delta n/n$ with electron Fermi level E_{Fn} , shown in Fig. 8. In Sec. I, we used Eq. (2.25) to show that the extrema of $\Delta n/n$ should coincide with the extrema in the density of impurity states, $g_0(E_{Fn})$. From Fig. 6, we see that $g_0(E_{Fn})$ has a peak when $E_c - E_{Fn}$ is 0.422 eV and a minimum when $E_c - E_{Fn}$ is 0.350 eV. From Fig. 8 we see that $\Delta n/n$ has a minimum when $E_c - E_{Fn}$ is 0.466 eV and a maximum when $E_c - E_{Fn}$ is 0.366 eV. This indicates that the extrema in $g_0(E_{Fn})$ and $\Delta n/n$ are indeed close to each other. The slight differences observed, 0.044 eV at the most, are easily explained by the fact that the density of impurity states $g_0(E_{Fn})$ and the fractional change in electron con-

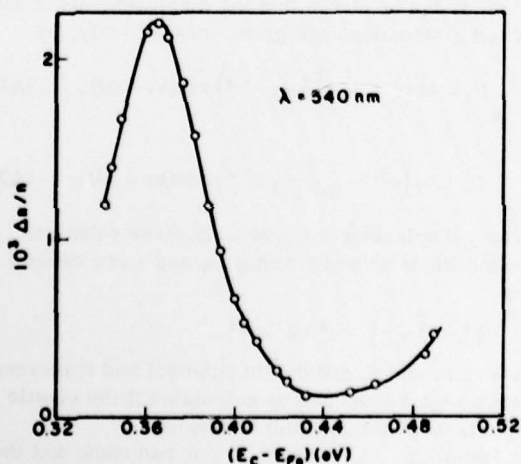


FIG. 11. $\Delta n/n$ as a function of $E_c - E_{Fn}$ for light of wavelength 540 nm.

centration due to strain $\Delta n/n$ were measured on two different films of CdS. Unfortunately, the technique of fabrication does not allow exact reproducibility of film characteristics between different films.

The coincidence of the extrema of $\Delta n/n$ with those of $g_0(E_{Fn})$ is the strongest confirmation we have observed of the theoretical model proposed by us. It indicates unambiguously the correlation between the modulation of conductivity by strain and the presence of impurity states in the forbidden gap. Furthermore, in the development of our model, we assumed that the elastic strain does not change the mobility of electrons, but modulates the concentration of free electrons. That the predictions based on this assumption are borne out by experiment tends to confirm the validity of the assumption.

Next, we will illustrate how the measurements of elastophotoconductance can be used to calculate the deformation potentials of impurity levels. For this purpose, it is more convenient to use the derivative of $\Delta n/n$ with respect to E_{Fn} rather than $\Delta n/n$ itself. This derivative is given in Eq. (2.26). We will rewrite this equation as follows

$$\Delta E(E_{Fn}) - \Delta E_c = kT \left[g_0(E_{Fn}) \left(\frac{dg_0}{dE_{Fn}} \right)^{-1} \frac{d}{dE_{Fn}} \left(\frac{\Delta n}{n} \right) + \frac{\Delta n}{n} \right]. \quad (5.3)$$

If we assume that the CdS crystallites in our films have the same deformation potentials as single crystals of CdS, then ΔE_c can be calculated since we know the magnitude of the strains generated. All other quantities in Eq. (5.3) can be determined from Figs. 6 and 8. Therefore, Eq. (5.3) can be used to determine $\Delta E(E_{Fn})$. However, at most values of E_{Fn} this is not possible with any degree of accuracy. To see this, we note that whenever dg_0/dE_{Fn} is positive, $(d/dE_{Fn})(\Delta n/n)$ is negative, and vice versa. Therefore, the first term in parentheses is always negative while the second term, $\Delta n/n$ is always positive. However, the magnitude of each term, for most values of E_{Fn} , is individually much larger than $(\Delta E - \Delta E_c)/kT$. Thus, Eq. (5.3) implies the calculation of a "small" number by taking the difference of two "large" numbers. Such a calculation is often inaccurate.

However, Eq. (5.3) can still be used for calculation of $\Delta E(E_{Fn})$ at those values of E_{Fn} where $(\Delta E - \Delta E_c)/kT$ is comparable to the magnitude of either term in the brackets on the right-hand side which is the case when $E_c - E_{Fn}$ is between 0.28 and 0.30 eV.

From Eq. (2.13) we have

$$E(E_{Fn}) = D_1(E_{Fn})\Sigma_{vi}^0 + D_2(E_{Fn})\Sigma_{ii}^0. \quad (5.4)$$

TABLE I. Values of deformation potentials $D_0(E_{Fn})$, calculated as described in the text.

$E_c - E_{Fn}$ (eV)	$g_0(E_c - E_{Fn})$ (arb. units)	$10^5 \left(\frac{\Delta n}{n} \right)$	$\frac{d}{dE_{Fn}} \left(\frac{\Delta n}{n} \right)$ (eV ⁻¹)	$D_0(E_{Fn})$ (eV) [from Eq. (5.8)]
0.284	2100	2.3	-1.700×10^{-3}	-9.93
0.288	1900	3.2	-2.579×10^{-3}	-12.88
0.294	1650	5.1	-3.563×10^{-3}	-13.36
0.298	1450	6.7	-4.651×10^{-3}	-13.89

Using Eq. (A10) we can write this

$$\begin{aligned} \Delta E(E_{Fn}) &= [D_1(E_{Fn}) - 0.22 D_2(E_{Fn})] \Sigma_{xx}^0 \\ &= D_0(E_{Fn}) \Sigma_{xx}^0, \end{aligned} \quad (5.5)$$

where

$$D_0(E_{Fn}) = D_1(E_{Fn}) - 0.22 D_2(E_{Fn}). \quad (5.6)$$

Using Langer's deformation potentials for CdS crystals and the strain components measured by us, we get

$$\Delta E_c = -3.5 \times 10^{-7} \text{ eV}. \quad (5.7)$$

Using this result along with Eq. (5.6) in Eq. (5.3) we can write,

$$\begin{aligned} D_0(E_{Fn}) &= -3.5 \times 10^{-7} \\ &+ \frac{kT}{\Sigma_{xx}^0} \left[g_0(E_{Fn}) \left(\frac{dg_0}{dE_{Fn}} \right)^{-1} \frac{d}{dE_{Fn}} \left(\frac{\Delta n}{n} \right) + \frac{\Delta n}{n} \right]. \end{aligned} \quad (5.8)$$

In both of these equations $D_0(E_{Fn})$ is in eV if kT is expressed in eV. We will use Eq. (5.8) to calculate $D_0(E_{Fn})$. The values of $\Delta n/n$ for $E_c - E_{Fn}$ between 0.28 and 0.30 eV are taken from Fig. 8. The slope of $g_0(E_{Fn})$, from Fig. 6, is almost constant in this region and given by

$$\frac{dg_0}{dE_{Fn}} = 4.35 \times 10^2 \text{ eV}^{-1}, \quad (5.8)$$

where $g_0(E_{Fn})$ is in arbitrary units.

Using all this data in Eq. (5.8) we have constructed Table I. We notice that the calculated values of $D_0(E_{Fn})$ are of the order of 10 eV. Moreover, as E_{Fn} approaches the conduction band, the deformation potential decreases in magnitude. It must do this since in the limit when E_{Fn} coincides with E_c , the deformation potentials must equal those of CdS crystals which are about 5 eV.

It is important to note that all our calculations and discussions in this section pertain to Fig. 8 in which we reported the variation of $\Delta n/n$ with white light intensity. Similar measurements with monochromatic light at different frequencies are shown in Figs. 9-11. They clearly have extrema

very close to those obtained with white light. However, only the measurements with white light were chosen for calculations since we were able to generate high enough intensities to explore a wide range of values of $E_c - E_{Fn}$. This was not possible with monochromatic light.

We have shown that the qualitative features predicted by our model are well borne out by our experiments. We feel that the theoretical model proposed by us can, in fact, be used for a study of the properties of deep impurities in semiconductors.

ACKNOWLEDGMENTS

This research was supported in part by the U.S. Army Night Vision Laboratory. Some of the preliminary work was supported by the NSF. This work is based in part on a thesis submitted by one of us (A.M.) to Syracuse University in partial fulfillment of the requirements for the Ph.D. degree.

APPENDIX A: STRAINS GENERATED BY RAYLEIGH WAVES

For a Rayleigh wave propagating the x direction and decaying exponentially in the positive z direction, it can be shown that the displacements in the x and z directions are given, respectively, by

$$U_x = Ak \left(e^{-qs} - \frac{2qs}{k^2 + s^2} e^{-ks} \right) \sin(kx - \omega t), \quad (A1)$$

$$U_z = Aq \left(e^{-qs} - \frac{2k^2}{k^2 + s^2} e^{-ks} \right) \cos(kx - \omega t). \quad (A2)$$

The y displacement is zero. In these equations, k is the Rayleigh wave vector; q and s are defined by

$$q^2 = k^2 - k_t^2, \quad s^2 = k^2 - k_l^2,$$

where k_l and k_t are the longitudinal and transverse wave vectors and can be calculated if the elastic constants of the medium are known.

From Eqs. (A.1) and (A.2) one can show that the amplitude of the strain components at the surface

($z=0$) are given by

$$\Sigma_{xx}^0 = \frac{Ak^2}{k^2 + s^2} (k^2 + s^2 - 2qs), \quad (A3)$$

$$\Sigma_{xx}^0 = \frac{Aq}{k^2 + s^2} (2k^2s - k^2q), \quad (A4)$$

$$\Sigma_{xx}^0 = 0. \quad (A5)$$

In terms of the amplitude of x displacement at the surface, u_0 , these can be written

$$\Sigma_{xx}^0 = \frac{k^2(k^2 + s^2 - 2qs)}{q(s^2 - k^2)} U_0, \quad (A6)$$

$$\Sigma_{xx}^0 = \frac{2k^2s - k^2q - s^2q}{s^2 - k^2} U_0. \quad (A7)$$

Therefore Σ_{xx}^0 can be expressed as

$$\Sigma_{xx}^0 = C \Sigma_{xx}^0, \quad (A8)$$

where

$$C = q(2k^2s - k^2q - s^2q)/k^2(k^2 + s^2 - 2qs). \quad (A9)$$

Using the elastic constants of soda-lime glass and the fact that our experiments were all done at 2.21 MHz, one can show that

$$C = -0.22,$$

so that

$$\Sigma_{xx}^0 = -0.22 \Sigma_{xx}^0. \quad (A10)$$

APPENDIX B: DERIVATION OF FORMULA FOR ELASTOPHOTOCONDUCTANCE SIGNALS

Figure 12 is an exploded view of the indium contact pattern laid down on the CdS film. Since the drift voltage and measured currents are along the y axis, we are interested in the σ_{yy} component of the conductivity. From Eq. (2.2) this component is

$$\sigma_{yy}(x) = P_{yy}(I) + [M(I)\Sigma]_{yy}. \quad (2.2')$$

Using Eq. (2.4), this reduces to

$$\sigma_{yy}(x) = P_{yy}(I) + M_0 \Sigma_{xx}. \quad (B.1)$$

Consider first in Fig. 12 the CdS strip between $y=0$ and $y=b$. Consider an element of this strip of width dx . If the film thickness is h , using Eq. (B.1) the current from this element can be written

$$di = (hV/b) [P_{yy}(I) + M_0(I)\Sigma_{xx}] dx, \quad (B.2)$$

where V is the voltage applied to the fingers. Let us assume the projected intensity pattern I has no variation along the y axis. Then, all the strips of CdS will make the same contribution to the current. If the total number of strips is R , the total current from the contact pattern is

$$i = \frac{RVh}{b} \int_{x=0}^a [P_{yy}(I) + M_0(I)\Sigma_{xx}] dx \\ = i_{dc} + i_{ac}, \quad (B.3)$$

where

$$i_{dc} = \frac{RVh}{b} \int_{x=0}^a P_{yy}(I) dx, \quad (B.4)$$

$$i_{ac} = \frac{RVh}{b} \int_{x=0}^a M_0(I)\Sigma_{xx} dx. \quad (B.5)$$

If the strain is a sinusoidal traveling wave along the positive x axis, we can write

$$\Sigma_{xx} = \Sigma_{xx}^0 e^{i(kx - \omega t)},$$

where Σ_{xx}^0 is the amplitude of the strain. Therefore

$$i_{ac} = \frac{RVh}{b} \Sigma_{xx}^0 \int_{x=0}^a M_0(I) e^{i(kx - \omega t)} dx. \quad (B.6)$$

It is clear from Eq. (B.4) that i_{dc} is just the photo-current through the film without strain. Now, using Eq. (B.4) we can eliminate V from Eq. (B.6) to obtain

$$i_{ac} = i_{dc} \Sigma_{xx}^0 \int_{x=0}^a M_0(I) e^{i(kx - \omega t)} dx / \int_{x=0}^a P_{yy}(I) dx. \quad (B.7)$$

This form of the equation is convenient since the amplifier used maintained a constant dc current through the film. Thus, i_{dc} in Eq. (B.7) is constant.

Now let us evaluate the integrals in Eq. (B.7) for a specific intensity pattern, namely, the periodic intensity function shown in Fig. 13. We will calculate the signal for such a pattern at its fundamental

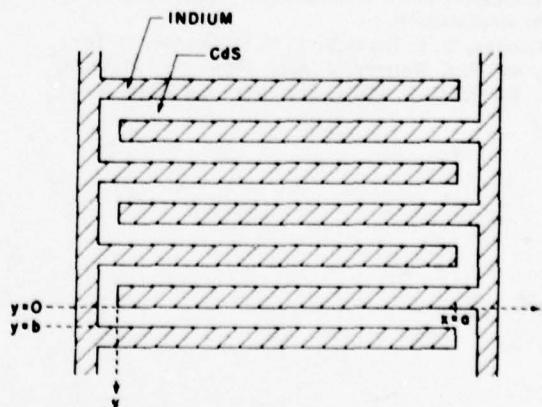


FIG. 12. Section of indium contact pattern evaporated on CdS film.

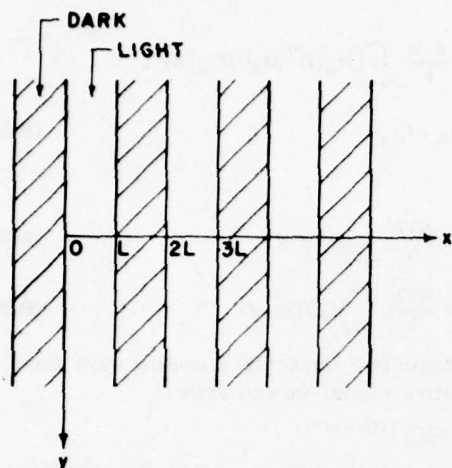


FIG. 13. Section of light pattern projected on the CdS film.

Fourier frequency, i.e., when

$$\lambda = 2L \text{ or } Lk = \pi. \quad (\text{B.8})$$

In this case the integral

$$\int_{x=0}^a M_0(I) e^{i(kx - \omega t)} dx$$

obtains contributions from all the light strips and all such contributions are in phase. The dark portions contribute practically nothing since $M_0(I)$ is zero for zero light flux. If there are N light strips in the length a ,

$$\begin{aligned} \int_{x=0}^a M_0(I) e^{i(kx - \omega t)} dx &= M_0(I_0) N \int_{x=0}^L e^{i(kx - \omega t)} dx \\ &= M_0(I_0) N \frac{2L}{\pi} e^{i(\pi/2 - \omega t)} \end{aligned} \quad (\text{B.9})$$

through Eq. (B.8). Also,

$$\begin{aligned} \int_{x=0}^a P_{yy}(I) dx &= NP_{yy}(I_0) \int_0^L dx \\ &= NP_{yy}(I_0) L. \end{aligned} \quad (\text{B.10})$$

Substituting Eq. (B.9) and (B.10) in Eq. (B.7) gives

$$i_{ac} = i_{dc} \sum_{xx}^0 \frac{M_0(I_0)}{P_{yy}(I_0)} \frac{2}{\pi} e^{i(\pi/2 - \omega t)}. \quad (\text{B.11})$$

Or, in terms of amplitude, the ac component of the photocurrent at the frequency defined by Eq. (B.8) is

$$(i_{ac})_{\text{amplitude}} = \frac{2}{\pi} i_{dc} \frac{M_0(I_0)}{P_{yy}(I_0)} \sum_{xx}^0. \quad (\text{B.12})$$

¹D. Langer, *Proceedings of the International Conference on Semiconductor Physics, Prague, 1960* (Academic New York, 1961).

²K. W. Boer, E. Gutsche, and E. Jahne, *Phys. Status Solidi* **3**, 922 (1963).

³C. S. Smith, in *Solid State Physics*, edited by F. Seitz and D. Turnbull (Academic, New York, 1958), Vol. 6.

⁴J. Dresner and F. V. Shallcross, *J. Appl. Phys.* **34**, 2390 (1963).

⁵A. Mahapatra, Ph.D. dissertation (Syracuse University, 1977) (unpublished).

⁶A. Waxman, V. E. Henrich, F. V. Shallcross, H. Borikan, and P. K. Weimer, *J. Appl. Phys.* **36**, 168 (1965).

⁷G. L. Bir and G. E. Pikus, *Symmetry and Strain In-*

duced Effects in Semiconductors (Halsted, New York, 1974).

⁸D. W. Langer, R. N. Euwema, Koh Era, and Takao Koda, *Phys. Rev. B* **2**, 4005 (1970).

⁹See, for example, A. Rose, *Concepts in Photoconductivity and Allied Problems* (Interscience, New York, 1963).

¹⁰K. W. Boer, A. S. Esbitt, and W. M. Kaufman, *J. Appl. Phys.* **37**, 2664 (1966).

¹¹N. F. Foster, *IEEE Proc.* **53**, 1400 (1965).

¹²J. Dresner and F. V. Shallcross, *J. Appl. Phys.* **34**, 2390 (1963).

¹³W. W. Piper and R. E. Halsted, in Ref. 1.

APPENDIX V.

SPURIOUS ACOUSTIC MODES IN TWO-DIMENSIONAL
FOURIER TRANSFORM DEVICES

IEEE Transactions on Sonics and Ultrasonics,
Vol. SU-25, No. 6 November 1978

Spurious Acoustic Modes in Two-Dimensional Fourier Transform Devices

AMARESH MAHAPATRA, STEPHEN T. KOWEL, SENIOR MEMBER, IEEE, PHILIPP G. KORNEICH, MEMBER, IEEE, AND MOOSA MEHTER

Abstract—Experiments conducted on two-dimensional Fourier transform sensors using CdS films on z-cut LiNbO₃ show evidence for the presence of more than one acoustic velocity in the substrate. Pulsed experiments conducted with two transducers and detailed measurements of transducer frequency response confirm the presence of these additional modes. As a result, the Fourier transform of any image repeats itself in frequency space, the number of repetitions depending on the number of additional acoustic modes. The detrimental effects of these spurious modes can be eliminated entirely by suitable sampling of the image projected on the sensor.

I. INTRODUCTION

FOR SOME time now we have been working on fabrication of devices which generate two-dimensional Fourier transforms of optical images. The devices use CdS films on LiNbO₃ as sensors. Interdigital transducers are used to generate SAW's in the LiNbO₃. Signals proportional to the Fourier transform of projected optical images result from a nonlinear electric field interaction in the CdS film.

Recently, we have found evidence for the existence of more than one acoustic mode in our monolithic layered structures. In this paper we present evidence for the presence of such modes and show how they can be attenuated by suitable treatment of the bottom surface of the substrate. More interestingly, we show that their detrimental effects can be entirely eliminated by suitable design of transducers and sampling of the optical image.

II. ELECTROPHOTOCONDUCTIVE SENSORS—BRIEF DESCRIPTION

We give here a brief description of our two-dimensional direct electronic Fourier transform (DEFT) devices. Such a description is essential to an understanding of spurious acoustic modes which will follow in later sections.

The direct electronic Fourier transform device which is illustrated in Fig. 1 consists essentially of a thin photoconducting film of CdS layed down on a z-cut LiNbO₃ substrate. Interdigital transducers are fabricated along the sides of the CdS film to allow the generation of surface acoustic waves in the

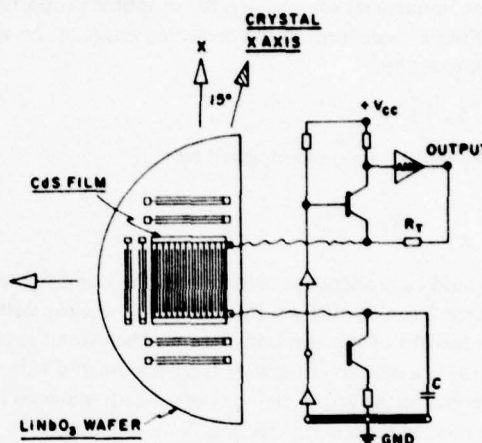


Fig. 1. Two-dimensional Fourier transform sensor (DEFT).

LiNbO₃ substrate. The transducers used by us have a center frequency of 30 MHz and a bandwidth of 20%. As a result of the SAW's, the CdS film is subject to the electric fields associated with these waves. It has been demonstrated that the photoconductivity of CdS films is strongly modulated by the application of external electric fields, with the photocurrent having a component proportional to the square of the electric field. Thus the electric fields associated with the SAW's modulate the photoconductivity of the CdS film. Indeed, if an optical image characterized by the intensity function $I(x, y)$ is projected on the CdS film, a full tensor treatment of the above phenomenon reveals that the deposited contacts detect a current

$$i(t) \propto \iint dx dy E_z^2(x, y, t) I(x, y), \quad (1)$$

where x and y are the coordinates on the film, and E_z is the total electric field perpendicular to the plane of the film.

Now,

$$E_z = E_1 \cos(\omega_1 t - k_1 x) + E_2 \cos(\omega_2 t + k_2 y), \quad (2)$$

where E_1 , ω_1 , and k_1 refer to the x -directed acoustic wave and E_2 , ω_2 , and k_2 refer to the y -directed acoustic wave. (In the rest of the paper subscripts 1 and 2 will refer to the x and y axis, respectively.) Clearly, E_z^2 contains a term of the form

$$\begin{aligned} E_z^2 &\propto E_1 E_2 \cos[(\omega_1 - \omega_2)t - (k_1 x + k_2 y)] \\ &= E_1 E_2 \cos[(\omega_1 - \omega_2)t - \vec{k} \cdot \vec{r}]. \end{aligned} \quad (3)$$

Manuscript received July 3, 1978. This work was supported by the U.S. Army Night Vision and Electrooptics Laboratory.

A. Mahapatra, S. T. Kowel, and P. G. Kornreich are with the Department of Electrical and Computer Engineering, Syracuse University, Syracuse, NY 13210.

M. Mehter was with the Department of Electrical and Computer Engineering, Syracuse University, Syracuse, NY 13210. He is now with the Noise Technology Section, Boeing Company, Seattle, WA.

Using this in (1), it is easy to see that $i(t)$ has a term of the form

$$i(t) \propto \exp [j(\omega_1 - \omega_2)t] \int d^2\vec{r} I(\vec{r}) \exp (-j\vec{k} \cdot \vec{r}), \quad (4)$$

while the other terms from (2) can be ignored because they are at different frequencies.

It is clear from (3) that if the two transducers T_1 and T_2 are driven at frequencies ω_1 and ω_2 , the output is proportional to the Fourier transform of the projected image at the wave vector \vec{k} given by

$$\vec{k} = \hat{i}k_1 + \hat{j}k_2, \quad (5)$$

where k_1 and k_2 are, in turn, given by

$$k_1 = \frac{\omega_1}{v_1}, \quad k_2 = \frac{\omega_2}{v_2}. \quad (6)$$

Here v_1 and v_2 are acoustic velocities in the x and y direction. The vector \vec{k} can be changed by varying ω_1 and ω_2 within the bandwidths of the two transducers. Therefore the signal behaves as if a new acoustic wave has been created with wave vector equal to the vector sum of the acoustic wave vectors. We call this "pseudo beam steering."

Now, the optical image will have Fourier transforms at base band ($\vec{k} = 0$) while the transducers will probe the region of Fourier space centered around the wave-vector $\vec{k} = \hat{i}k_{10} + \hat{j}k_{20}$, where k_{10} and k_{20} are determined by substituting the transducer center frequencies into (6). This problem is eliminated by sampling the image with a grid with periodicity corresponding to k_{10} and k_{20} in the x and y directions. This will effectively shift the Fourier transform of the image from baseband to the region of Fourier space probed by the transducers.

In one direction the interdigital contact pattern layed down to detect the signal is itself effective in sampling the image. In the other direction we achieve sampling either by etching the CdS into strips, or by projecting the image through a grid. In our experiments the sampling periodicities in the x and y direction were equal (k_g) since the acoustic velocities in the two directions are almost equal.

Now, suppose we illuminate the CdS with uniform light intensity. The Fourier transform of such a pattern is a sinc function (the spread being determined by the aperture) centered around $\vec{k} = 0$. However, since the light is sampled, the same sinc function will now appear centered around $\vec{k} = \vec{k}_0$.

These details are given here since they will be referred to in the next section in connection with the existence of spurious acoustic modes. For a complete description of the device fabrication and operation the reader is referred to [1]–[3].

III. EXPERIMENTAL RESULTS

The first experimental evidence for the existence of more than one acoustic velocity in our substrates appeared in our tests with uniform light intensity on the CdS. The experiment was done by driving the y -directed transducer (T_2) at a fixed frequency ω_2 , and sweeping the x -directed transducer (T_1) through its full bandwidth, i.e., from 25 MHz to 35 MHz. We had expected a finite output only when k_1 and k_2 were both

equal to k_g , i.e., when

$$\frac{\omega_1}{v_1} = \frac{\omega_2}{v_2} = k_g. \quad (7)$$

The frequency ω_2 was adjusted to satisfy the second equality in (7).

It was found that difference frequency signals appeared at two different values of ω_1 , namely at $\omega_1 = 29.622$ MHz and $\omega_1 = 29.168$ MHz. This was a clear indication of two separate acoustic velocities in the x direction v_{11} and v_{12} , which when combined with the two values of ω_1 individually satisfied the equality $\omega_1/v_1 = k_g$. Henceforth we use the convention that the first subscript specifies the axis while the second subscript specifies the acoustic mode corresponding to that axis.

Clearly, there was no *a priori* reason to assume that two velocities v_{21} and v_{22} did not exist in the y -direction also. With a set of four acoustic velocities, two along each axis, it is easy to deduce from (7) that, with uniform light, one would expect to see different frequencies signals at four combinations of ω_1 and ω_2 values. These combinations would be

$$(\omega_{11}, \omega_{21}), \quad (\omega_{12}, \omega_{21}), \quad (\omega_{11}, \omega_{22}), \\ \text{and } (\omega_{12}, \omega_{22}),$$

where ω_{11} , ω_{12} , ω_{21} , and ω_{22} are given by

$$\frac{\omega_{11}}{v_{11}} = \frac{\omega_{12}}{v_{12}} = \frac{\omega_{21}}{v_{21}} = \frac{\omega_{22}}{v_{22}} = k_g. \quad (8)$$

Indeed, by careful scanning of the frequency space spanned by ω_1 and ω_2 , we did observe four signals. With the use of (8) we were able to calculate the ratio of the two velocities along each axis. In fact,

$$\frac{v_{12}}{v_{11}} = 1.066 \quad \frac{v_{22}}{v_{21}} = 1.137. \quad (9)$$

From (9) we notice that the two velocities in the x -direction differ by about 7%.

A. Pulsed Experiments With No CdS Layer on the LiNbO₃.

To confirm the existence of two acoustic velocities along each propagation direction, we decided to conduct pulsed acoustic experiments with two x -directed 30-MHz transducers fabricated on z -cut LiNbO₃. The experiments were done both with and without CdS layers evaporated on the LiNbO₃.

Fig. 2 shows a typical input and output pulse for the case with no CdS layer on the LiNbO₃. We noticed that though the input is a rectangular pulse, the output has ramped leading and lagging edges. This is a common feature and arises from the fact that the maximum voltage at the output develops only after the acoustic wave has traveled from the left most finger of the input transducer to the right most finger of the output transducer. By measuring the delay time we calculate the acoustic velocity to be 3846m/sec. (insertion loss = -26 dB).

The two upper traces of Fig. 2 show the result of reducing the input pulse width to about 0.1 μ sec. The output continues to show a single continuous pulse. Thus there was no evidence for the existence of spurious acoustic modes.

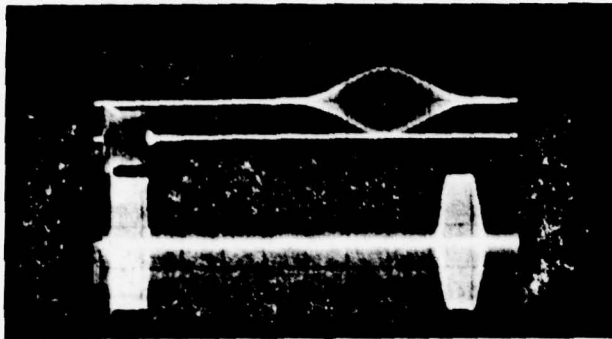


Fig. 2. Pulsed experiment without CdS layer on LiNbO₃. Lowest trace shows input and output pulses—horizontal scale 1 μ s/div; vertical scale 0.2V/div for input pulse and 0.01V/div for output pulse. Middle trace shows input pulse reduced in width—horizontal scale 0.1 μ s/div; vertical scale 0.5V/div. Uppermost trace shows output corresponding to middle trace—horizontal scale 0.1 μ s/div; vertical scale 0.01V/div.

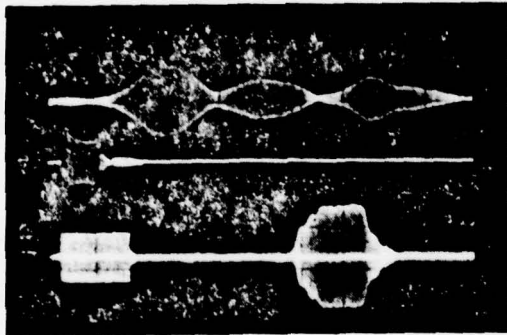


Fig. 3. Pulsed experiment with CdS layer on LiNbO₃. Lowest trace shows input and output pulses—horizontal scale 1 μ s/div; vertical scale 0.5V/div. for input pulse and 0.02V/div. for output pulse. Middle trace shows input pulse reduced in width—horizontal scale 0.1 μ s/div; vertical scale 0.5V/div. Uppermost trace shows output corresponding to middle trace—horizontal scale 0.1 μ s/div; vertical scale 0.01V/div.

B. Pulsed Experiments With CdS Layer on the LiNbO₃ Between the Transducers

Experiments similar to those described in (A) were also conducted with CdS layers evaporated on the LiNbO₃. Fig. 3 shows the results of these experiments. We notice that the output now not only has ramped edges but also seems to build up and die out in stages. In fact, there are three distinct steps in either edge. Such a behavior would develop if there were three different acoustic velocities being propagated in the substrate so that waves of different velocity would reach the output transducer after different delays. By measuring the smallest delay and the delay corresponding to the setting in of each step, we calculate the three acoustic velocities to be

$$v = 3592 \text{ m/sec}, \quad 3762 \text{ m/sec}, \quad \text{and} \quad 3964 \text{ m/sec}.$$

The two upper traces of Fig. 3 show the effect of reducing the input pulse width to 0.1 μ sec. Notice that the output develops three distinct pulses. This is to be expected since if the input pulse is narrow enough and if the transducer separation is large enough, acoustic pulses at the three velocities will become distinct from each other. Indeed this result most graphi-

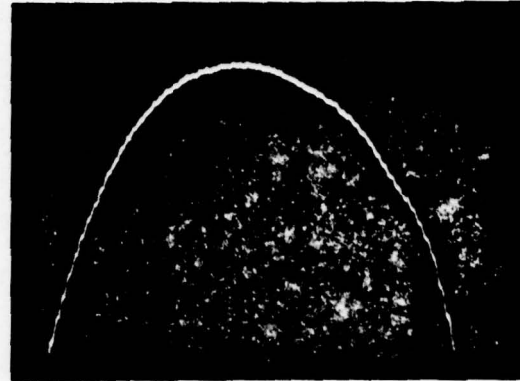


Fig. 4. Frequency response without CdS on LiNbO₃. 2.5 dB/div. Frequency scanned 26–34 MHz.

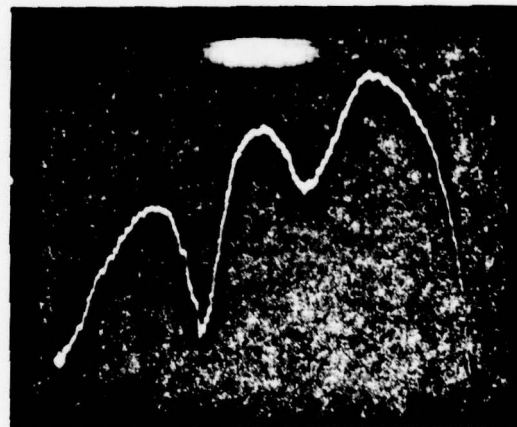


Fig. 5. Frequency response with CdS, on LiNbO₃ 2.5 dB/div. Frequency scanned 27.6–34 MHz.

cally illustrates the presence of more than one acoustic velocity.

C. Frequency Response of Transducers

If there were a unique acoustic velocity v , the frequency response of an interdigital transducer would be bell-shaped and centered around a frequency determined by

$$f = \frac{v}{a},$$

where a is the transducer periodicity. However, if there are three acoustic velocities, the same transducer would have three bell-shaped curves in its frequency response with center frequencies determined by v_1/a , v_2/a , and v_3/a . At any given frequency, of course, all three modes are present (because of the transducer bandwidth) and there is a possibility of interference between them.

Fig. 4 and Fig. 5 show the frequency response of our transducers without CdS layers and with CdS layers on the LiNbO₃. Three peaks appear in Fig. 5 as predicted. The three peak frequencies yield the following ratios:

$$\frac{v_2}{v_1} = 1.056, \quad \frac{v_3}{v_1} = 1.112.$$

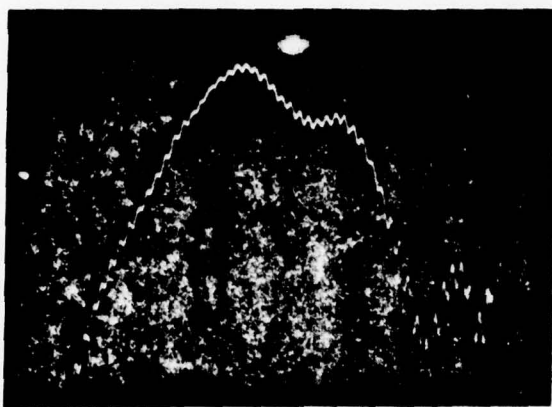


Fig. 6. Frequency response with CdS, but with acoustic absorbing tape stuck to bottom surface 2.5 dB/div. Ripples are due to slight electromagnetic feedthrough from input to output.

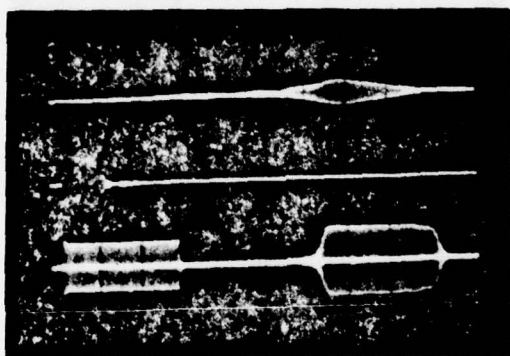


Fig. 7. Pulsed experiments with CdS and acoustic absorbing tape. Lowest trace shows input and output pulses—horizontal scale 1 μ s/div.; vertical scale 0.5V/div. for input pulse and 0.02V/div. for output pulse. Middle trace shows input reduced in width—horizontal scale 0.1 μ s/div.; vertical scale 0.5V/div. Uppermost trace shows output corresponding to middle trace—horizontal trace 0.1 μ s/div.; vertical scale 0.01V/div.

The first ratio indicates the velocity difference between the first and second mode to be about 6%, which agrees well with the result of pulsed experiments.

Finally, we have found that treatment of the bottom surface of the LiNbO_3 results in considerable improvement in acoustic performance. The result of sticking absorbing tape to the bottom surface is shown in Fig. 6 and Fig. 7. It is clear that the frequency response is much smoother. In the pulsed experiments we notice that the output very closely resembles the output with no CdS on the LiNbO_3 (Fig. 2). This result seems to indicate that the spurious acoustic modes observed by us are bulk plate modes. However, we have also found that the fundamental mode and the spurious modes are considerably suppressed by liquids sprayed on the top surface. The implications of these diverse results are discussed in the next section.

IV. ORIGIN OF SPURIOUS WAVES

The subject of spurious surface wave generation in layered SAW devices has received considerable attention in the literature. It has been shown by Farnell and Adler [4], that the presence of layers on isotropic or piezoelectric substrates will

result, not only in dispersive surface waves, but will generate more than one Rayleigh mode. All but the first Rayleigh mode (which corresponds to the Rayleigh mode in the absence of a layer) will have low-frequency cutoffs which depend on the layer thickness.

In our devices, we are hesitant to assume that the observed modes are surface acoustic waves, since our LiNbO_3 substrates are only four wavelengths thick. At the same time, the additional acoustic modes appear only when CdS layers are evaporated onto the LiNbO_3 substrates. This indicates that they might be related to the additional Rayleigh modes on layered structures predicted by Farnell and Adler [4]. It is true that in most instances dealt with in the literature, the second Rayleigh mode has a low-frequency cutoff at $kh \approx 0.5$, where k is the magnitude of the wave vector and h is the layer thickness. In our case, at 30 MHz and a layer thickness of 2–4 microns, kh is at most 0.23. Moreover, the difference in velocity between the first two Rayleigh modes close to the cutoff is usually much larger than the 6% difference observed by us.

However, Farnell and Adler [4] also discuss in detail the relation of Rayleigh-type modes to plate modes [6]. Indeed they show that for layered structures on thin substrates there are two modes with no low-frequency cutoffs. These modes have displacement profiles that do not go to zero at either the free surface of the layer or the bottom surface of the substrate. It would be possible to attenuate such waves by treatment of either of these surfaces. The substrates we use are only about four wavelengths thick, and it is conceivable that we are generating plate modes, more strongly so in the presence of the CdS layers.

V. DEVICE DESIGN IN THE PRESENCE OF SPURIOUS WAVES

It is clear that the presence of spurious velocities is detrimental to the operation of our two-dimensional Fourier transform devices. For instance, with uniform light on the sensor, one obtains four instead of one peak in frequency space. These peaks, which we call dc peaks, are illustrated in Fig. 8.

Now, if any picture is projected on the sensor, its Fourier transform appears centered not only about the main dc peak (i.e., the one at f_{x0}, f_{y0}) but also about the other three dc peaks. This leads to considerable overlapping of peaks and difficulty in analysis of signals. In this section, we use f to denote the temporal frequency corresponding to the radian frequency ω used in earlier sections.

This problem can be avoided by sampling the picture such that the main dc peak is located not at the center of the scanned frequency space but the line AB of Fig. 8. Moreover, it would be convenient to design the transducers such that the $f_x = f_y$ line did not pass through the scanned frequency space. Signals on this line correspond to zero-difference frequency and cannot be easily amplified. The situation would then be as depicted in Fig. 9. The main dc peak is now located at $(f_{x0}, f_{y0} + \Delta f_y/2)$. There is one spurious dc peak to the right of the main dc peak which may produce some undesirable effects. But the other two spurious dc peaks are outside the scanned frequency space. It is true that this design permits

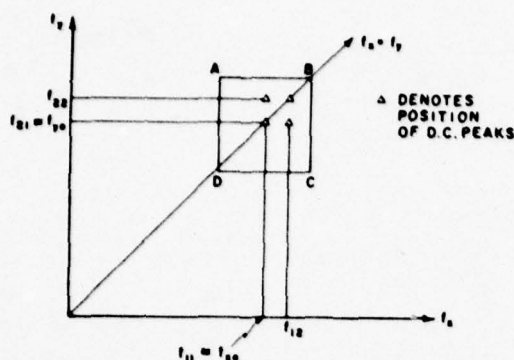


Fig. 8. Location of dc peaks with uniform illumination. ABCD denotes roughly region of frequency space scanned by transducers. Center frequencies of transducers, f_{x0} and f_{y0} , are almost equal. Peak at (f_{x0}, f_{y0}) is main dc peak. In addition, there are three other dc peaks in the scanned frequency space.

scanning of only one half of Fourier space. However, for a real function $I(\vec{r})$ (which all intensity distributions are), the Fourier transform $F(\vec{k})$ and its complex conjugate $F^*(\vec{k})$ satisfy

$$F(-\vec{k}) = F^*(\vec{k})$$

so that the information in one half of Fourier space is sufficient.

We are now in the process of fabricating a device with the design of Fig. 9.

ACKNOWLEDGMENT

We would like to thank Mr. David Helm, the project monitor. One of the authors (A. Mahapatra) would like to thank Dr. K. W. Loh for helpful discussions.

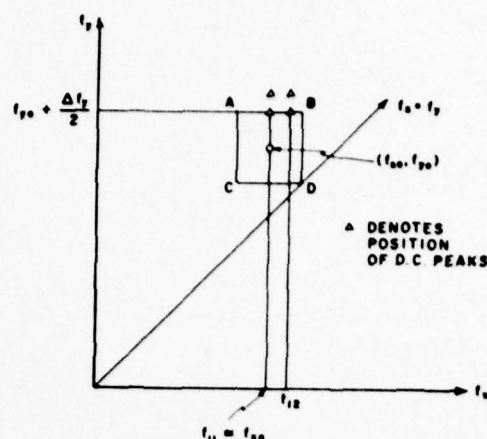


Fig. 9. Improved device design to eliminate spurious dc peaks. Transducers are designed with unequal center frequencies. Peak at $(f_{x0}, f_{y0} + \Delta f_y/2)$ is dc peak and is close to periphery of scanned frequency space. There is only one other dc peak located within ABCD.

REFERENCES

- [1] "Imaging Without Spatial Raster Scanning," S. T. Kowel, P. G. Kornreich, K. W. Loh, A. Mahapatra, and M. Mehter, *IEEE Trans. on Electron Devices* (to be published).
- [2] "The Vector Imaging Convolver," S. T. Kowel, P. G. Kornreich, A. Mahapatra, B. Emmer, M. Mehter, and P. Reck, *1977 Ultrasonics Symposium Proceedings*, p. 715.
- [3] "Two-Dimensional Direct Electronic Fourier Transform Devices (DEFT): Analysis, Fabrication, and Evaluation," S. T. Kowel *et al.*, TR-77-5, Dept. of Electrical Engr., Syracuse University, Syracuse NY 13210.
- [4] "Elastic Wave Propagation in Thin Layers," G. W. Farnell and E. L. Adler, *Physical Acoustics*, Eds. Mason and Thurston, Academic Press.
- [5] "A Review of Propagation and Electroacoustic Coupling in Layered Structures," G. W. Farnell, *1977 Ultrasonics Symposium Proceedings*, p. 803.
- [6] "Plate Mode Coupling in Acoustic Surface Wave Devices," R. S. Wagers, *IEEE Trans. Sonics Ultrasonics*, vol. SU 23, no. 2, Mar. 1976.

APPENDIX VI.

MONOLITHIC TWO-DIMENSIONAL FOURIER TRANSFORMER

1978 International Optical Computing Conference
London, England

1978 INTERNATIONAL OPTICAL COMPUTING CONFERENCE
London, England

MONOLITHIC TWO-DIMENSIONAL FOURIER TRANSFORMER

P.G. Kornreich, S.T. Kowel, A. Mahapatra, and M. Mehter*

Department of Electrical and Computer Engineering, Syracuse University, Syracuse, New York 13210

Abstract

We have fabricated acoustooptical sensors capable of two-dimensional image processing. They exploit the non-linear modulation of the photoconductivity of a CdS film by an electric field component normal to the plane of the device. The electric field is associated with two orthogonal traveling surface acoustic waves in the LiNbO_3 substrate. The total photocurrent on the device surface is detected. With sinusoidal voltages applied to the transducers, we obtain a difference frequency signal proportional to the Fourier transform of the image focused on the device. It is necessary to optically sample the image in order to shift its Fourier transform to the region of Fourier space probed by the acoustic waves. This sampling is achieved by a monolithic sampling grid integral with the device.

pattern permits the collection of the total photocurrent over the area of the CdS film. Indium is used as the contact material. It is our experience that it makes ohmic contact to CdS and aluminum provides better longitudinal conduction. Two interdigital transducers, each parallel to one of two orthogonal edges of the square sensor, are used for the generation of surface acoustic waves. The sensor area is overlaid by a thin polymer insulating film after the contacts are fabricated. An array of aluminum film squares deposited on the polymer film form a monolithic shadow mask. This shadow mask provides the sampling of the image in the x-direction. The image is sampled in the y-direction by the interdigital contact pattern.

Our previous devices had an externally mounted shadow mask [3,5]. Since the mask was spaced about 50 μm from the device, imaging with a lens was difficult. The light rays incident at an angle other than 90° to the plane of the device would undercut the shadow mask.

The present monolithic device eliminates this difficulty.

1. Introduction

We have succeeded recently in fabricating monolithic direct electronic Fourier transform (DEFT) imaging sensors. We here present the results of tests conducted with those devices. We also present contrast and Fourier space raster scan data previously not reported. In previous publications [1,2,3,4,5] we have reported data taken with devices having an externally mounted sampling grid, rather than the present monolithic sampling mask.

A DEFT device is an electronic image sensor. The output of the device is a sinusoidal electrical current. The amplitude of the current is proportional to the amplitude of the Fourier transform components of the two-dimensional image, and the phase of the current is proportional to the phase of the Fourier transform components of the image.

One embodiment of the device is shown in Fig. 1. The image sensor consists of a double layered CdS film [6] deposited on a z-cut LiNbO_3 substrate. The metal contacts, consisting of an Al/In film sandwich in the form of an interdigital pattern, are deposited onto the CdS film. This

2. Device Operation

The DEFT device derives an electrical signal representative of Fourier components by modulating the photo-generated electrons with electric fields associated with the traveling surface acoustic waves in the LiNbO_3 substrate. This modulation, as demonstrated by M. Luukkala [7], E.S. Kohn [8], and by us [1,9] is proportional to the square of the SAW electric field E . We here present a simplified calculation of the device output signal current i_{sig} . A detailed description of the tensor nature of the electrophotoconductivity is given elsewhere [1,4]. There we have shown that the sheet conductivity σ of a CdS film subject to illumination with a light intensity I and an electric field with a component E_1 normal to the plane of the film is

$$\sigma = \sigma_L I + \sigma_{LE} E_1^2 I \quad (2.1)$$

where σ_L is the ordinary scalar photoconductivity and σ_{LE} is the appropriate linear combination of elements of the electrophotoconductivity tensor.

The dark conductivity, that is the conductivity in the absence of light, is very small and

* Work supported by U.S. Army Night Vision & Electrooptics Laboratory, Ft. Belvoir, VA.

is neglected.

The interdigital contact pattern, in conjunction with the aluminum shadow mask divide the CdS film into an array of squares of photoconductive material. Thus the contact pattern also serves as part of a sampling grid that translates the image onto a high spacial carrier frequency. This, as will become evident, is necessary since the transducers have a limited bandwidth centered at a high temporal frequency.

The normal component E_z of the electric field associated with the two acoustic waves traveling at right angles to each other is

$$E_z = E_x \cos(\omega_x t - k_x x) + E_y \cos(\omega_y t + k_y y) \quad (2.2)$$

where ω_x , k_x and E_x are the temporal and spacial angular frequencies, and the normal component of the electric field associated with the SAW propagating in the x-direction, and ω_y , k_y and E_y are similar quantities associated with the y-propagating acoustic wave.

Consider a square of CdS film at the m, n position. We assume that the conductance g_{mn} of the mn 'th CdS square can also be expressed by an equation similar to equation 2.1. That is, we neglect all variations within each CdS square. This is justified since these variations will at most result in a slowly varying function of the spacial frequencies in the area of transform space considered. The conductance g_{mn} of the mn 'th CdS square is

$$g_{mn} = g_L I_{mn} + g_{LE} E_z^2 I_{mn} \quad (2.3)$$

where I_{mn} is the average light intensity incident on the mn 'th square of photoconducting material, g_L is the ordinary photoconductance, g_{LE} is the electrophotoconductance of a square of CdS film, and E_z is the SAW electric field component normal to the plane of the film.

The photocurrent i_{mn} in the mn CdS square due to a d.c. voltage V_0 applied across the contacts is

$$i_{mn} = g_{mn} V_0 \quad (2.4)$$

As we have noted, the conductance modulating electric field component E_z associated with the acoustic waves is in the form of two orthogonally traveling waves, equation 2.2. The modulation of the photoconductance, as expressed by equation 2.3, is proportional to the square of this field component. Therefore the photocurrent i_{mn} will contain components oscillating at various frequencies. The photocurrent component oscillating with the difference frequency $\omega_x - \omega_y$ is also a sinusoidal function of the vector sum of the wave vectors k_x and k_y , of the individual surface acoustic waves

$$\vec{k} = k_x \hat{x} + k_y \hat{y}. \quad (2.5)$$

We have thus created a conductivity "wave" propagating with a wave vector \vec{k} which is the vectorial sum of the original SAW wave vectors. The SAW wave vectors k_i are related to the angular frequency ω_i of the transducer driving voltages

by a linear dispersion relation

$$k_i = \omega_i / v_s \quad i = x, y \quad (2.6)$$

where v_s is the surface wave velocity under the CdS film, 3759 m/sec in our case. By controlling the frequencies of the transducer driving voltages we can "steer" the conductivity wave.

The circuit that detects the output current of the device is arranged, therefore, to detect only signals oscillating at the difference frequency $\omega_x - \omega_y$. Thus, we are only interested in the current component i_{sig} oscillating at the difference frequency and the d.c. component $i_{d.c.}$. By substituting equations 2.2 and 2.3 into equation 2.4 and summing over all CdS squares we obtain for the two current components of interest

$$i_{d.c.} = [g_L + (g_{LE}/2)(E_x^2 + E_y^2)] V_0 \sum_{m=-N}^{m=N} \sum_{n=-N}^{n=N} I_{mn} \quad (2.7)$$

$$i_{sig} = 2g_{LE} E_x E_y V_0 \sum_{m=-N}^{m=N} \sum_{n=-N}^{n=N} I_{mn} \exp(j(k_x m a + k_y n a)) \quad (2.8)$$

where a is the spacial period of the CdS squares as shown in Fig. 1. Since the image is sampled we can now define a reduced wave vector with components q_i ($i = x, y$)

$$k_i = q_i + (2\pi/a). \quad (2.9)$$

Substituting equation 2.9 into equation 2.8 brings the image back to "base band" in the reduced Fourier space.

$$i_{sig} = 2g_{LE} E_x E_y V_0 \sum_{m=-N}^{m=N} \sum_{n=-N}^{n=N} I_{mn} \exp(j(q_x m a + q_y n a)). \quad (2.10)$$

The current sensing electronics keep the d.c. photocurrent constant rather than keeping the d.c. voltage V_0 constant. This makes the output current less susceptible to aging, temperature, or other changes of the CdS films. Solving equation 2.7 for V_0 and substituting the result for V_0 into equation 2.10 we obtain for the signal current

$$i_{sig} = A i_{d.c.} \sum_{m=-N}^{m=N} \sum_{n=-N}^{n=N} I'_{mn} \exp(j(q_x m a + q_y n a)) \quad (2.11)$$

where

$$A = 2(g_{LE}/g_L) E_x E_y / [1 + (g_{LE}/2g_L)(E_x^2 + E_y^2)] \quad (2.12)$$

and the average normalized light intensity I'_{mn} incident on the mn 'th CdS square is

$$I'_{mn} = I_{mn} / \sum_{m=-N}^{m=N} \sum_{n=-N}^{n=N} I_{mn}. \quad (2.13)$$

Thus, the signal current i_{sig} , as shown in equation 2.11 is proportional to the Fourier transform of the normalized sampled image I' .

3. Experimental Arrangement

The device and its associated signal detecting circuitry is mounted in a camera box. A low pass filter with a cutoff frequency of 6 MHz and providing an attenuation of 80 db at 30 MHz is used for the detection of the difference frequency component. The characteristic impedance of the filter is 15 Ohms which matches the input impedance of the broad band current-sensing amplifier. A low input impedance is required of the device shunt capacitance (325 pF).

For some experiments, a peak detector is used at the output of the amplifier.

Each transducer is tuned by a series inductance to match its impedance to the impedance of the driving source. The transducer that generates the y-propagating acoustic wave is driven by a H.P. 8601A sweep oscillator. The input voltage to this transducer is swept in a continuous fashion in frequency over the bandwidth of the transducer centered at the center frequency of the transducer.

The other transducer is driven by a H.P. 3200A VHF oscillator. The frequency of the voltage applied to the transducer generating the x-propagating wave could, thus, only be changed manually. This arrangement results in raster scanning of Fourier space.

The incoming light is imaged on the device by means of a 50 mm focal length $f/1.8$ lens. The image is either front or back projected onto a screen facing the DEFT camera. A slide projector is used to display the image on the screen.

Oscilloscope pictures as shown in Figs. 2, 3, and 4 are generated by selecting a frequency for the x-transducer driving voltages and sweeping the frequency of the voltage applied to the y-transducer about 100 times per second. The horizontal deflection of the oscilloscope is controlled by a saw-tooth voltage output of the sweep generator. The amplitude of this saw-tooth voltage is proportional to the frequency of the voltage applied to the y-transducer. Thus the horizontal axis in these pictures is the y-frequency f_y . The peak detected output voltage of the signal amplifier is applied to the vertical input of the oscilloscope.

A Polaroid picture is taken of this oscilloscope trace.

Next, the x-transducer driving frequency is set to a new value, the oscilloscope trace is moved up and slightly to the right. The same Polaroid picture is exposed again to the resulting oscilloscope trace.

These steps are repeated until the desired

range of x-frequencies, f_x , is obtained.

The contrast measurements were obtained without the peak detector. The peak detector tends to clip the lower portion of the signal.

4. Transforms of Test Patterns

In this paper we demonstrate the response of the monolithic DEFT device to stationary test patterns. The simplest pattern to examine is uniform illumination. The signal output when the sensor is illuminated with uniform light is, from equations 2.11 and 2.13

$$i_{sig} = \frac{A}{(2N+1)^2} \sum_{m=-N}^{m=N} \sum_{n=-N}^{n=N} \exp(j(q_x m a + q_y n a)) \quad (4.1)$$

$$i_{sig} = \frac{A}{(2N+1)^2} \left[\frac{\cos N q_x a - \cos(N+1) q_x a}{1 - \cos q_x a} \right] \left[\frac{\cos N q_y a - \cos(N+1) q_y a}{1 - \cos q_y a} \right] \quad (4.2)$$

For our present device $N = 49$. It is one less than half of the numbers of sampling lines along each axis of the device. Indeed, for large N equation 4.2 reduces, as expected, approximately to a two-dimensional sinc function

$$i_{sig} = A \frac{\sin(q_x L/2)}{q_x L/2} \frac{\sin(q_y L/2)}{q_y L/2} \quad (4.3)$$

where $L = (2N+1)a$ the dimension of the aperture of the device. In the present case $L = 12.7$ mm's. The dispersion relation for the reduced wave vectors q_i is

$$2\pi(f_x - f_y)/v_s = q_x - q_y \quad (4.4)$$

where v_s is the surface wave velocity under the CdS film, 3759 m/sec in this case, f_x and f_y are the frequencies of oscillation of the voltages applied to the x- and y-transducers.

Consider the behavior of the sinc functions of equation 4.3 along the principal axis of the reduced Fourier transform space. For an aperture $L = 12.7$ mm the first zero of the sinc functions will occur at a difference frequency $h = |f_x - f_y|$ of 296 kHz from the center of the reduced Fourier space.

The response of the sensor to uniform illumination is shown in Fig. 2. Indeed we observe a 600 kHz-wide peak in the center of the reduced Fourier space with some side lobes along each axis, as predicted.

The next test pattern we used consisted of a periodic array of bright rectangles. The center-to-center spacing of the bright rectangles along the y-direction was 3.4 mm's. Three lines of rectangles crossed the x-axis and four lines of rectangles crossed the y-axis.

One would expect the following output from the device:

One would expect a peak with small sidelobes due to the average brightness of the pattern

located at the center of the reduced Fourier space.

One would expect a pair of symmetric peaks not on the axis due to the periodicity of the pattern in off-axis directions.

The transform of this pattern can be calculated from equations 2.11 and 2.13. One obtains a signal current of the form

$$i_{sig} = (A/3) \{ (1/2) + \cos b_x q_x \} \{ \cos(b_y q_y/2) + \cos(3b_y q_y/2) \} \text{sinc}(b_y q_y/4) \text{sinc}(b_x q_x/4) \quad (4.5)$$

where $b_x = 4.3$ mm is the center-to-center spacing of the rectangles in the x-direction and $b_y = 3.4$ mm is the center-to-center spacing of the rectangles in the y-direction.

There will be a pair of peaks at $q_y = 0$, $b_x q_x = \pm 2\pi$. Defining the reduced temporal frequency h_1 as

$$h_1 = q_1 v_s / 2\pi, \quad t = x, y. \quad (4.6)$$

Along the principal axis this frequency h_1 is equal to the difference frequency described previously. Using the appropriate values for v_s and b_x we find that these two peaks are located at $h_x = \pm 0.845$ MHz and $h_y = 0$. We observe peaks along the h_x axis in Fig. 3 at $h_x = \pm 0.865$ MHz. This is a 2.3% error due to a slightly different velocity in the x-direction.

Along the h_y axis we predict peaks at $h_y = \pm 1.079$ MHz, $h_x = 0$. We observe peaks at $h_y = \pm 1.08$ MHz, close to the predicted value.

One source that tends to distort the output signal is the inability of the amplifier to detect signals at zero difference temporal frequency. This results in a diagonal null line in the reduced transform space.

Fig. 4 is the transform of a chevron pattern. The transform of a chevron consists of peaks forming an "X" in transform space. This is discernable in Fig. 4. The complete transform of this pattern is quite complicated.

We can clearly see that the output of the device is quite predictable and distinct for each pattern.

5. Contrast Measurements

The contrast measurements were made with the aid of two slide projectors. Each projector was equipped with a variable iris so that the light intensity output could be varied. A pattern of equally spaced alternate dark and light bars was displayed on the screen by the use of one projector. The other projector was used to control the background illumination of the screen. The camera was placed to face the screen. The lens was adjusted to focus the image, displayed on the screen, onto the DEFT device.

The experiment was conducted by varying both background illumination and the light intensity

of the bar pattern in such a way as to keep the total light intensity of the image constant.

$$\sum_{n=-N}^{n=N} \sum_{m=-M}^{m=M} I_{mn} = \text{constant} \quad (5.1)$$

A pattern was chosen in such a way that there was an equal number of N of darker and brighter lines. The output of the device, according to equations 2.11 and 2.13, along the q_y axis ($q_x = 0$) is of the form

$$i_{sig} = \frac{(I_s - I_B)F(q_y) + I_B G(q_y)}{NI_B + NI_s} \quad (5.2)$$

where I_s is the light intensity of the bright lines, I_B is the background light intensity, $F(q_y)$ is a spacial frequency function exhibiting two symmetric peaks along the q_y axis associated with the periodic bar pattern, and $G(q_y)$ is a sinc-like function associated with the average illumination of the device.

All measurements were made at constant spacial frequency q_y at a peak of the function $F(q_y)$. The measurements were made at a sufficiently high spacial frequency so that the amplitude at q_y of the sinc function $G(q_y)$, associated with the aperture, was small enough to be neglected. (See Fig. 2 for the extent of aperture sinc function.)

In this case equation 5.2 reduces to

$$i_{sig} = [F(q_y)/N] C$$

where the contrast C is defined as

$$C = (I_s - I_B)/(I_s + I_B) \quad (5.4)$$

We have measured the contrast response of the device. The results of the measurements are shown in Fig. 5. Indeed, the output of the device is a linear function of the contrast C .

Thus, we have shown in both experiments described here and in previous publications [1,2,3,4,5] that the device, indeed, performs as predicted by theory.

6. Conclusion

In this communication we have demonstrated some of the capabilities of our new monolithic DEFT sensor. We have overcome some of the difficulties associated with the external sampling grid of our previous sensor. We are now able to image a light pattern by means of a highly converging lens on the device. This was difficult to do with the external sampling grid.

We are now working on a sensor with much higher resolution and moderate low light level capability. We also intend to operate the sensor in a line scan mode. This line scan mode could be especially useful for reading out infrared sensitive diodes. We hope to extend our work to

devices using infrared sensitive materials.

References

1. S.T. Kowel, P.G. Kornreich, A. Mahapatra, D. Cleverly, B. Emmer, and R. Zawada, "Two-Dimensional Fourier Imaging of Light Using Acoustic Pseudo Beam Steering," 1975 Ultrasonics Symposium Proceedings, pp. 136-140.
2. S.T. Kowel, P.G. Kornreich, A. Mahapatra, and B. Emmer, "Experimental Confirmation of Two-Dimensional Acoustic Processing of Images," 1976 Ultrasonics Symposium Proceedings, pp. 668-672.
3. S.T. Kowel, P.G. Kornreich, A. Mahapatra, M. Mehter, and P. Reck, "The Vector Imaging Convolver," 1977 Ultrasonics Symposium Proceedings, pp. 715-720.
4. S.T. Kowel, P.G. Kornreich, K.W. Loh, A. Mahapatra, M. Mehter, B. Emmer, P. Reck, W.A. Penn, "Two-Dimensional Transform (DEFT) Devices: Analysis, Fabrication and Evaluation," Report DAAG53-76-C-0162 (1976), prepared for U.S. Army Night Vision Laboratory, Ft. Belvoir, VA 22060
5. S.T. Kowel, P.G. Kornreich, K.W. Loh, A. Mahapatra, M. Mehter, P. Reck, and B. Emmer, "Imaging Without Spacial Raster Scanning," submitted for publication in the IEEE Transactions on Electron Devices, to be published.
6. P.G. Kornreich, A. Mahapatra, S.T. Kowel, K.W. Loh, and B. Emmer, "Double-Layered Polycrystalline Cadmium Sulfide on Lithium Niobate," J. Appl. Phys., Vol 49, pp. 2443-2448, (1978).
7. M. Luukkala, P. Merilainen, and K. Saarinen, "Acousto-Resistive Effects in Thin Films of CdSe/LiNbO₃ Delay Line System," 1974 Ultrasonics Symposium Proceedings, pp. 345-347.
8. E.S. Kohn and M. Lampert, Phys. Rev. B4, p. 4479 (1971)
9. A. Mahapatra, P.G. Kornreich, and S.T. Kowel, "Strain Induced Modulation of Photoconductivity in Thin Polycrystalline Films of Cadmium Sulfide," accepted for publication in the Sept., 1978, issue of the Phys. Rev., Vol B18.

* Note: Figure 2 and Figure 3 should be interchanged.

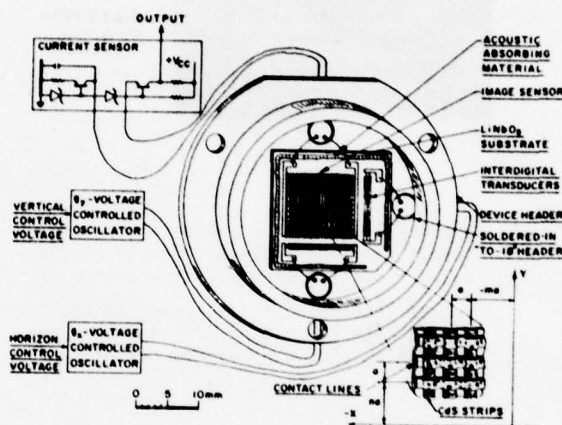


Fig. 1. Photoconducting DEFT sensor mounted in a header. Note the image sampling arrangement shown in the lower right corner. The sensor described here uses a monolithic aluminum film shadow mask to sample the image in the x-direction rather than etching the CdS films into lines as shown above.

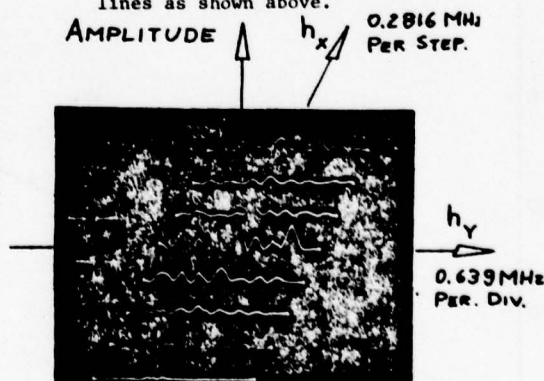


Fig. 2. The magnitude of the output signal as a function of the reduced temporal frequency $h_i = q_i v_s / 2\pi$ ($i = x, y$) for uniform illumination of the sensor. Note the single peak with small side lobes in the center of the transform space.

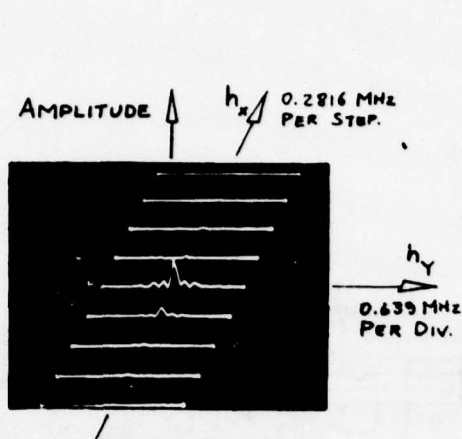


Fig. 3. The magnitude of the output signal as a function of the reduced temporal frequency $h_i = q_i v / 2\pi$ ($i = x, y$) for a grid of bright rectangles as described in the text. Note the center peak and two peaks on each axis of the reduced frequency space.

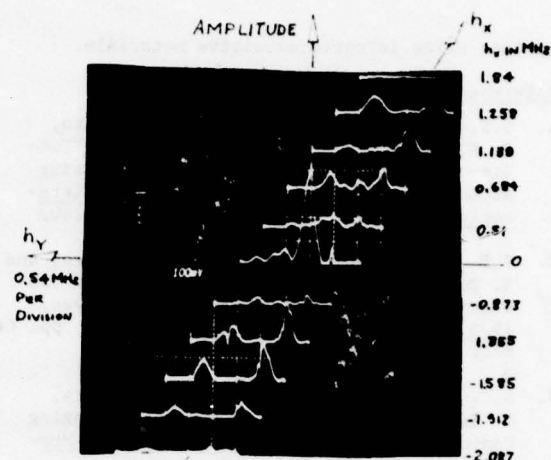


Fig. 4. The magnitude of the output signal as a function of the reduced temporal frequency $h_i = q_i v / 2\pi$ ($i = x, y$) for a chevron pattern. Four off-axis peaks forming roughly an "X" pattern are visible.

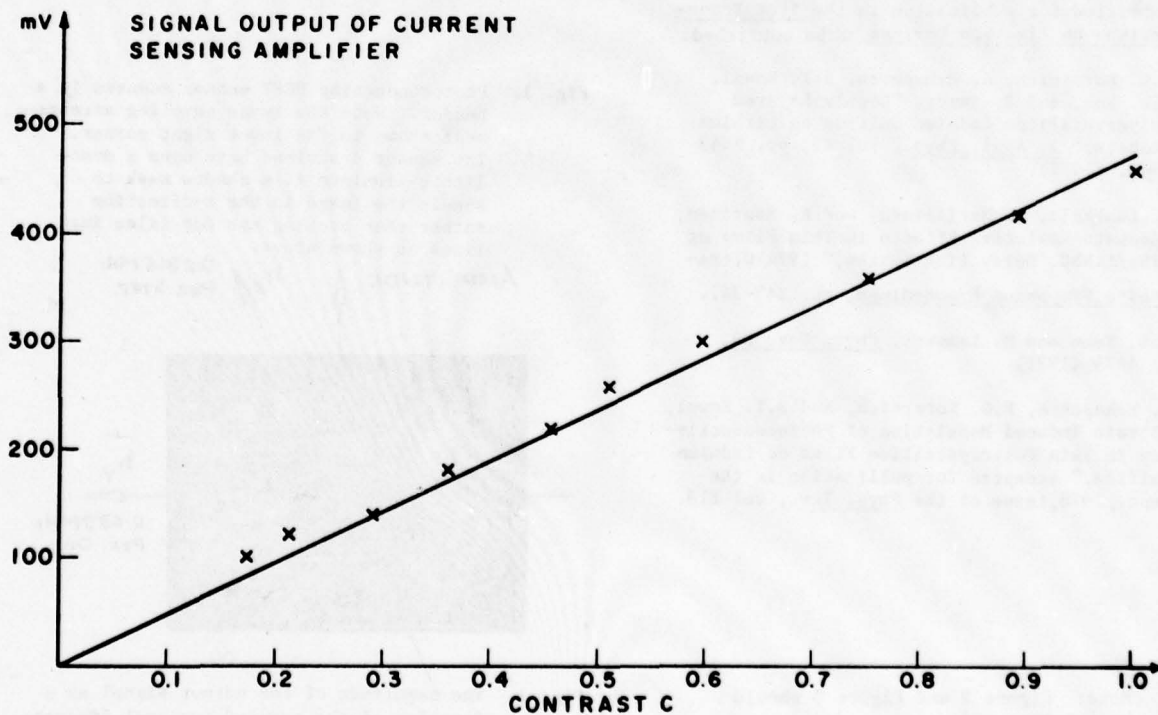


Fig. 5. The contrast response of the device. Note that the response is linear as predicted.

APPENDIX VII.

A TWO-DIMENSIONAL ACOUSTIC PROCESSOR

1978 International Optical Computing Conference
London, England

1978 INTERNATIONAL OPTICAL COMPUTING CONFERENCE
London, England

A TWO-DIMENSIONAL ACOUSTIC PROCESSOR

S.T. Kowel, D. Cleverly, A. Mahapatra, T. Szebenyi, and P.G. Kornreich: Department of Electrical and Computer Engineering, Syracuse University, Syracuse, New York 13210

Stephen Wanuga: Electronics Laboratory, General Electric Company, Syracuse, New York 13221

Abstract

A new direct electronic Fourier transform (DEFT) system has been developed for two-dimensional imaging of two-dimensional signals. The image is focused on a fused quartz valve in which two perpendicularly travelling longitudinal waves are launched, one at frequency ω_1 , the other at ω_2 . This yields an intensity containing a term in the photocurrent at the difference frequency proportional to the k Fourier component of $I(\vec{r})$, where k is the sum of the original acoustic wavevectors, and $I(\vec{r})$ is the input optical signal. Thus by varying the transducer frequencies, arbitrary Fourier components can be obtained by this "pseudo beam steering," as if a new acoustic wave had been created.

Base band Fourier imaging is obtained by placing a sampling mask in front of the valve in order to place the optical intensity on a spatial carrier appropriate for the transducers. The system can electronically track a rotating image, measuring the spatial frequencies and orientation of image transform components.

Image processing by means of acoustical modulation has received considerable attention. Successful devices for optical deflection [1], image scanning [2,3], and Fourier transformation [2,3,4,5,6,7,8] have been reported. Most of this work has been concerned with structures capable of "one axis" operation, such as deflection about a single axis, etc. In 1974, we described an electrophotoconductive structure which could be used for full "two-dimensional" image processing [6]. In 1975, we also described an elastobirefringent light valve system for accomplishing the same purpose [9]. Since that time, the electrophotoconductive device has been fabricated [7,8,10]. In this paper we report conclusive evidence for the operation of a light valve system as a fully two-dimensional Fourier transforming system. This first prototype system can electronically probe the two-dimensional Fourier transform, yielding the vector spatial frequencies present in the image intensity focussed on the valve and the relative amplitudes of these components.

The direct electronic Fourier transform (DEFT) devices derive signals representative of

Fourier components by acoustically modulating photoelectrons. In the electrophotoconductive device, two surface acoustic waves, travelling perpendicularly, cross the image, focussed on a thin photoconductive film (CdS in the current model). It has been demonstrated that the photocurrent is strongly dependent on applied electric field, with the generated photocurrent having a component proportional to the square of the electric field [7,8]. We provide the electric fields by propagating the two crossed surface acoustic waves on a piezoelectric substrate (LiNbO_3) on which CdS has been deposited. Deposited contacts detect a current

$$i(t) \propto \iint dx dy E_z^2(x,y,t) I(x,y) \quad (1)$$

where $I(x,y)$ is the image intensity as a function of the x - and y -coordinates along the film, and E_z is the electric field associated with the surface acoustic wave (SAW) in the substrate.

The simplest mode of operation occurs when the transducers are driven with sinusoids of arbitrary frequency, yielding

$$E_z = E_1 \cos(\omega_1 t - k_1 x) + E_2 \cos(\omega_2 t + k_2 y) \quad (2)$$

where E_1 , ω_1 , k_1 refer to the x -directed SAW, and E_2 , ω_2 , k_2 refer to the y -directed SAW. Thus (1) contains a term

$$i_s \propto \exp\{j(\omega_1 - \omega_2)t\} \iint d^2\vec{r} I(\vec{r}) \exp(-j\vec{k} \cdot \vec{r}). \quad (3)$$

By varying the driving frequencies, we vary \vec{k} , the vector sum of k_1 and k_2 . That is, the signal behaves as if a new acoustic wave has been created with wavevector equal to the sum of the excited wavevectors. Thus we call this effect "pseudo beam steering."

The alternative structure reported here relies on strain-induced birefringence in a light valve sandwich. Fig. (1) shows a schematic of the system in which this valve is employed. The image is impressed on the surface of a fused quartz plate by a well-collimated optical system. The intensity modulation has a component proportional to the strain squared, thus providing a mechanism for pseudo beam steering. The modulated light passes through the polarizer-valve-analyzer sandwich and is detected by a photo-detector with circuitry tuned to the difference frequency. This structure requires more light but

is easier to build, at least for use as an optical instrument, since it is made from existing hardware. It will also not suffer from relaxation time effects, thus providing much faster time response to image changes. Simple one-dimensional experiments have already been reported [6] for a similar structure.

From theoretical considerations, it appears that pseudo beam steering is likely to be far superior to other proposed techniques for accomplishing two-dimensional imaging. For example, the actual creation of a third wave from nonlinear mixing appears to be a much smaller and less controllable effect, since the original waves produce a cbrrogated "background" for the mixed wave.

A Pseudo Beam Steering Elastobirefringent Light Valve

Our previous work with the elastobirefringent light valve using standing acoustic waves [5,6], and the possibility of using pseudo beam steering to obtain arbitrary Fourier components, led to the consideration of a travelling wave elastobirefringent light valve. Such a system was assembled, using the same z-cut LiNbO_3 substrate used in the CdS sensor. Unfortunately, while some changes in average light transmittance were observed, no successful measurements of difference frequency signals were obtained. This appears to result from the high level of non-homogenous natural birefringence present in the material. This natural birefringence could not be blocked by careful alignment of the polarizers or by the addition of a quarter wave plate appropriate for the 6328A He-Ne laser used as a light source. While adjustments permitted the transmitted intensity to be minimized in some places, it was not possible to get a uniform null over the 1 cm by 1 cm aperture. Thus, after numerous attempts, we abandoned LiNbO_3 as a substrate. By using a fused quartz cell, we were able to obtain a uniformly dark field, since quartz is isotropic and homogenous. Longitudinal strain waves were produced by LiNbO_3 transducers bonded to two edges of the quartz plate. Fig. (1) shows a schematic view of the configuration used with the light valve to obtain the two-dimensional transform of an image.

Two orthogonal transducers are shown; one in the positive x-direction and one in the negative y-direction. The strain in the region of the quartz substrate where both longitudinal waves propagate is the linear super-position of the two travelling strain waves. Therefore, it can be expressed as

$$\epsilon = \sum_{x1} \cos(k_1 x - \omega_1 t) + \sum_{y1} \cos(k_2 y + \omega_2 t). \quad (4)$$

An image is impressed on the region of the quartz where the two waves are superimposed. It may be shown that we are working in the Raman-Nath region so that the light rays remain parallel inside the material. The polarizer and analyzer

are crossed to pass a minimum amount of light when no electrical signal is applied to the transducers.

Due to the strain-induced birefringence, each ray of light splits into two orthogonally polarized rays which travel inside the material with different phase velocities. Let the phase difference between the two rays after they exit the material be δ . Then the intensity of the light I_0 at the detector in Fig. (1) is given by [5]

$$I_0(x, y) = I(x, y) \sin^2 \frac{\delta}{2} \quad (5)$$

where I is the light intensity of the image at the valve.

The relationship of this phase difference to the strain is

$$\delta = \frac{\pi L p n^3}{\lambda} \epsilon \quad (6)$$

where p is a constant depending on the elasto-optical constants of the material, L is the thickness of the plate, n is the refractive index of the material, and λ is the wavelength of light. Thus (5) can be expanded yielding

$$I_0(x, y) = I(x, y) \left[\left(\frac{\delta}{2} \right)^2 - \frac{1}{3} \left(\frac{\delta}{2} \right)^4 + \dots \right]. \quad (7)$$

Keeping only the first term yields

$$I_0(x, y) = \frac{I(x, y)}{4} \delta^2. \quad (8)$$

The contribution of higher order terms which normally would have to be considered is not important in this case since no term except the first contributes to the difference frequency which will be detected. Substituting the phase difference from (6) and the strain, (4), yields

$$I_0(x, y) = \frac{I(x, y)}{4} \left(\frac{\pi L p n^3}{\lambda} \right)^2 \left[\sum_{x1} \cos(k_1 x - \omega_1 t) + \sum_{y1} \cos(k_2 y + \omega_2 t) \right]^2. \quad (9)$$

The squaring produces a current term at the difference frequency which at the output of the photodetector is given by

$$i(t) = \frac{R}{8} \left(\frac{\pi L p n^3}{\lambda} \right)^2 \sum_{x1} \sum_{y1} \iint I(\vec{r}) \cos(\vec{k} \cdot \vec{r} - \Delta \omega t) d^2 \vec{r} \quad (10)$$

where $\vec{k} = k_1 \hat{x} = k_2 \hat{y}$,

$$\vec{r} = x \hat{x} + y \hat{y},$$

$$\Delta \omega = \omega_1 - \omega_2,$$

and R is the responsivity of the detector.

Thus, we observe a current proportional to the \vec{k} Fourier component of the incident optical intensity at the difference frequency of the two transducers. By varying the transducer frequencies over their bandwidth, the spatial spectrum of the image can be obtained. Thus elastobirefringence provides a mechanism for pseudo beam steering. This system behaves as if there were a travelling disturbance with wavevector \vec{k} and frequency $\Delta \omega$, when in fact there is merely a quasi stationary variation in optical refractive index.

Consider a fused quartz light valve with a high sensitivity detector. Approximate values for (10) are

$$R = 70 \text{ milliamps/watt}$$

$$n = 1.54$$

$$\lambda = 0.63 \times 10^{-6} \text{ m}$$

$$L = 0.635 \text{ cm}$$

$$p = 0.15$$

$$\int_{x1} = \int_{y1} = 10^{-5}.$$

The area of the valve (and detector) is approximately 6 cm^2 . Substitution into (10) yields for the current magnitude for the $k = 0$ component approximately 0.16×10^{-6} amperes.

Since the detector has a dark current of 10 pA , components of the Fourier transform four orders of magnitude below the $k_1 = k_2 = 0$ component could theoretically be detected. Since all image intensities have transforms which go down as $1/k$ for large k , each order of magnitude corresponds to a decade of spatial frequency bandwidth. This demonstrates one important advantage of the light valve over the elastophotocoductive devices. By using a very low dark signal detector as a separate entity, a far greater spatial bandwidth can be obtained. This also effects several other advantages. The thin film devices suffer from rather long rise time and fall time (approximately 1 ms) due to carrier effects, thus limiting their temporal bandwidth. In practice, this limits them to use with images which do not change significantly in less than a few milliseconds. The only time limitations on the light valve system are caused by the detector since the valve responds instantaneously to the light.

The calculations and estimates above do not include one important constraint in the design of the system. The transducers selected have fundamental frequencies of 40 MHz with bandwidths expected to be 15% . In order to perform base-band Fourier imaging (around $k = 0$, as indicated in (10)), it is necessary to put the optical signal, $I(r)$, on a spatial carrier whose radian spatial frequency equals the spatial frequency of the 40 MHz acoustic wave [8]. Otherwise, the values of $|k|$ will be so large that little information will be obtained since the acoustic system is centered at high spatial frequencies. The image is placed on a carrier by a sampling mask affixed to the valve. For a velocity of 5960 m/s at 40 MHz , the wavelength is $149 \text{ }\mu\text{m}$ in both the x - and y - directions.

The quartz plate itself is $2.54 \text{ cm} \times 2.54 \text{ cm} \times 0.635 \text{ cm}$ thick. A calculation of the optical Rayleigh range

$$Z_R = \frac{\pi d^2}{\lambda} = 2.77 \text{ cm} \quad (11)$$

where d is the width of the sampling apertures ($149 \text{ }\mu\text{m}/2$) shows that the image remains well sampled throughout the optical path within the 0.635 cm thick plate.

Thus the intensity pattern exiting the valve sandwich (10) has only low frequency variation. Assuming a 20% acoustic bandwidth, the Rayleigh range will be at least one meter,

$$Z_{RI} = \pi \frac{(L/34)^2}{.63 \times 10^{-6}} = 2.78 \text{ m}. \quad (12)$$

Placement of an extended detector within one meter from the valve will insure proper operation including "local" detection of intensity and spatial integration.

Experimental Results

Four thin transducers with wrap-around electrodes were purchased and bonded to the quartz plate. After testing, two were removed and those contiguous plate edges sand blasted in order to produce travelling acoustic waves rather than standing waves. The placement of the transducers is shown in Fig. 2.

The device is mounted in a holder with BNC connectors to facilitate the signal input to the transducers.

On one of the square faces a sampling grid was placed to shift the center of the Fourier space from zero to $f_x = 38.3 \text{ MHz}$ and $f_y = 38.3 \text{ MHz}$, which is in the center of the bandwidth of the transducers. The sampling grid dimensions are $1 \text{ cm} \times 1 \text{ cm}$.

The input light was from a 15 mW HeNe laser with a telescopic expander adjusted to give a beam diameter of 1.0 cm maximum at the device. The polarizers were set such that there was a minimum of light transmitted when no signal was applied to the transducers. The output was detected by an EEG 585 photomultiplier and the output was displayed on a Tektronix spectrum analyzer. This arrangement is shown in Fig. 1.

Standing Waves

Unfortunately, the sand blasting was not very effective and a strong pattern of discrete, equally spaced, frequencies was detected. Since the valve was so long compared to acoustic wavelength, no two-dimensional modes were formed due to each transducer. Thus the system worked as expected, except for a rapid "sampling" of the transform space.

The bandwidth or extent of the signal peak can be easily calculated by

$$BW = \frac{v}{d} \quad (13)$$

where v is the velocity (5960 m/sec) and d is the beam diameter ($.005 \text{ m}$ in this case), giving the signal bandwidth as 1.2 MHz . Fig. 3 shows a standing wave pattern. The standing wave peaks are 0.12 MHz apart and have a bandwidth of 40 KHz . By pulse delay experiments it can be shown that the wave velocity is indeed

$$v = \frac{2\ell}{t} \quad (14)$$

where ℓ is the crystal size ($.0254 \text{ m}$) and t is the round trip transit time of the pulse ($8.4 \times 10^{-6} \text{ sec}$) giving a velocity of 6047 m/sec , very close to the published longitudinal velocity.

It is of interest that, in accordance with (7), no linear terms were observed. Within the bandwidth of the detector (50 MHz), the only signals found were the difference frequencies. No signals at 40 MHz were seen.

Bar Pattern Experiment

The simplest image for which one can calculate and observe the Fourier transform is a bar pattern of light and dark stripes. If we consider that the wavelength is given by the distance from the center of one light band to the center of the next light band, then the frequency is given by

$$\Delta f = \frac{v_p}{\lambda_p} \quad (15)$$

where v_p and λ_p are the pseudo wave parameters. The actual frequency measured is then 38.3 MHz $\pm \Delta f$. The direction of \vec{k} from the center is the direction of a vector perpendicular to the bar pattern stripes. Thus one can rotate the image, follow the signal by changing the two frequencies, and transcribe a circle in Fourier space. Three different bar patterns or spatial periodic images were tried, and the longitudinal velocity of sound in the crystal is given as 5960 m/sec. Table I gives the wavelength and Fourier frequency for the patterns tried.

spatial pattern	λ	Δf
A	$1.78 \times 10^{-3} \text{ m}$	3.40 MHz
B	$3.64 \times 10^{-3} \text{ m}$	1.634 MHz
C	$6.20 \times 10^{-3} \text{ m}$.961 MHz

In Fig. 4 the circles represent the theoretical calculated value of Δf when the image is rotated about 360°. The crosses represent data taken at several selected angles for each spatial pattern.

Circular Pattern

Fig. 5 shows a circular aperture whose Fourier transform is given by

$$F(\vec{k}) = \frac{1}{2\pi} \iint_{\text{area}} f(r, \theta) \exp(-j\vec{k} \cdot \vec{r}) d^2\vec{r} \quad (16)$$

where

$$f(r, \theta) = \begin{cases} 1 & b > r > a \\ & 0 > \theta > \pi \\ 0 & \text{otherwise} \end{cases}$$

which then gives

$$F(k) = \frac{b^2 J_1(kb)}{kb} - \frac{a^2 J_1(ka)}{ka} \quad (17)$$

by choosing $b = 0.5 \text{ cm}$ and $a = 0.16 \text{ cm}$ a calculated minima for the transform is at 0.95 MHz in the radial direction from the center of the sampled \vec{k} space. In Fig. 6, the solid circle represents the calculated transform and the crosses are the data points. The signal amplitude is very small and only a few DBm above the signal associated with the sinc function lobes of the aperture response.

Conclusions

We have verified the two-dimensional pseudo beam steering effect by quantitative experiments in which Fourier spectra of a variety of images were obtained. We measured spatial frequencies and tracked them during rotation experiments over a full 360°.

Future improvements include further attempts to produce a travelling wave system by more effective sand blasting and through the addition of absorbing materials on the edges opposite the transducers.

Bibliography

1. C.S. Tsai, "Wideband Guided-Wave Acoustooptic Bragg Devices and Applications," 1975 Ultrasonics Symposium Proceedings, pp. 120-125.
2. G.S. Kino, "Acoustoelectric Interactions in Acoustic-Surface-Wave Devices," Proc. IEEE, Vol. 64, May 1976, pp. 724-748.
3. M. Luukkala, "Applications of the Acousto-Electric SAW Image Scanners," 1977 Ultrasonics Symposium Proceedings, pp. 165-170.
4. P. Kornreich, N.T. Yang, and S.T. Kowel, "A Direct Electronic Fourier Transform Device for Imaging," IEEE Proc. Letters, Vol. 61, Aug. 1973.
5. P.G. Kornreich, S.T. Kowel, D.J. Fleming, N.T. Yang, A. Gupta, and O. Lewis, "DEFT: Direct Electronic Fourier Transforms of Optical Images," IEEE Proceedings, Vol. 62, pp. 1072-1087, Aug. 1974.
6. S.T. Kowel, P.G. Kornreich, O. Lewis, A. Gupta, and R. Zawada, "Progress on Two-Dimensional Direct Electronic Fourier Transform (DEFT) Devices," 1974 Ultrasonics Symposium Proceedings, pp. 763-767.
7. S.T. Kowel, P.G. Kornreich, A. Mahapatra, B. Emmer, M. Mehter, and P. Reck, "The Vector Imaging Convolver," 1977 Ultrasonics Symposium Proceedings, pp. 715-720.
8. P.G. Kornreich, S.T. Kowel, K.W. Loh, A. Mahapatra, M. Mehter, and B. Emmer, "Imaging Without Raster Scanning," IEEE Trans. on Electron Devices, to be published.
9. S.T. Kowel, P.G. Kornreich, A. Mahapatra, D. Cleverly, B. Emmer, and R. Zawada, "Two-Dimensional Fourier Imaging of Light Using Acoustic Pseudo-Beam Steering," 1975 Ultrasonics Symposium Proceedings, pp. 136-140.

The subject of spurious surface wave generation in layered SAW devices has received considerable attention in the literature. It has been shown by Farnell and Adler [4], that the presence of layers on isotropic or piezoelectric substrates will

($f_{x0}, f_{y0} + \Delta f_y/2$). There is one spurious dc peak to the right of the main dc peak which may produce some undesirable effects. But the other two spurious dc peaks are outside the scanned frequency space. It is true that this design permits

72

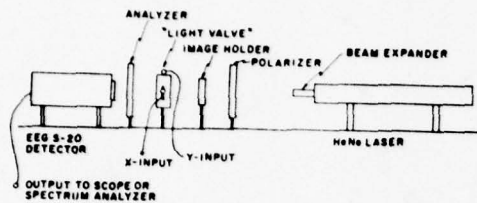


Figure 1. Experimental setup for the two dimensional light valve. The x and y inputs are connected to different frequency generators.

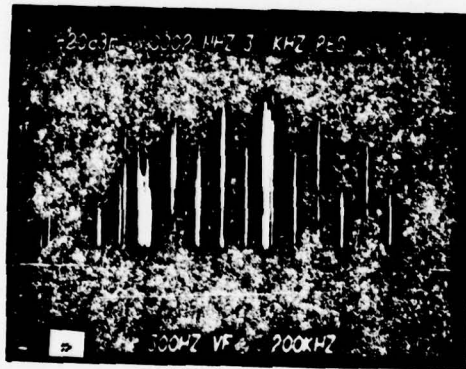


Figure 3. The Fourier transform of several different bar patterns. The spatial wavelength corresponding to the Fourier frequencies are a) $\lambda = 6.20$ mm and $\Delta f = 0.961$ MHz; b) $\lambda = 3.64$ mm and $\Delta f = 1.634$ MHz and c) $\lambda = 1.78$ mm and $\Delta f = 3.40$ MHz.

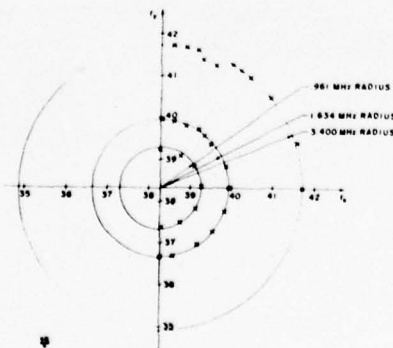


Figure 4. The image peak composed of standing wave modes. The signal has been sent through an amplifier with a gain of 50 db.

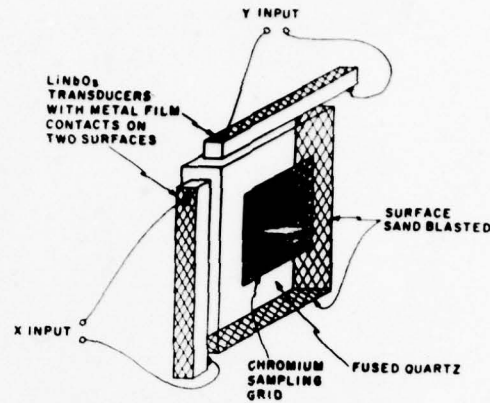


Figure 2. The "light valve" with LiNbO_3 transducers and sampling grid.

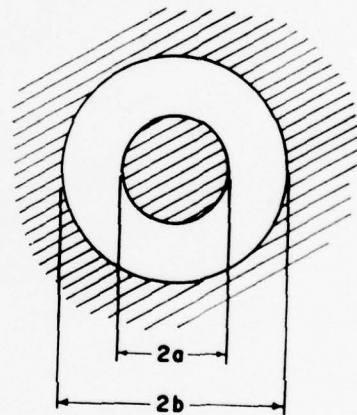


Figure 5. The circular hole image with inner radius a and outer radius b.

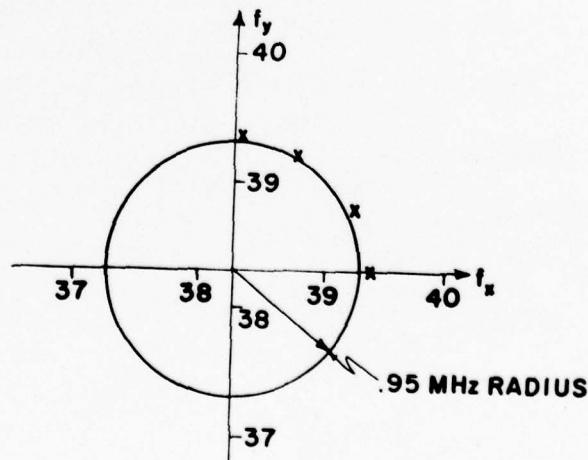


Figure 6. The Fourier transform of the circular hole with $a = 1.6$ mm and $b = 5.0$ mm.

* Note: Figure 2 and Figure 3 should be interchanged.

APPENDIX VIII.

TWO-DIMENSIONAL PHOTOACOUSTIC IMAGE PROCESSING
WITH LONGITUDINAL WAVES

1978 Ultrasonics Symposium Proceedings
IEEE Cat. #78CH 1344 - ISU

TWO-DIMENSIONAL PHOTOACOUSTIC IMAGE PROCESSING WITH LONGITUDINAL WAVES

S.T. Kowel, D. Cleverly, A. Mahapatra, T. Szebenyi, and P.G. Kornreich: Department of Electrical and Computer Engineering, Syracuse University, Syracuse, New York 13210

Stephen Wanuga: Electronics Laboratory, General Electric Company, Syracuse, New York 13221

Abstract

A new direct electronic Fourier transform (DEFT) system has been developed for two-dimensional imaging of two-dimensional signals. The image is focused on a fused quartz valve in which two perpendicularly travelling longitudinal waves are launched, one at frequency ω_1 , the other at ω_2 . This valve, placed between two crossed polarizers to block unmodulated light, yields an exit intensity containing a component proportional to the product of the input intensity with a sine wave "travelling" at the difference frequency and with an associated wavevector equal to the sum of the original wavevectors. Thus when this light is collected by a photocell, there is a term in the photocurrent at the difference frequency proportional to the \vec{k} Fourier component of $I(\vec{r})$, where $\vec{k} = k_1\hat{x} + k_2\hat{y}$, is the vector sum created by the squaring effect of the birefringence, and $I(\vec{r})$ is the input optical signal. Thus by varying the transducer frequencies, arbitrary Fourier components can be obtained by this "pseudo beam steering", as if a new acoustic wave had been created.

Base band Fourier imaging is obtained by placing a sampling mask in front of the valve in order to place the optical intensity on a spatial carrier appropriate for the 40 MHz center frequency LiNbO_3 transducers.

Introduction

Image processing by means of acoustical modulation has received considerable attention. Successful devices for optical deflection [1], image scanning [2,3], and Fourier transformation [2,3,4,5,6,7,8] have been reported. Most of this work has been concerned with structures capable of "one axis" operation, such as deflection about a single axis, etc. In 1974, we described an electrophotoconductive structure which could be used for full "two-dimensional" image processing [6]. In 1975, we also described an elastobirefringent light valve system for accomplishing the same purpose [9]. Since that time, the electrophotoconductive device has been fabricated

[7,8,9]. In this paper we report conclusive evidence for the operation of a light valve system as a fully two-dimensional Fourier transforming system. This first prototype system can electronically probe the two-dimensional Fourier transform, yielding the vector spatial frequencies present in the image intensity focussed on the valve and the relative amplitudes of these components.

The structure reported here relies on strain-induced birefringence in a light valve sandwich. Fig. 1 shows a schematic of the system in which this valve is employed. The image is impressed on the surface of a fused quartz plate by a well-collimated optical system. The intensity modulation has a component proportional to the strain squared, thus providing a mechanism for pseudo beam steering. The modulated light passes through the polarizer-valve-analyzer sandwich and is detected by a photodetector with circuitry tuned to the difference frequency. This structure requires more light than the electrophotoconductive device, but is easier to build, at least for use as an optical instrument, since it is made from existing hardware. It will also not suffer from relaxation time effects, thus providing much faster time response to image changes. Simple one-dimensional experiments have already been reported [6] for a similar structure.

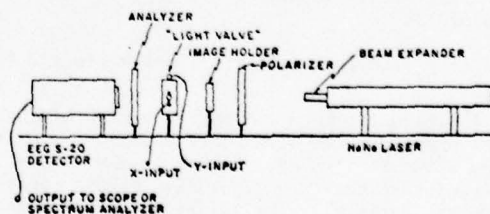


Fig. 1. Experimental setup for the two-dimensional light valve. The x and y inputs are connected to different frequency generators.

From theoretical considerations, it appears that pseudo beam steering is likely to be far

layered CdS film [6] deposited on a z-cut LiNbO₃ substrate. The metal contacts, consisting of an Al/In film sandwich in the form of an interdigital pattern, are deposited onto the CdS film. This

* Work supported by U.S. Army Night Vision & Electrooptics Laboratory, Ft. Belvoir, VA.

of elements of the electrophotoreactivity tensor.

The dark conductivity, that is the conductivity in the absence of light, is very small and

49

CH1305-2/79/0000-0049\$00.75 © 1979 IEEE

75

superior to other proposed techniques for accomplishing two-dimensional imaging. For example, the actual creation of a third wave from nonlinear mixing appears to be a much smaller and less controllable effect, since the original waves produce a corrugated "background" for the mixed wave.

A Pseudo Beam Steering Elastobirefringent Light Valve

Our previous work with the elastobirefringent light valve using standing acoustic waves [5,6], and the possibility of using pseudo beam steering to obtain arbitrary Fourier components, led to the consideration of a travelling wave elastobirefringent light valve. Such a system was assembled, using the same z-cut LiNbO₃ substrate used in the CdS sensor. Unfortunately, while some changes in average light transmittance were observed, no successful measurements of difference frequency signals were obtained. This appears to result from the high level of non-homogenous natural birefringence present in the material. This natural birefringence could not be blocked by careful alignment of the polarizers or by the addition of a quarter wave plate appropriate for the 6328A He-Ne laser used as a light source. While adjustments permitted the transmitted intensity to be minimized in some places, it was not possible to get a uniform null over the 1 cm by 1 cm aperture. Thus, after numerous attempts, we abandoned LiNbO₃ as a substrate. By using a fused quartz cell, we were able to obtain a uniformly dark field, since quartz is isotropic and homogenous. Longitudinal strain waves were produced by LiNbO₃ transducers bonded to two edges of the quartz plate. Fig. 1 shows a schematic view of the configuration used with the light valve to obtain the two-dimensional transform of an image.

Two orthogonal transducers are shown; one in the positive x-direction and one in the negative y-direction. The strain in the region of the quartz substrate where both longitudinal waves propagate is the linear super-position of the two travelling strain waves. Therefore, it can be expressed as

$$\epsilon = \sum_{x1} \cos(k_1 x - \omega_1 t) + \sum_{y1} \cos(k_2 y + \omega_2 t). \quad (1)$$

An image is impressed on the region of the quartz where the two waves are superimposed. It may be shown that we are working in the Raman-Nath region so that the light rays remain parallel inside the material. The polarizer and analyzer are crossed to pass a minimum amount of light when no electrical signal is applied to the transducers.

Due to the strain-induced birefringence, each ray of light splits into two orthogonally polarized rays which travel inside the material with different phase velocities. Let the phase difference between the two rays after they exit the material be δ . Then the intensity of the light I_0 at the detector in Fig. 1 is given by [5]

$$I_0(x,y) = I(x,y) \sin^2 \frac{\delta}{2} \quad (2)$$

where I is the light intensity of the image at the valve.

The relationship of this phase difference to the strain is

$$\delta = \frac{\pi L p n^3}{\lambda} \epsilon \quad (3)$$

where p is a constant depending on the elastooptical constants of the material, L is the thickness of the plate, n is the refractive index of the material, and λ is the wavelength of light. Thus (2) can be expanded yielding

$$I_0(x,y) = I(x,y) \left[\left(\frac{\delta}{2} \right)^2 - \left(\frac{\delta}{2} \right)^4 + \dots \right]. \quad (4)$$

Keeping only the first term yields

$$I_0(x,y) = \frac{I(x,y)}{4} \delta^2. \quad (5)$$

The contribution of higher order terms which normally would have to be considered is presumably small. Substituting the phase difference from (3) and the strain, (1), yields

$$I_0(x,y) = \frac{I(x,y)}{4} \left(\frac{\pi L p n^3}{\lambda} \right)^2 \left[\sum_{x1} \cos(k_1 x - \omega_1 t) + \sum_{y1} \cos(k_2 y + \omega_2 t) \right]^2. \quad (6)$$

The squaring produces a current term at the difference frequency which at the output of the photodetector is given by

$$i(t) = \frac{R}{8} \left(\frac{\pi L p n^3}{\lambda} \right)^2 \sum_{x1} \sum_{y1} \iint I(\vec{r}) \cos(\vec{k} \cdot \vec{r} - \Delta \omega t) d^2 \vec{r} \quad (7)$$

where $\vec{k} = k_1 \hat{x} + k_2 \hat{y}$,

$$\vec{r} = x \hat{x} + y \hat{y},$$

$$\Delta \omega = \omega_1 - \omega_2,$$

and R is the responsivity of the detector.

Thus, we observe a current proportional to the \vec{k} Fourier component of the incident optical intensity at the difference frequency of the two transducers. By varying the transducer frequencies over their bandwidth, the spatial spectrum of the image can be obtained. Thus elastobirefringence provides a mechanism for pseudo beam steering. This system behaves as if there were a travelling disturbance with wavevector \vec{k} and frequency $\Delta \omega$, when in fact there is merely a quasi-stationary variation in optical refractive index. Notice that even if the full expansion of $\sin^2 \frac{\delta}{2}$ is used in (8), the component of current at the difference temporal frequency and sum wavevector is still proportional to the Fourier transform of the optical image.

Consider a fused quartz light valve with a

high sensitivity detector.

Approximate values for (7) are

$$R = 70 \text{ milliamps/watt}$$

$$n = 1.54$$

$$\lambda = 0.63 \times 10^{-6} \text{ m}$$

$$L = 0.63 \text{ cm}$$

$$p = 0.15^{(10)}$$

$$\sum_{x1} = \sum_{y1} = 10^{-5}$$

The area of the valve (and detector) is approximately 6 cm^2 . Substitution into (7) yields for the current magnitude for the $\bar{k} = 0$ component approximately 0.16×10^{-6} amperes.

Since the detector has a dark current of 10 pA , components of the Fourier transform four orders of magnitude below the $k_1 = k_2 = 0$ component could theoretically be detected. Since all image intensities have transforms which go down as $1/k$ for large k , each order of magnitude corresponds to a decade of spatial frequency bandwidth. This demonstrates one important advantage of the light valve over the elastophotocathode devices. By using a very low dark signal detector as a separate entity, a far greater spatial bandwidth can be obtained. This also effects several other advantages. The thin film devices suffer from rather long rise time and fall time (approximately 1 ms) due to carrier effects, thus limiting their temporal bandwidth. In practice, this limits them to use with images which do not change significantly in less than a few milliseconds. The only time limitations on the light valve system are caused by the detector since the valve responds instantaneously to the light.

The calculations and estimates above do not include one important constraint in the design of the system. The transducers selected have fundamental frequencies of 40 MHz with bandwidths expected to be 15% . In order to perform baseband Fourier imaging (around $\bar{k} = 0$, as indicated in (7)), it is necessary to put the optical signal, $I(\bar{r})$, on a spatial carrier whose radian spatial frequency equals the spatial frequency of the 40 MHz acoustic wave [8]. Otherwise, the values of $|\bar{k}|$ will be so large that little information will be obtained since the acoustic system is centered at high spatial frequencies. The image is placed on a carrier by a sampling mask affixed to the valve. For a velocity of 5960 m/s at 40 MHz , the wavelength is $149 \mu\text{m}$ in both the x - and y - directions.

The quartz plate itself is $2.54 \text{ cm} \times 2.54 \text{ cm} \times 0.635 \text{ cm}$ thick. A calculation of the optical Rayleigh range

$$Z_R = \frac{\pi d^2}{\lambda} = 2.77 \text{ cm} \quad (8)$$

where d is the width of the sampling apertures ($149 \mu\text{m/s}$) shows that the image remains well

sampled throughout the optical path within the 0.635 cm thick plate.

Thus the intensity pattern exiting the valve sandwich (7) has only low frequency variation. Assuming a 20% acoustic bandwidth, the Rayleigh range will be at least one meter,

$$Z_{R1} = \pi \frac{(L/34)^2}{.63 \times 10^{-6}} = 2.78 \text{ m}. \quad (9)$$

Placement of an extended detector within one meter from the valve will insure proper operation including "local" detection of intensity and spatial integration.

Experimental Results

Four thin transducers with wrap-around electrodes were purchased and bonded to the quartz plate. After testing, two were removed and those contiguous plate edges sand blasted in order to produce travelling acoustic waves rather than standing waves. The placement of the transducers is shown in Fig. 2.

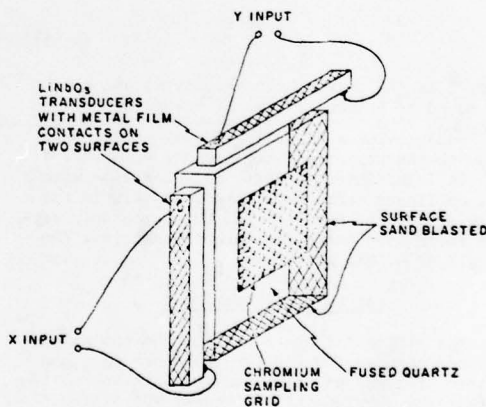


Fig. 2. The "light valve" with LiNbO_3 transducers and sampling grid.

The device is mounted in a holder with BNC connectors to facilitate the signal input to the transducers.

On one of the square faces a sampling grid was placed to shift the center of the Fourier space from zero to $f_x = 38.3 \text{ MHz}$ and $f_y = 38.3 \text{ MHz}$, which is in the center of the bandwidth of the transducers. The sampling grid dimensions are $1 \text{ cm} \times 1 \text{ cm}$.

The input light was from a 15 mW HeNe laser with a telescopic expander adjusted to give a beam diameter of 1.0 cm maximum at the device. The polarizers were set such that there was a minimum of light transmitted when no signal was applied to the transducers. The output was

detected by an EEG 585 photomultiplier and the output was displayed on a Textronix spectrum analyzer. This arrangement is shown in Fig. 1.

Standing Waves

Unfortunately, the sand blasting was not very effective and a strong pattern of discrete, equally spaced frequencies was detected. Since the valve was so long compared to acoustic wavelength, no two-dimensional modes were formed due to each transducer. Thus the system worked as expected, except for a rapid "sampling" of the transform space.

The bandwidth or extent of the signal peak can easily be calculated by

$$BW \approx \frac{v}{d} \quad (10)$$

where v is the velocity (5960 m/sec) and d is the beam diameter (.005 m in this case), giving the signal bandwidth as 1.2 MHz. The standing wave peaks are 0.12 MHz apart and have a bandwidth of 40 KHz. By pulse delay experiments it can be shown that the wave velocity is indeed

$$v = \frac{2\ell}{t} \quad (11)$$

where ℓ is the crystal size (.0254 m) and t is the round trip transit time of the pulse (8.4×10^{-6} sec) giving a velocity of 6047 m/sec, very close to the published longitudinal velocity.

It is of interest that, in accordance with (4), no linear terms were observed. Within the bandwidth of the detector (50 MHz), the only signals found were the difference frequencies. No signals at 40 MHz were seen.

Bar Pattern Experiment

The simplest image for which one can calculate and observe the Fourier transform is a bar pattern of light and dark stripes. If we consider that the wavelength is given by the distance from the center of one light band to the center of the next light band, then the frequency is given by

$$\Delta f = \frac{v}{\lambda_p} \quad (12)$$

where v_p and λ_p are the pseudo wave parameters. The actual frequency measured is then 38.3 MHz $\pm \Delta f$. The direction of \vec{k} from the center is the direction of a vector perpendicular to the bar pattern stripes. Thus one can rotate the image, follow the signal by changing the two frequencies, and transcribe a circle in Fourier space. Three different bar patterns or spatial periodic images were tried, and the longitudinal velocity of sound in the crystal is given as 5960 m/sec. Table I gives the wavelength and Fourier frequency for the patterns tried. Notice that the longitudinal wave velocity in fused quartz calculated

from this data agrees well with the value recorded in the literature.

Table I

spatial pattern	λ	Δf	$v = \lambda \Delta f$ (m/sec)
A	1.78×10^{-3} m	3.40 MHz	6052
B	3.64×10^{-3} m	1.634 MHz	5948
C	6.20×10^{-3} m	.961 MHz	5958

In Fig. 3 the circles represent the theoretical calculated value of Δf when the image is rotated about 360°. The crosses represent data taken at several selected angles for each spatial pattern.

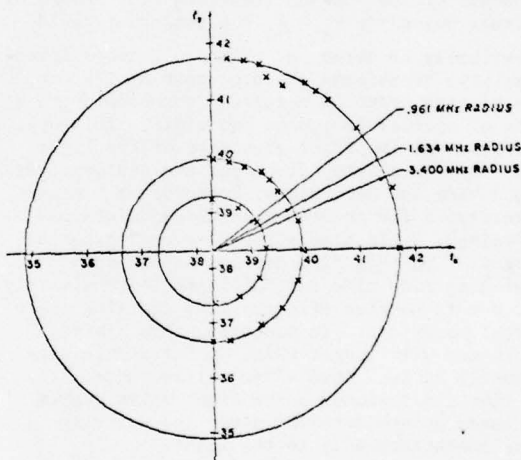


Fig. 3. The Fourier transform of several different bar patterns. The spatial wavelength corresponding to the Fourier frequencies are a) $\lambda = 6.20$ mm and $\Delta f = 0.961$ MHz; b) $\lambda = 3.64$ mm and $\Delta f = 1.634$ MHz and c) $\lambda = 1.78$ mm and $\Delta f = 3.40$ MHz.

Circular Pattern

Fig. 4 shows a circular aperture whose Fourier transform is given by

$$F(\vec{k}) = \frac{1}{2\pi} \int_{\text{area}} f(r, \theta) \exp(-j\vec{k} \cdot \vec{r}) d^2\vec{r} \quad (13)$$

$$f(r, \theta) = \begin{cases} 1 & b > r > a \\ 0 & \text{otherwise} \end{cases}$$

which then gives

$$f(k) = \frac{b^2 J_1(kb)}{kb} - \frac{a^2 J_1(ka)}{ka} \quad (14)$$

by choosing $b = 0.5$ cm and $a = 0.16$ cm a calculated minima for the transform is at 0.95 MHz in the radial direction from the center of the sampled k space. In Fig. 5, the solid circle represents the calculated transform and the crosses are the data points. The signal amplitude is very small and only a few dBm above the signal associated with the sinc function lobes of the aperture response.

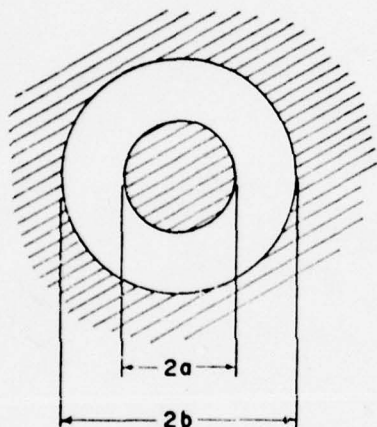


Fig. 4. The circular hole image with inner radius a and outer radius b .

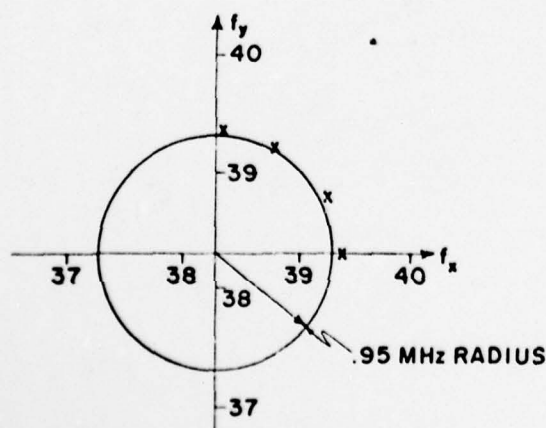


Fig. 5. The Fourier transform of the circular hole with $a = 1.6$ mm and $b = 5.0$ mm.

Conclusions

We have verified the two-dimensional pseudo beam steering effect by quantitative experiments in which Fourier spectra of a variety of images were obtained. We measured spatial frequencies and tracked them during rotation experiments over a full 360° .

Future improvements include further attempts to produce a travelling wave system by more effective sand blasting and through the addition of absorbing materials on the edges opposite the transducers.

Bibliography

1. C.S. Tsai, "Wideband Guided-Wave Acoustooptic Bragg Devices and Applications," 1975 Ultrasonics Symposium Proceedings, pp. 120-125.
2. G.S. Kino, "Acoustoelectric Interactions in Acoustic-Surface-Wave Devices," Proc. IEEE, Vol. 64, May 1976, pp. 724-748.
3. M. Luukkala, "Applications of the Acoustoelectric SAW Image Scanners," 1977 Ultrasonics Symposium Proceedings, pp. 165-170.
4. P. Kornreich, N.T. Yang, and S.T. Kowel, "A Direct Electronic Fourier Transform Device for Imaging," IEEE Proc. Letters, Vol. 61, August, 1973.
5. P.G. Kornreich, S.T. Kowel, D.J. Fleming, N.T. Yang, A. Gupta, and O. Lewis, "DEFT: Direct Electronic Fourier Transforms of Optical Images," IEEE Proceedings, Vol. 62, pp. 1072-1087, August, 1974.
6. S.T. Kowel, P.G. Kornreich, O. Lewis, A. Gupta, and R. Zawada, "Progress on Two-Dimensional Direct Electronic Fourier Transform (DEFT) Devices," 1974 Ultrasonics Symposium Proceedings, pp. 763-767.
7. S.T. Kowel, P.G. Kornreich, A. Mahapatra, B. Emmer, M. Mehter, and P. Reck, "The Vector Imaging Convolver," 1977 Ultrasonics Symposium Proceedings, pp. 715-720.
8. P.G. Kornreich, S.T. Kowel, K.W. Loh, A. Mahapatra, M. Mehter, and B. Emmer, "Imaging Without Raster Scanning" IEEE Trans. on Electron Devices, to be published.
9. S.T. Kowel, P.G. Kornreich, A. Mahapatra, D. Cleverly, B. Emmer, and R. Zawada, "Two-Dimensional Fourier Imaging of Light Using Acoustic Pseudo-Beam Steering," 1975 Ultrasonics Symposium Proceedings, pp. 136-140.
10. D.A. Pinnow, "Elastooptical Materials," Chapter 17 from Handbook of Lasers, R.J. Presley, Ed., The Chemical Rubber Co., Cleveland, Ohio, 1971.

APPENDIX IX.

IMAGE FEATURE ANALYSIS USING DEFT SENSORS

AIAA/NASA Conference on "Smart" Sensors
Hampton, Va./Nov. 14-16, 1978

Sponsored by—

American Institute of Aeronautics and Astronautics (AIAA)
NASA Langley Research Center (NASA)

78-1727

Image Feature Analysis Using Deft Sensors

S.T. Kowel, P.G. Kornreich, A. Mahapatra,
M. Mehter and T. Szebenyi, *Syracuse
University, Syracuse, N. Y.*

AIAA/NASA Conference on "Smart" Sensors

Hampton, Va./Nov. 14-16, 1978

For permission to copy or republish, contact the American Institute of Aeronautics and Astronautics,
1290 Avenue of the Americas, New York, N. Y. 10019.

IMAGE FEATURE ANALYSIS USING DEFT SENSORS

S.T. Kowel, P.G. Kornreich, A. Mahapatra, M. Mehter, and T. Szebenyi

Department of Electrical and Computer Engineering, Syracuse University
Syracuse, New York 13210Abstract

The DEFT sensor makes use of a photoconducting film deposited on a piezoelectric substrate. Two orthogonally directed surface acoustic transducers modulate the image-induced charges, creating an electronic signal of the general form

$$i(t) \propto \iint I(x, y) f_1(x \pm v_1 t) f_2(y \pm v_2 t) dx dy$$

where $i(t)$ is a current detected by interdigital contacts laid over the film, $I(x, y)$ is the image intensity, and $f_1(t)$ and $f_2(t)$ are electronic signals used to generate the acoustic waves. When $f_1(t)$ and $f_2(t)$ are sinusoids, $i(t)$ represents the two-dimensional Fourier transform of the image intensity. Thus the sensors are called Direct Electronic Fourier Transform devices (DEFT).

Since the Fourier transform is available, realtime processing functions can be performed, such as feature tracking and focussing.

Two interdigital transducers, each parallel to one of two orthogonal edges of the square sensor, are used for the generation of surface acoustic waves. The sensor area is overlaid by a thin polymer insulating film after the contacts are fabricated. An array of aluminum film squares deposited on the polymer film form a monolithic shadow mask. This shadow mask provides the sampling of the image in the x-direction. The image is sampled in the y-direction by the interdigital contact pattern.

Our previous devices had an externally mounted shadow mask [3,5]. Since the mask was spaced about 50 μm from the device, imaging with a lens was difficult. The light rays incident at an angle other than 90° to the plane of the device would undercut the shadow mask.

The present monolithic device eliminates this difficulty.

1. Introduction

We have succeeded recently in fabricating monolithic direct electronic Fourier transform (DEFT) imaging sensors. We present here the results of tests conducted with those devices. We also present contrast and Fourier space raster scan data previously not reported. In previous publications [1,2,3,4,5] we have reported data taken with devices having an externally mounted sampling grid, rather than the present monolithic sampling mask.

A DEFT device is an electronic image sensor. The output of the device is a sinusoidal electrical current. The amplitude of the current is proportional to the amplitude of the Fourier transform components of the two-dimensional image, and the phase of the current is proportional to the phase of the Fourier transform components of the image.

One embodiment of the device is shown in Fig. 1. The image sensor consists of a double layered CdS film [6] deposited on a z-cut LiNbO_3 substrate. The metal contacts, consisting of an Al/In film sandwich in the form of an interdigital pattern, are deposited onto the CdS film. This pattern permits the collection of the total photocurrent over the area of the CdS film. Indium is used as the contact material. It is our experience that it makes ohmic contact to CdS and aluminum provides better longitudinal conduction.

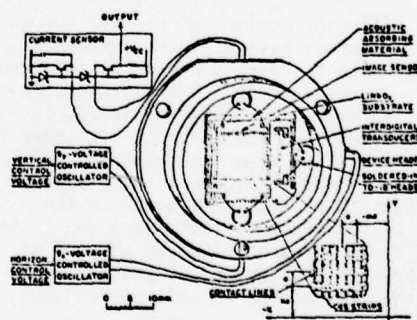


Fig. 1. Photoconducting DEFT sensor mounted in a header. Note the image sampling arrangement shown in the lower right corner.

2. Device Operation

The DEFT device derives an electrical signal representative of Fourier components by modulating the photo-generated electrons with electric fields associated with the traveling surface acoustic waves in the LiNbO_3 substrate. This modulation,

as demonstrated by M. Luukkala [7], E.S. Kohn [8], and by us [1,9] is proportional to the square of the SAW electric field E_z . A detailed description of the tensor nature of electrophotoconductivity is given elsewhere [1,4]. We have shown that the deposited contacts detect a current proportional to

$$i(t) \propto \iint dx dy E_z^2(x, y, t) I(x, y) \quad (2.1)$$

where $I(x, y)$ is the image intensity, x and y are the coordinates on the film, and E_z is the electric field perpendicular to the plane.

Since,

$$E_z = E_{1z} \cos(\omega_1 t - k_1 x) + E_{2z} \cos(\omega_2 t - k_2 x) \quad (2.2)$$

where E_{1z} , ω_1 , k_1 refer to the x -directed wave and E_{2z} , ω_2 , k_2 refer to the y -directed wave,

E_z^2 contains a term of the form

$$\begin{aligned} E_{zd}^2 &\propto E_{1z} E_{2z} \cos[(\omega_1 - \omega_2)t - (k_1 x + k_2 y)] \\ &\propto E_{1z} E_{2z} \cos[(\omega_1 - \omega_2)t - \vec{k} \cdot \vec{r}] \end{aligned} \quad (2.3)$$

Using this in Equation 2.1 gives,

$$i(t) \propto \int d^2 \vec{r} I(\vec{r}) \cos[(\omega_1 - \omega_2)t - \vec{k} \cdot \vec{r}] \quad (2.4)$$

Thus, the component of the current at the difference frequency $(\omega_1 - \omega_2)$ is indeed proportional to the Fourier transform of the function $I(\vec{r})$. By varying the frequencies ω_1 and ω_2 one can vary \vec{k} and probe different regions of Fourier space. Since the transducers have a finite bandwidth they are only able to sweep a region of frequency-space centered around their center frequencies. However, all optical images have their Fourier spectrums centered around base-band. In order to shift this information from base-band to the region scanned by the transducers the image has to be sampled. This sampling is done in the x -direction by the metal contact lines and in the y -direction by an array of aluminum squares as explained earlier. The region of Fourier space scanned by the transducers we call the reduced Fourier space.

3. Experimental Arrangement

The device and its associated signal detecting circuitry is mounted in a camera box. A low pass filter with a cutoff frequency of 6 MHz and providing an attenuation of 80 db at 30 MHz is used for the detection of the difference frequency component. The characteristic impedance of the filter is 15 Ohms which matches the input impedance of the broad band current-sensing amplifier. A low input impedance is required of the device shunt capacitance (325 pF).

For some experiments, a peak detector is used at the output of the amplifier.

Each transducer is tuned by a series inductance to match its impedance to the impedance of the driving source. The transducer that generates the x -propagating acoustic wave is driven by a H.P. 8601A sweep oscillator. The input voltage to this transducer is swept in a continuous fashion in frequency over the bandwidth of the transducer centered at the center frequency of the transducer.

The other transducer is driven by a H.P. 3200A VHF oscillator. The frequency of the voltage applied to the transducer generating the y -propagating wave could, thus, only be changed manually. This arrangement results in raster scanning of Fourier space.

The incoming light is imaged on the device by means of a 50 mm focal length $f/1.8$ lens. The image is either front or back projected onto a screen facing the DEFT camera. A slide projector is used to display the image on the screen.

Oscilloscope pictures as shown in Figs. 2 and 3 are generated by selecting a frequency for the y -transducer driving voltages and sweeping the frequency of the voltage applied to the x -transducer about 100 times per second. The horizontal deflection of the oscilloscope is controlled by a saw-tooth voltage output of the sweep generator. The amplitude of this saw-tooth voltage is proportional to the frequency of the voltage applied to the x -transducer. Thus, the horizontal axis in these pictures is the x -frequency f_x . The peak detected output voltage of signal amplifier is applied to the vertical input of the oscilloscope.

A Polaroid picture is taken of this oscilloscope trace.

Next, the y -transducer driving frequency is set to a new value, the oscilloscope trace is moved up. The same Polaroid picture is exposed again to the resulting oscilloscope trace.

These steps are repeated until the desired range of y -frequencies, f_y , is obtained.

The contrast measurements were obtained without the peak detector. The peak detector tends to clip the lower portion of the signal.

4. Transforms of Test Patterns

In this section we present data to show that the sensor is indeed capable of generating two-dimensional optical images. Consider the response of the sensor to uniform light illustrated in Fig. 2. In this figure f_y is kept fixed at

29.6 MHz while f_x is swept from 27 MHz to 30 MHz.

The peak at the center is just the main lobe of the sinc function which is the Fourier transform of such a pattern. Furthermore, if the aperture of the sensor is L , one expects the width of the main lobe of the sinc function in frequency space to be $\Delta\omega = \frac{v}{L}$, where v is the velocity of the surface acoustic waves. Using $L = 12.7$ mm and $v = 3820$ m/s we expect $\Delta\omega$ to be 300 kHz. From Fig. 2 the width of the main lobe is indeed of this order of magnitude.

Consider next the signal for a periodic bar pattern consisting of light and dark lines parallel to the y axis. The Fourier transform of such a pattern should show a peak at the center of the reduced Fourier space plus two peaks on the f_x



Fig. 2. The magnitude of the output signal for uniform illumination of the sensor.

axis located equidistant from the central peak. This is exactly what we observe as illustrated in Fig. 3. The two peaks are separated from the central peak by a frequency difference of $\Delta f = \pm 0.8$ MHz. This coupled with the periodicity of the pattern, $\lambda = 4.55$ mm, yields a surface wave velocity of

$$v = 2\pi\Delta f\lambda = 3640 \text{ m/s}$$

This agrees well with the velocity of surface waves recorded in the literature for the crystal-cut we used.

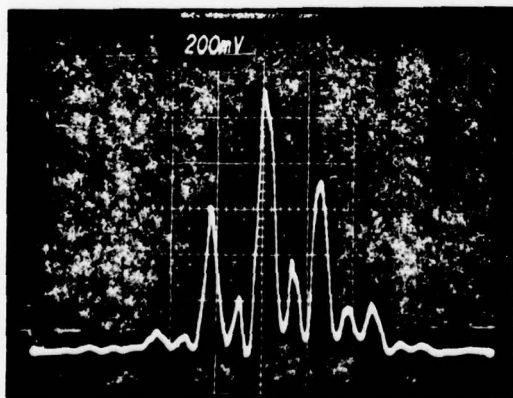


Fig. 3. The magnitude of the output signal with the sensor illuminated by a periodic bar pattern consisting of light and dark lines parallel to the y axis.

These and other similar data reported elsewhere [10] convince us that our sensor is capable of measuring arbitrary, two-dimensional Fourier transforms of optical images.

5. Focus Detection

The focus detection experiments were done by

imaging a periodic grid pattern on a sensor and monitoring the fundamental Fourier frequency of this pattern. The object was placed at a distance of 0.9 m from the lens. The magnitude of the signal was noted as the lens was focussed through this distance. The experiment was repeated at different f-stops and the results are illustrated in Fig. 4. As expected, the camera is more sensitive to focus at smaller f-stops; that is, at larger apertures.

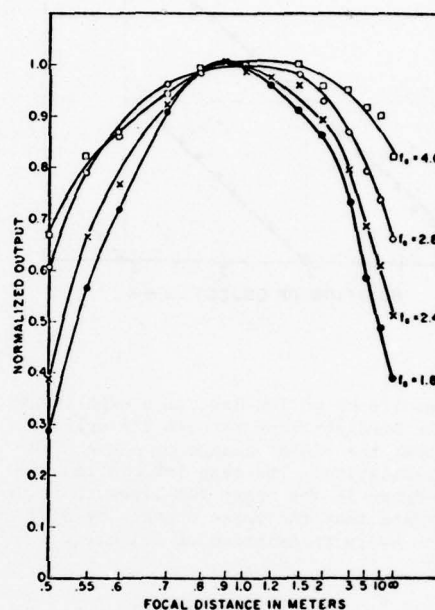


Fig. 4. Results of focus detection experiments. The object is kept at a distance of 0.9 m. The f-stop for each curve is specified by f_s .

6. Motion Detection

The use of our camera for motion detection utilizes the spatial shifting theorem of Fourier transforms. This theorem states that a pure translation of a picture in real space leaves the magnitude of Fourier components unchanged but alters their phase by an amount proportional to the magnitude of the translation. Therefore, by monitoring the phase of a Fourier component one can detect any motion of the picture. Indeed, because of the device being a two-dimensional Fourier transformer, one can also determine the direction of motion.

To test this we again projected a periodic grid pattern on the sensor and monitored the phase of its fundamental Fourier component. The results are shown in Fig. 5. We see that the phase changes linearly and undergoes a 360° shift at 2.1 mm. This is exactly the periodic length of the grid image on the sensor.

Though we do not demonstrate its use here, we have developed elsewhere [11] a simple algorithm which yields the velocity as a function of time, of an object moving against a complicated

background.

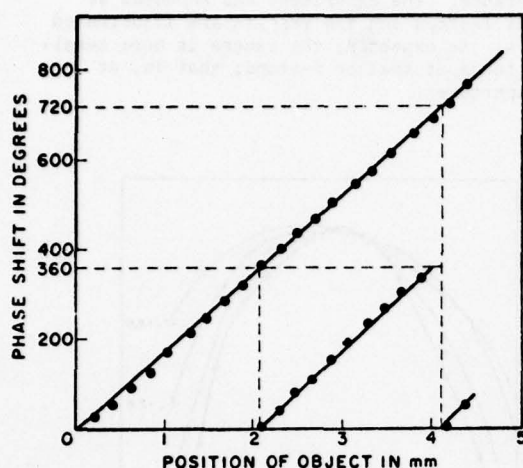


Fig. 5. Results of motion-detection experiments. The straight line through the origin shows the linear change of phase with translation. The same information is redrawn in the other two lines to illustrate that the phase changes by 360° for every translation of 2.1 mm.

7. Contrast Measurements

The contrast measurements were made with the aid of two slide projectors. Each projector was equipped with a variable iris so that the light intensity output could be varied. A pattern of equally spaced alternate dark and light bars was displayed on the screen by the use of one projector. The other projector was used to control the background illumination of the screen. The camera was placed to face the screen. The lens was adjusted to focus the image, displayed on the screen, onto the DEFT device.

The experiment was conducted by varying both background illumination and the light intensity of the bar pattern in such a way as to keep the total light of the image constant. A pattern was chosen in such a way that there was an equal number of N of darker and brighter lines. The output of the device along the k_x axis can be shown to be,

$$i_{\text{sig}} \propto \frac{(I_s - I_B)F(k_x) + I_B G(k_x)}{I_B + I_s} \quad (7.1)$$

where I_s is the light intensity of the bright lines, I_B is the background light intensity, $F(k_x)$ is a spacial frequency function exhibiting two symmetric peaks along the k_x axis associated with the periodic bar pattern, and $G(k_x)$ is a sinc-like function associated with the average

illumination of the device.

All measurements were made at constant spacial frequency k_x at a peak of the function $F(k_x)$. The measurements were made at a sufficiently high spacial frequency so that the amplitude at k_x of the sinc function $G(k_x)$, associated with the aperture, was small enough to be neglected. (See Fig. 2 for the extent of aperture sinc function.)

In this case equation 7.1 reduces to

$$i_{\text{sig}} \propto F(k_x)C \quad (7.2)$$

where the contrast C is defined as

$$C = (I_s - I_B)/(I_s + I_B) \quad (7.3)$$

We have measured the contrast response of the device. The results of the measurements are shown in Fig. 6. Indeed, the output of the device is a linear function of the contrast C .

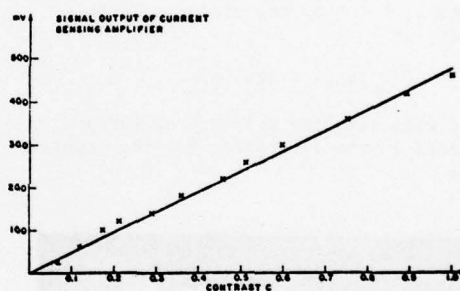


Fig. 6. The contrast response of the device. As expected, the response is linear.

8. Conclusion

In this communication we have demonstrated some of the capabilities of our new monolithic DEFT sensor. We have overcome some of the difficulties associated with the external sampling grid of our previous sensor. We are now able to image a light pattern by means of a highly converging lens on the device. This was difficult to do with the external sampling grid.

We have demonstrated the feasibility of using this device for real-time processing functions such as focussing and feature tracking.

We are now working on a sensor with much higher resolution and moderate low light level capability. We also intend to operate the sensor in a line scan mode. This line scan mode could be especially useful for reading out infrared sensitive diodes. We hope to extend our work to devices using infrared sensitive materials.

Acknowledgements This work was supported by the Night Vision and Electrooptics Laboratory, Fort Belvoir, Virginia.

References

1. S.T. Kowel, P.G. Kornreich, A. Mahapatra, D. Cleverly, B. Emmer, and R. Zawada, "Two-Dimensional Fourier Imaging of Light Using Acoustic Pseudo Beam Steering," 1975 Ultrasonics Symposium Proceedings, pp. 136-140.
2. S.T. Kowel, P.G. Kornreich, A. Mahapatra, and B. Emmer, "Experimental Confirmation of Two-Dimensional Acoustic Processing of Images," 1976 Ultrasonics Symposium Proceedings, pp. 668-672.
3. S.T. Kowel, P.G. Kornreich, A. Mahapatra, M. Mehter, and P. Reck, "The Vector Imaging Convolver," 1977 Ultrasonics Symposium Proceedings, pp. 715-720.
4. S.T. Kowel, P.G. Kornreich, K.W. Loh, A. Mahapatra, M. Mehter, B. Emmer, P. Reck, W.A. Penn, "Two-Dimensional Transform (DEFT) Devices: Analysis, Fabrication and Evaluation," Report DAAG53-76-C-0162 (1976), prepared for U.S. Army Night Vision Laboratory, Fort Belvoir, VA 22060.
5. S.T. Kowel, P.G. Kornreich, K.W. Loh, A. Mahapatra, M. Mehter, P. Reck, and B. Emmer, "Imaging Without Spacial Raster Scanning," submitted for publication in the IEEE Transactions on Electron Devices, to be published.
6. P.G. Kornreich, A. Mahapatra, S.T. Kowel, K.W. Loh, and B. Emmer, "Double-Layered Polycrystalline Cadmium Sulfide on Lithium Niobate," J. Appl. Phys., Vol. 49, pp. 2443-2448, (1978).
7. M. Luukkala, P. Merilainen, and K. Saarinen, "Acousto-Resistive Effects in Thin Films of CdSe/LiNbO₃ Delay Line System," 1974 Ultrasonics Symposium Proceedings, pp. 345-347.
8. E.S. Kohn and M. Lampert, Phys. Rev. B4, p. 4479 (1971).
9. A. Mahapatra, P.G. Kornreich, and S.T. Kowel, "Strain Induced Modulation of Photoconductivity in Thin Polycrystalline Films of Cadmium Sulfide," accepted for publication in the Sept., 1978, issue of the Phys. Rev., Vol. B18.
10. P.G. Kornreich, S.T. Kowel, A. Mahapatra, and M. Mehter, "Monolithic Two-Dimensional Fourier Transformer," Proceedings of the Optical Computing Conference, London, 1978.
11. S.T. Kowel, P.G. Kornreich, Owen Lewis, and Frank Kirschner, "Passive Detection of Motion Transverse to the Optical Viewing Axis," IEEE Trans. Instrumentation and Measurement, September, 1975.

APPENDIX X.

A PROGRAMMABLE, MULTI-FUNCTION PROCESSOR

S.P.I.E. Technical Symposium East,
April 1979, Washington, D.C.

A PROGRAMMABLE, MULTI-FUNCTION PROCESSOR

Stephen T. Kowel, Philipp G. Kornreich, A. Mahapatra, T. Szebenyi, A. Nouhi
 Department of Electrical and Computer Engineering*
 Syracuse University
 Syracuse, NY 13210
 and
 Samuel Craig
 DEPT Laboratories, Inc.**
 East Syracuse, NY 13057

Abstract

A new two-dimensional DEFT sensor (for Direct Electronic Fourier Transform) for multi-processing will be described. Operating at a center frequency of 100 MHz, it is capable of resolving 1800 unique spatial Fourier image components in a random access mode. As a Fourier transformer it can identify vector spatial frequencies, their amplitude and phase. By suitable change of input functions, the device can be operated as a spatial raster scanner, Hadamard transformer, matrix multiplier, or convolver. The device achieves this flexibility by virtue of producing the spatial integral of the product of two electronic signals with an optical signal.

1. Introduction

We have succeeded recently in fabricating monolithic direct electronic Fourier transform (DEFT) imaging sensors. We here present the results of tests conducted with those devices. We also present Fourier space raster scan data previously not reported. In previous publications [1,2,3,4,5] we have reported data taken with devices having an externally mounted sampling mask [6].

A DEFT device is an electronic image sensor. The output of the device is a sinusoidal electrical current. The amplitude of the current is proportional to the amplitude of the Fourier transform components of the two-dimensional image, and the phase of the current is proportional to the phase of the Fourier transform components of the image.

The device has three input ports; two electronic, one optical; and one electronic output. The optical input is usually considered stationary, while the electronic signals used to excite the surface waves are time-varying.

Such devices have considerable flexibility. By appropriate choice of the inputs, a large class of signal and optical processing functions can be performed. We shall describe a prototype system, currently used to raster scan the two-dimensional spatial Fourier transform of the optical intensity. It could be expanded to provide direct video scanning, Hadamard transformation, etc.

As a signal processing device, it can be operated to obtain generalized matrix inner products of digital signals.

Recently, an alternative structure also capable of two-dimensional processing has been described [7]. It is based on a Si diode-array separated-medium surface-wave convolver, and has been used to line scan images.

One embodiment of the device is shown in Fig. 1. The image sensor consists of a layered CdS film deposited on a z-cut LiNbO₃ substrate. The metal contacts, consisting of an Al/In film sandwich in the form of an interdigital pattern, are deposited onto the CdS film. This pattern permits the collection of the total photocurrent over the area of the CdS film. Indium is used as the contact material. It is our experience that In makes ohmic contact to CdS and aluminum provides better longitudinal conduction. Two interdigital transducers, each parallel to one of two orthogonal edges of the square sensor, are used for the generation of surface acoustic waves. The sensor area is overlaid by a thin polymer insulating film after the contacts are fabricated. An array of aluminum film squares deposited on the polymer film form a monolithic shadow mask. This shadow mask provides the sampling of the image in the x-direction. The image is sampled in the y-direction by the interdigital contact pattern.

Previous devices had an externally mounted shadow mask [3,5]. Since the mask was spaced about 50 μ m from the device, imaging with a lens was difficult. The light rays incident at an angle other than 90° to the plane of the device would undercut the shadow mask.

The present monolithic device eliminates this difficulty, as well as providing a stronger mechanical unit.

* Research leading to this paper supported by U.S. Army Night Vision and Electrooptics Laboratory, Ft. Belvoir, VA.

** Work supported in part by U.S. Army Engineer Topographic Laboratories, Ft. Belvoir, VA.

2. Device Operation

The DEFT device derives an electrical signal representative of Fourier components by modulating the photo-generated electrons with electric fields associated with the travelling surface acoustic waves in the LiNbO_3 substrate [6].

The interdigital contact pattern, in conjunction with the aluminum shadow mask, divides the CdS film into an array of squares of photoconductive material. Thus the contact pattern also serves as part of a sampling grid that translates the image onto a high spatial carrier frequency. This, as will become evident, is necessary since the transducers have a limited bandwidth centered at a high temporal frequency.

The normal component E_z of the electric field associated with the two acoustic waves travelling at right angles to each other is

$$E_z = E_x \cos(\omega_x t - k_x x) + E_y \cos(\omega_y t + k_y y) \quad (2.1)$$

where ω_x , k_x and E_x are the temporal and spacial angular frequencies, and the normal component of the electric field associated with the SAW propagating in the x-direction, and ω_y , k_y and E_y are similar quantities associated with the y-propagating acoustic wave.

Consider a square of CdS film at the m,n position. The conductance g_{mn} of the mn'th CdS square is

$$g_{mn} = g_L I_{mn} + g_{LE} E_z^2 I_{mn} \quad (2.2)$$

where I_{mn} is the average light intensity incident on the mn'th square of photoconducting material, g_L is the ordinary photoconductance, g_{LE} is the electrophotoconductance of a square of CdS film, and E_z is the SAW electric field component normal to the plane of the film.

The photocurrent i_{mn} in the mn CdS square due to a d.c. voltage V_0 applied across the contacts is

$$i_{mn} = g_{mn} V_0 \quad (2.3)$$

As we have noted, the conductance-modulating electric field component E_z associated with the acoustic waves is in the form of two orthogonally travelling waves, Equation 2.1. The modulation of the photoconductance, as expressed by Equation 2.2 is proportional to the square of this field component. Therefore the photocurrent i_{mn} will contain components oscillating at various frequencies. The photocurrent component oscillating with the difference frequency $\omega_x - \omega_y$ is also a sinusoidal function of the vector sum of the wave vectors k_x and k_y , of the individual surface acoustic waves

$$\bar{k} = k_x \hat{x} + k_y \hat{y} \quad (2.4)$$

We have thus created a conductivity "wave" propagating with a wave vector \bar{k} which is the vectorial sum of the original SAW wave vectors. The SAW wave vectors k_i are related to the angular frequency ω_i of the transducer driving voltages by a linear dispersion relation

$$k_i = \omega_i / v_s \quad i = x, y \quad (2.5)$$

where v_s is the surface wave velocity under the CdS film, 3759 m/sec in our case. By controlling the frequencies of the transducer driving voltages we can "steer" the conductivity wave.

The circuit that detects the output current of the device is arranged, therefore, to detect only signals oscillating at the difference frequency $\omega_x - \omega_y$. Thus, we are only interested in the current component i_{sig} oscillating at the difference frequency and the d.c. component $i_{d.c.}$. By substituting Equations 2.1 and 2.2 into Equation 2.3 and summing all CdS squares we obtain for the two current components of interest

$$i_{d.c.} = [g_L + (g_{LE}/2)(E_x^2 + E_y^2)] V_0 \sum_{m=-N}^{m=N} \sum_{n=-N}^{n=N} I_{mn} \quad (2.6)$$

and,

$$i_{sig} = 2g_{LE} E_x E_y V_0 \sum_{m=-N}^{m=N} \sum_{n=-N}^{n=N} I_{mn} \exp j(k_x m a + k_y n a) \quad (2.7)$$

where a is the spacial period of the CdS squares as shown in Fig. 1. Since the image is sampled we can now define a reduced wave vector with components q_i ($i = x, y$)

$$k_i = q_i + (2\pi/a) \quad (2.8)$$

Substituting Equation 2.8 into Equation 2.7 brings the image back to "base band" in the reduced Fourier space,

$$i_{sig} = 2g_{LE} E_x E_y V_0 \sum_{m=-N}^{m=N} \sum_{n=-N}^{n=N} I_{mn} \exp j(q_x m a + q_y n a). \quad (2.9)$$

The current sensing electronics keep the d.c. photocurrent constant rather than keeping the d.c. voltage V_0 constant. This makes the output current less susceptible to ageing, temperature, or other changes of the CdS films. Solving Equation 2.6 for V_0 and substituting the result for V_0 into Equation 2.9 we obtain for the signal

$$i_{sig} = A i_{d.c.} \sum_{m=-N}^{m=N} \sum_{n=-N}^{n=N} I'_{mn} \exp j(q_x m a + q_y n a) \quad (2.10)$$

where

$$A = 2(g_{LE}/g_L) E_x E_y / [1 + (g_{LE}/2g_L) (E_x^2 + E_y^2)] \quad (2.11)$$

and the average normalized light intensity I'_{mn} incident on the mn 'th CdS square is

$$I'_{mn} = I_{mn} / \sum_{m=-N}^{m=N} \sum_{n=-N}^{n=N} I_{mn}. \quad (2.11)$$

Thus, the signal current i_{sig} , as shown in Equation 2.10 is proportional to the Fourier transform of the normalized sampled image I' .

3. General Signal Processing

In order to understand the flexibility inherent in the DEFT sensor, we will describe the Hadamard transform technique.

The Hadamard transform matrix T of a sampled image represented by a matrix I is given by the following similarity transformation

$$T = W I W \quad (3.1)$$

where W is a matrix consisting of normalized Walsh functions ordered by sequency and alternating in symmetry. We note that such a Walsh function matrix is equal to its own inverse.

Let us now compare the output of a DEFT device driven by circuits as shown in Fig. 2 to the above Hadamard transformation. The output signal current of a DEFT device at the temporal radian sum frequency $\omega_1 + \omega_2$ is given by

$$i_{SIG} = \delta \sum_{n=0}^{n=N} \sum_{m=0}^{m=N} I_{mn} E_x(t - \frac{na}{v}) E_y(t - \frac{mb}{v}) \times \exp j(na q_x + mb q_y) \quad (2.2)$$

where δ is a constant associated with device geometry and material properties, I_{mn} is the light intensity of the mn 'th image point, q_x and q_y are the components of the reduced wave vector, a and b are the spacial periods in the x and y direction respectively of the image sampling grid, and E_x and E_y are the phasor electric fields associated with the travelling acoustic waves. Here v is the velocity of the acoustic surface waves.

The phasors, E_x and E_y , must incorporate the forms of Walsh functions. This is achieved by modulating the phase of the sinusoidal transducer driving voltages with Walsh functions as shown schematically in Fig. 3. At one instant of time the electric field phasor E_x will be in the form of the k 'th Walsh function across the sensor in the x direction and the electric field phasor E_y will be in the form of the l 'th Walsh function along the y direction. We sample the output of the device by means of the sampling gate at this instant of time to obtain the kl 'th component of the Hadamard transform matrix T

$$T_{kl} = i_{kl, SIG} = A \sum_{n=0}^{n=N} \sum_{m=0}^{m=N} I_{mn} E_x^{kn} E_y^{lm} = E_x I E_y \quad (3.3)$$

where we have chosen the frequencies of the transducer driving voltages such that

$$q_x = 0; q_y = 0 \quad (3.4)$$

and E_x^{kn} , E_y^{lm} are the instantaneous values of the electric phasors E_x and E_y at the time the output signal is sampled.

We see that Equations 3.1 and 3.3 are similar. Here E_x^{kn} is the k 'th Walsh function with n as the discrete spacial variable.

Thus the DEFT device can be used as a Hadamard image transformer. Indeed it can be used to point scan an image.

For example, let

$$\begin{aligned} E_x &= \delta(t - \frac{x}{v}) \\ E_y &= \delta(t - \frac{y}{v} + \phi) \end{aligned} \quad (3.5)$$

then we can rewrite Equation (2.7) as

$$i_{sig} = \int \int dx dy I(x, y) E_x(t - \frac{x}{v}) E_y(t - \frac{y}{v}) \quad (3.6)$$

yielding with Equation (3.5)

$$i_{sig}(t) = I(vt, vt + v\phi) \quad (3.7)$$

so that the signal output is proportional to the image intensity along a 45° diagonal line. By changing the relative delay ϕ between the impulses, any such line of the image can be accessed.

The band width is limited by the lowest transducer driving frequency ω_i ($i=1$ or 2) and the band width of the transducer. It is usually the transducer bandwidth that is the limiting factor. As a spacial raster scanner, the spatial resolution is limited by the length of the "impulse."

4. Programmed Operation

The large amount of data which is potentially available from the DEFT sensor (i.e. 1800 unique complex spatial frequency samples with the 100 MHz device) warrants a capability for automatic control of the sensor. To that end, we have developed an interface between a simple 6800-based microcomputer system and a small image processing module containing a 30 MHz DEFT sensor and a minimum of peripheral circuitry. Even this most basic system offers a great deal of flexibility in probing the two-dimensional Fourier transform plane of an image and processing the resulting data.

The computer/sensor interface consists of means for setting the frequencies of the two surface-acoustic waves generated in the device, and for converting the amplitude of the resulting output to digital form. For the first function, two digitally controlled frequency synthesizers are connected to the computer. The synthesizers generate the two acoustic drive signals for the sensor, so that any point in the spatial frequency plane can be examined under program control.

To examine the entire two dimensional Fourier transform, the transducer frequencies can be stepped sequentially in a raster scan fashion, and at each step, the detected output of the sensor can be sampled and converted to a digital value. These values are stored in read/write memory. After all values have been obtained, the data can be processed and displayed or used in some other way.

Of prime significance here is the fact that the computer does not perform the Fourier transform; the data samples from the sensor are themselves the desired Fourier components. The computer is responsible only for controlling the sensor and keeping track of the data it produces. A relatively simple microcomputer system is well-suited to these tasks.

The most basic function of the computer-controlled sensor is for the display of the magnitude of the Fourier transform of an image's intensity. Our micro-computer system has two analog outputs which are used to produce a display on a conventional laboratory oscilloscope. The display is isometric, consisting of 32 horizontal lines, each displaced horizontally in proportion to its vertical position. The horizontal displacement tilts the raster so that the perimeter of the display is a parallelogram. Signal magnitude is indicated by vertical displacement, and in addition the intensity of the display is modulated in proportion to the slope of each raster line. This technique produces a pseudo-three-dimensional appearance which we feel is subjectively more appealing than a rectangular raster with intensity modulation alone.

Because the computer takes 23 microseconds to output each element in the display, the number of resolvable elements has been limited to 1024 to produce a frame rate of about 40 per second, so that flicker will not be too noticeable. In a more complex system, a display generator could be used to allow higher resolution without flicker. The display generator would be able to refresh the display at a higher rate, not limited by the cycle time of the computer. However, even with its rather limited resolution, the present display is a more effective way to examine the output of the DEFT sensor than any method we have used previously.

As presently programmed, the display can show any square area in the Fourier transform plane which is designated by an acoustic frequency span of 3.1 MHz in both the x- and y- directions. The exact location of the displayed area can be specified by entering the acoustic frequencies at the lower left hand corner by means of the microcomputer terminal keyboard.

With a simple bar pattern used as a test image, the display shows the positive and negative spatial frequency peaks on each side of the peak at the origin, as Fig. 4 shows. Photographing the display eliminates the problem of flicker, so the resolution was increased to 64 lines of 64 elements each. Rotation of the bar pattern produces a corresponding rotation of the two peaks about the origin. Heretofore, it has been possible to examine all

three peaks only when the bars were parallel to one of the acoustic axes.

In order to improve the quality of the data which the display program gathers automatically from the DEFT sensor, a simple filter subroutine was added to the program. The subroutine takes 256 separate samples of the sensor's detected output and reports their mean. This process aids in rejection of interference which is always present from a 5 kW AM broadcast station about a half-mile away.

The existing display program requires only a little more than 2K bytes of memory for data storage and less than 600 bytes for the program.

We expect this display to be an effective method for investigating the spatial frequency characteristics of real images, and for automated testing of newly fabricated DEFT devices. A sensor with 30 MHz acoustics is being used at present in the system for convenience, but acoustic frequencies up to 160 MHz can be accommodated without any change in the hardware, and with only minor software revisions.

In addition to the display function, computer control of the sensor would allow the searching and tracking of specific components of a Fourier transform. Another possibility would be the tabulation and presentation of the statistics of the spatial frequency data. Since the processor is not burdened with the computation of the Fourier transform, it is free to carry out a variety of other tasks.

5. Experimental Results with a "100 MHz" Sensor

We have succeeded in fabricating a sensor whose nominal center frequency is 100 MHz. In fact, it was designed to have different center frequencies in each direction so that the center of the image Fourier space would be along one edge rather than at the center of the acoustic space. Thus all Fourier components would be unique. Previous devices "wasted" half the space, yielding positive and negative frequencies.

For simplicity, this device was first operated as a one-directional sensor. Two adjacent transducers were excited, rather than two orthogonal transducers. The surface acoustic waves travelled parallel to the sensor contacts, and no monolithic pedestal sampling was required. In this case, the difference wavevector $k_{1x} - k_{2x}$ corresponds to the difference temporal frequency $\omega_1 - \omega_2$.

Time has permitted only simple measurements, which are very encouraging. Fig.5 shows a graph of measured temporal difference frequency versus number of light bars per cm. projected on the sensor. The slope of this line is quite constant. From this data the surface wave velocity is inferred to be 3500 m/sec., in good agreement with theory for this z-cut LiNbO_3 . Data was in fact obtained corresponding to spatial frequencies of up to 50 line pairs/cm.

We hope to evaluate a two-dimensional version of this sensor shortly. It should be capable of resolving 2500 data points with appropriate transducer matching and synchronous output detection.

The major difficulty in fabricating DEFT sensors at frequencies higher than 30 MHz in overcoming the high acoustic loss in the CdS film. This was achieved by going to a thinner film ($\approx .5\mu\text{m}$) and by evaporating thicker transducer metallization to improve the wide aperture transducers.

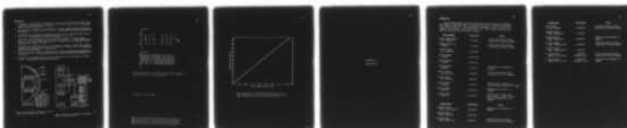
6. Conclusions

We have shown the feasibility of the 100 MHz sensor by evaluating a one-directional version capable of resolving 50 line pairs per cm. Considerable effort was required to obtain good performance, since acoustic losses were quite severe in the first prototypes. Thinner CdS films and thicker transducers reduced insertion loss between two parallel transducers separated by the sensor area to about 25 db, without tuning.

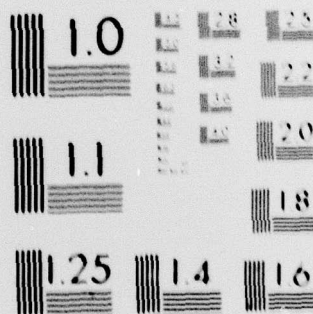
The programmable driver-detector system permits quasi-real time operation of the sensors and the isometric display of the Fourier space. Further work is required to program other decompositions, such as Hadamard, spacial raster scanning, etc. This capability, combined with a two-dimensional beam-steered device will provide great flexibility in image evaluation and processing.

AD-A075 373 SYRACUSE UNIV NY DEPT OF ELECTRICAL AND COMPUTER EN--ETC F/G 17/8
DEFT: ADVANCED STRUCTURES AND APPLICATIONS.(U)
JUN 79 S T KOWEL, P G KORNREICH, A MAHAPATRA DAA653-76-C-0162
UNCLASSIFIED TR-79-12 NL

2 OF 2
AD
A075373



END
DATE
FILMED
11-79
DDC



MICROCOPY RESOLUTION TEST CHART
NATIONAL BUREAU OF STANDARDS-1963-A

References

1. S.T. Kowel, P.G. Kornreich, A. Mahapatra, D. Cleverly, B. Emmer, and R. Zawada, "Two-Dimensional Fourier Imaging of Light Using Acoustic Pseudo Beam Steering," 1975 Ultrasonics Symposium Proceedings, pp. 136-140.
2. S.T. Kowel, P.G. Kornreich, A. Mahapatra, and B. Emmer, "Experimental Confirmation of Two-Dimensional Acoustic Processing of Images," 1976 Ultrasonics Symposium Proceedings, pp. 668-672.
3. S.T. Kowel, P.G. Kornreich, A. Mahapatra, M. Mehter, and P. Reck, "The Vector Imaging Convolver," 1977 Ultrasonics Symposium Proceedings, pp. 715-720.
4. S.T. Kowel, P.G. Kornreich, K.W. Loh, A. Mahapatra, M. Mehter, P. Reck, B. Emmer, and W. A. Penn, "Two-Dimensional Transform (DEFT) Devices: Analysis, Fabrication, and Evaluation," Report DAAG53-76-C-0162 (1977), prepared for U.S. Army Night Vision Laboratory, Ft. Belvoir, VA 22060.
5. S.T. Kowel, P.G. Kornreich, K.W. Loh, A. Mahapatra, M. Mehter, P. Reck, and B. Emmer, "Imaging Without Spatial Raster Scanning," submitted for publication in the IEEE Transactions on Electron Devices, to be published.
6. P.G. Kornreich, S.T. Kowel, A. Mahapatra, and M. Mehter, "Monolithic Two-Dimensional Fourier Transformer," 1978 International Optical Computing Conference Proceedings, London, 1978.
7. H. Gautier, C. Maerfeld, and P. Tournois, "Diode Acoustic Devices Applied to Optical Imaging," 1978 Ultrasonics Symposium Proceedings.

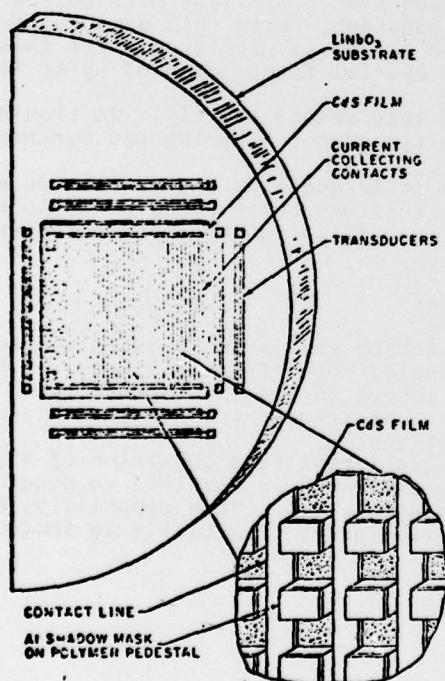


Fig. 1. Two-dimensional DEFT sensor, showing the monolithic sampling technique.

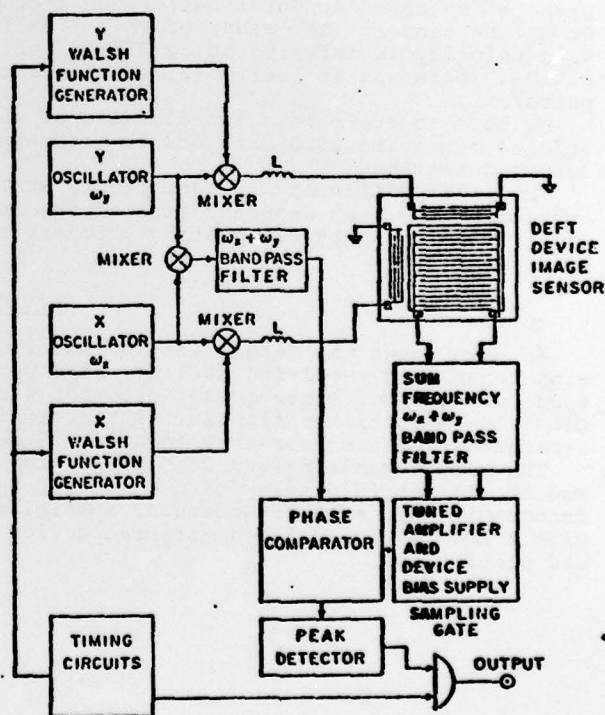


Fig. 2. Schematic of a Hadamard transformer based on the DEFT sensor.

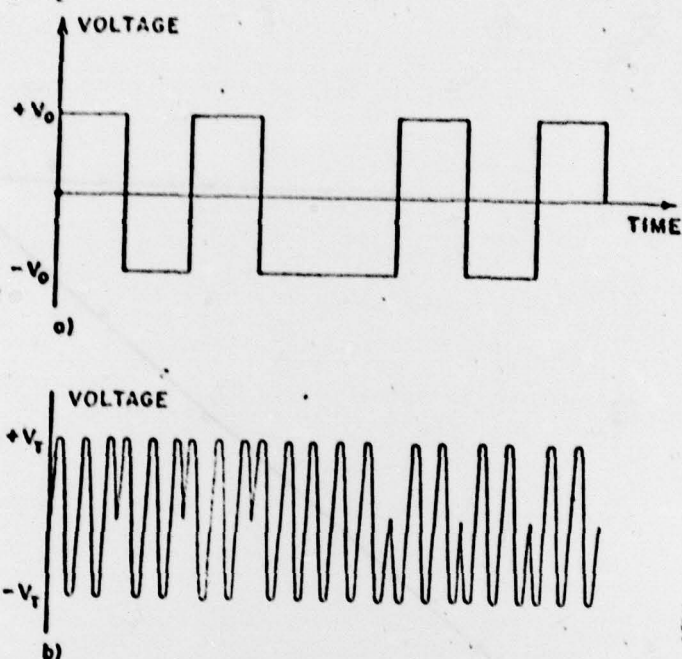


Fig. 3. Pulse modulation used for encoding a Walsh function onto the sinusoidal carrier appropriate for the transducer (a). The final mixed signal is shown in (b).

See Figs. (II.2) in text.

Fig. 4. Spectrum of a bar pattern with 7.2 lines/inch. Note the 'd.c.' peak at the center, and the two prominent peaks along the diagonal. The bar pattern was oriented with the bars at 45° , yielding a spatial frequency vector along the 135° and along the 315° directions as shown.

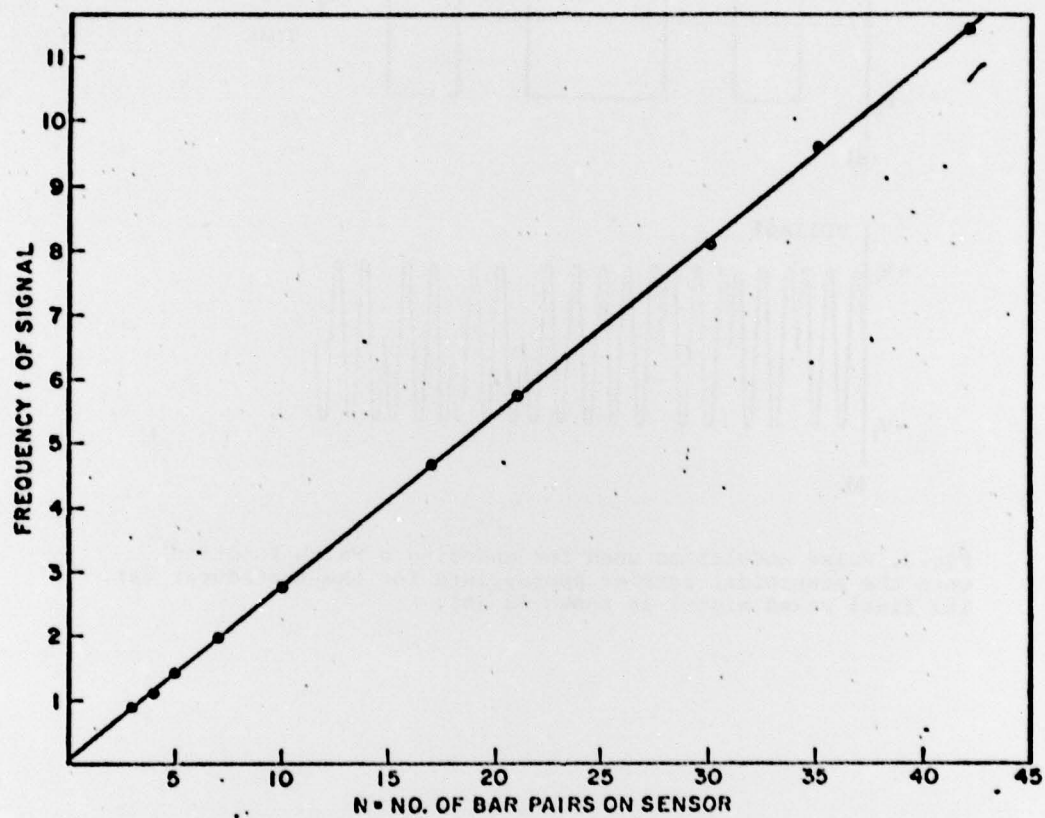


Fig.5. Results from the unidirectional 100 MHz sensor.
Note the linear map of detected difference frequency (MHz)
versus the primary spatial frequency in the image.

APPENDIX XI.
PATENT RIGHTS

Appendix XI

The following patents and applications were filed by Philipp G. Kornreich and Stephen T. Kowel on behalf of Syracuse University by the Research Corporation, New York, New York. The United States Government retains a royalty-free license to all patents. Deft Laboratories, Inc., East Syracuse, New York, has taken an exclusive non-governmental license.

<u>Patent Rights</u>	<u>Issue Date</u>	<u>Title</u>
United States Patent No. 3,836,712	9/17/1974	"Direct Electronic Fourier Transforms of Optical Images"
Canadian Patent No. 993,098	7/13/1976	"Direct Electronic Fourier Transforms of Optical Images"
Italian Patent No. 1,008,040	11/10/1976	"
United Kingdom 1445119	12/01/1976	"
United Kingdom 1445120	12/01/1976	"
United Kingdom 1480289	7/20/1977	"Measuring the Sharpness of Images"
United States No. 4,040,091	8/02/1977	"Direct Electronic Fourier Transforms of Optical Images"
United States No. 4,040,112	8/02/1977	"
United States 4,063,281	12/13/1977	"Motion Detection Employing Direct Fourier Transforms of Images"
United States 4,053,934	10/11/1977	"Measuring the Quality of Images"
United States 4,065,791	12/27/1977	"Interaction of Image with Strain Waves to Derive Fourier Transform Components of the Images"
<u>Applications</u>	<u>Filing Date</u>	<u>Title</u>
Austrian Patent Appl. #11 A 8213/74	10/00/1974	"Measuring the Sharpness of Images"
Canadian Patent Appl. #211,440	10/15/1974	"
French Patent Appl. #73,34,793	9/28/1973	"Direct Electronic Fourier Transforms of Optical Images"

<u>Applications</u>	<u>Filing Date</u>	<u>Title</u>
Dutch Patent Appl. #13,380	9/28/1973	"Direct Electronic Fourier Transforms of Optical Images"
Japanese Patent Appl. #108,065/73	9/27/1973	"
Japanese Patent Appl. #118,331/74	10/08/1974	"Measuring the Sharpness of Images"
U.S.S.R. Patent Appl. #1959357/18-24	9/28/1973	"Direct Electronic Fourier Transforms of Optical Images"
U.S.S.R. Patent Appl. #2044412/18-24	7/09/1974	"
W. German Patent Appl. #P 23 48 385.4	9/28/1973 (Allowed, 2/79)	"Direct Electronic Fourier Transforms of Optical Images"
W. German Patent Appl. #P 24 47 914.9	10/08/1974 (Allowed, 2/79)	"Measuring the Sharpness of Images"